# ACCELERATING CHEMICAL SIMILARITY SEARCH USING GPUS AND METRIC EMBEDDINGS

A DISSERTATION
SUBMITTED TO THE DEPARTMENT OF COMPUTER SCIENCE
AND THE COMMITTEE ON GRADUATE STUDIES
OF STANFORD UNIVERSITY
IN PARTIAL FULFILLMENT OF THE REQUIREMENTS
FOR THE DEGREE OF
DOCTOR OF PHILOSOPHY

Imran Saeedul Haque
September 2011

# Abstract

Fifteen years ago, the advent of modern high-throughput sequencing revolutionized computational genetics with a flood of data. Today, high-throughput biochemical assays promise to make biochemistry the next data-rich domain for machine learning. However, existing computational methods, built for small analyses of about 1,000 molecules, do not scale to emerging multi-million molecule datasets. For many algorithms, pairwise similarity comparisons between molecules are a critical bottleneck, presenting a 1,000×-1,000,000× scaling barrier.

In this dissertation, I describe the design of SIML and PAPER, our GPU implementations of 2D and 3D chemical similarities, as well as SCISSORS, our metric embedding algorithm. On a model problem of interest, combining these techniques allows up to 274,000x speedup in time and up to 2.8 million-fold reduction in space while retaining excellent accuracy. I further discuss how these high-speed techniques have allowed insight into chemical shape similarity and the behavior of machine learning kernel methods in the presence of noise.

# Acknowledgements

I offer a world of thanks to the people who have helped me through the process of graduate school and the Ph.D. First and foremost, I thank my family: my parents Yusuf and Nilufar, brothers Omar and Ejaz, and all the rest. Five years feels a lot longer in the middle of year three; knowing that my family is local, understands the doctorate process, and is behind me has been huge. (Grabbing the occasional home-cooked meal doesn't hurt either.) In particular, to my grandmother: you surely didn't know, in the middle of my second year, that I was doubting whether I had the chops to compete with all the sheer talent around me. But after you said, "I'm so proud, three generations: first your grandfather with a Ph.D., then your father, and now you." — there wasn't any other way to go, was there? Thank you.

Thanks also to my friends, be they from my days at Stanford, Berkeley, Bellarmine, Challenger, or even before. Staying in the Bay Area for so long has its advantages, and a deep social network is definitely among them. Go Bells and go Bears!

When we get to the actual "work" part of this thesis, many thanks to my primary thesis advisor, Vijay Pande. I could not have asked for a better advisor than Vijay; the care he shows for his graduate students, whether it is reflected in the questions he asks at weekly meetings, his encouragement of (seemingly distracting) side projects, the *laissez-faire* strategy for working hours, or even simply his support for lab members working with modern computer equipment, appear in both the happiness and productivity of the lab as a whole. Vijay, it's been a privilege to have worked with you. This applies equally to the rest of the Pande group. Listing everyone would extend this section to ten pages. Suffice it to say that you all have taught me that nothing in computational biochemistry works (but some things do); that thermodynamics is equally applicable to protein folding and the tailgate preparation of roast duck; that the wet lab is full of pain, but stepping away from the computer is a good idea;

and that even though it seems like our projects may be too many steps removed from the real world, that it's important to keep your eyes on the target.

Funding for my graduate work was provided in large part by a graduate research fellowship from the National Science Foundation, so thanks to the American taxpayer for considering science to be a worthy cause.

Oh, and finally: haters to the left. Thanks.

# Contents

# List of Tables

# List of Figures

# Chapter 1

# Introduction

Two major open problems in biochemistry are the ability to identify the proteins that will bind an arbitrary small molecule in the cellular milieu as well as the converse problem of finding compounds that would be bound by a particular protein. In various guises, these fundamental questions underlie a large portion of drug discovery, toxicology, and chemical biology in general. Target-based small molecule drug discovery (in which it is desired to find a small molecule that activates or inhibits a known "target" protein) essentially focuses around these two questions: finding an active compound is an instance of the latter problem. Trying to predict the side effects and toxicity of a known compound is, at least in part, a matter of discovering its possible "off-target" activities: other proteins to which the compound binds whose activity is modulated thereby in a biologically-significant manner.

The most reliable methods to discover these activities are experimental: *in vitro* assays, testing isolated compound and protein in solution; cellular assays testing compounds in cells; *in vivo* animal screens; and human clinical trials. Because of the importance of acquiring experimental protein binding data, significant improvements have been made in recent years in high-throughput experimental techniques. Massively parallel methods like high-throughput screening (usually using fluorescence or absorbance readouts in a 96-, 384-, or 1536-well plate format to quickly assay inhibitory potential) or highly-parallel isothermal titration calorimetry (to directly measure the binding enthalpy and entropy) are able to test hundreds to thousands of compounds simultaneously against a desired target protein. Conversely, protein microarrays and bound-ligand affinity chromatography can

rapidly find proteins that will bind a particular compound with high affinity. Unfortunately, experimental methods face problems of cost as well as sheer scale: assays require the use of compounds and proteins that are often expensive and/or hard to synthesize/express, and assay cost and time (on a per compound-protein pair basis) rises exponentially going from *in vitro* to cellular, animal, and human testing. Furthermore, with thousands of known proteins and over 35 million purchasable compounds, exhaustive experimental validation of all possible binding pairs is not possible. It is also unnecessary: typical high-throughput screens show that only a small fraction of compounds will actually inhibit a typical target at reasonable concentration.

## 1.1 Computational Biochemistry

The high expense and labor-intensive nature of experimental biochemistry motivates computational approaches to the problem. One promising avenue is the use of physical simulation to predict binding affinity. Free energy perturbation methods using molecular dynamics [19, 80] or Monte Carlo [23, 50] techniques to sample the thermodynamic protein-ligand binding partition function have shown success in estimating the binding affinity for a variety of protein-ligand systems. However, such methods are extremely computationally intensive, often taking days or weeks of supercomputer time to simulate even "easy" systems with little protein flexibility. Furthermore, it is not clear whether current molecular dynamics force fields and solvation models would even yield correct answers in the limit of infinite computer time (in particular, the treatment of polarizability in most current forcefields is weak) [52, 69]. The key reason for the expense of physical simulation is that it tries to make an affinity prediction from physics alone, without harnessing related experimental data (except indirectly through forcefield parameterization).

Consequently, it is of interest to consider computational methods to address the protein-ligand binding question that are cheaper than full physical simulation. The field of chemical informatics (also known as cheminformatics or chemoinformatics), studies ways to organize and search chemical information, such as structures and assay data. In particular, a subfield of cheminformatics, which I will term "biochemical machine learning," or BML, seeks to build models from existing experimental data to predict the results of future related assays

using statistical and machine learning methods. When cast in the language of data mining, the biochemical learning problem is the following: we are given a matrix with proteins along the rows and compounds along the columns in which each element is the binding affinity (or inhibitory concentration, etc.) between that pair. Training data in this matrix are only sparsely available (i.e., experimental values cover a very small subset of all possible protein-ligand pairs) and are expensive to obtain; we would like to use a learning method to predict the remaining entries.

A number of specific problems in biochemical machine learning, frequently treated in the literature, can be expressed as variants of this problem. For example, in ligand-based virtual screening, a number of compounds are known to be active against a particular target; a large database of compounds is then queried for compounds hypothesized to be active based on this training information. In the matrix formulation, this would be a query in which a few elements are known in a given row, and we would like to predict the remainder. Prediction of off-target activities is the transpose of this problem: here, we know one or a few proteins to which our compound binds, and would like to predict other unknown binding partners in the same column. Higher-order methods can be constructed by considering more than one row or column in isolation; for example, one might use the fact that some compounds show correlated activity on many proteins to predict that they should share activities on a new protein.

BML, broadly speaking, can be divided into "structure-based" and "ligand-based" techniques; in the former, structural information about both the protein target as well as the chemical compound in question are available, whereas the latter uses only information about the compounds. Structure-based techniques, such as docking, are often able to use physics-based predictor functions [26, 43]. However, they are unusable for problems lacking a solved protein structure or those for which the protein mediating a physical effect of interest is unknown. Ligand-based methods, in contrast, require no protein information, but cannot bring as much physical detail to bear. Rather, almost all ligand-based techniques fundamentally rely on a hypothesis of similarity: that compounds which are "similar" according to some measure will exhibit similar biological activity. Therefore, the definition and evaluation of chemical similarity is essential to the practice of biochemical machine learning [64].

## 1.2 Chemical Similarity

Broadly speaking, chemical similarity methods can be classified into three categories: property-based, two-dimensional (2D), and three-dimensional (3D). From a machine learning standpoint, each class of similarity method can be interpreted as using a different set of features defined on compounds. Property-based methods use as compound features various physical properties of the molecule: for example, molecular weight, polar surface area, log octanol-water partition coefficient (logP, a measurement of water solubility), or number of rotatable bonds. While historically important to the development of cheminformatics, purely property-based descriptors play a relatively minor role today except in particular specialties (for example, in predicting membrane permeability [72]). Such methods are also often used as negative controls in evaluating newer similarity techniques: it is expected that improved similarity techniques ought to be able to outperform simple molecular weight thresholds, for example.

2D similarity measures consider as features various properties of the chemical graph of a compound. The chemical graph is a graph with vertices defined by atoms and edges corresponding to interatomic bonds. Various properties can be associated with vertices: typically, atom name (carbon, nitrogen, etc.), atom type (defined by particular force fields, but may include atomic orbital hybridization information), and charge state. Edges also have properties: most importantly, bond order defines the number of electron pairs shared in that bond (1, 2, or 3), and additional properties such as bond aromaticity or resonance may also be stored.

Different 2D methods are distinguished by their way of processing the chemical graph to yield features. Fixed-substructure fingerprints, such as MDL keys [25], define for each molecule a feature vector as a fixed-length binary vector. Each bit in this vector corresponds to the presence or absence of a particular subgraph in the compound. The fixed set of subgraph queries makes these methods both inflexible and insensitive: new chemical matter containing subgraphs not present in the fingerprint set will not be well-mapped onto the feature space.

Hashed substructure fingerprints, such as the extended-connectivity fingerprint (ECFP) family [74], take a different approach. Rather than checking for the presence or absence

of predefined subgraphs, these methods enumerate all subgraphs present in the molecule, under certain constraints. For example, ECFP$x$, for a positive integer $x$, considers around each atom the $x$-bond-radius subgraph around that atom. Each subgraph is then hashed into a very large binary vector, which is then reduced to a smaller (order of 1-4 kbit) vector by "folding" (recursive binary-OR reduction). Hashed fingerprints gain flexibility at the cost of interpretability, as individual fingerprint bits can no longer be unambiguously associated with particular chemical features. Nevertheless, the use of 2D fingerprints for chemical machine learning is widespread. Evaluation of 2D similarity is very fast (especially once fingerprints have been precomputed). 2D graph analysis also aligns well with intuition over chemical structures and reactions, which are often understood as graph transformations (e.g., subgraph augmentation or deletion in adding/removing functional groups).

While broadly used, 2D methods abstract away the physical reality of molecules by considering only their atomic connectivity graphs. Molecules exist as three-dimensional arrangements of atoms in space and this geometry is important to their activity. Recognizing this, various methods exist to measure this similarity. Atom-distance methods are purely geometric, considering the distribution of distances among atom pairs (or higher-order tuples) or various descriptors of the overall molecular shape, such as maximum internal lengths [5, 48, 76]. Field-based methods define the molecule as a scalar density field in 3-dimensional space (with density defined by van der Waals volume, electrostatic potential, or proximity to a particular desired chemical feature) and compute similarity between molecules as a functions between a pair of fields [18, 21, 33]. Finally, surface similarity techniques consider only the similarity of compounds (e.g., in terms of sterics, hydrogen bonding, and electrostatics) at their molecular surfaces [46]. 3D methods are an attempt to model more faithfully the physical factors behind protein-ligand binding (such as steric exclusion and electrostatic complementarity). However, as a consequence, they are often much slower to evaluate than 2D similarities, with individual similarity evaluations taking on the order of milliseconds to seconds, rather than nanoseconds to microseconds for 2D similarities on precomputed fingerprints.

## 1.3 Modern Cheminformatics

An emerging trend in chemical informatics is the public availability of very large databases of chemical structures and biochemical assay data. While pharmaceutical companies have long had extensive databases of internal assay data and compound libraries, recent efforts have begun to release large amounts of data to the public domain. The PubChem project from the US National Center for Biotechnology Information (NCBI) holds, at the time of writing, data from more than 34,000 assays, testing over 960,000 compounds. On a similar scale, ChEMBLdb from the European Bioinformatics Institute has data on more than 8,000 protein targets and 600,000 compounds. While much of the data comes from publicly-funded ventures (such as the US National Institutes of Health Molecular Libraries Screening Centers Network) and academic labs, private companies have also begun to release significant amounts of data to the public. Perhaps the most prominent example to date has been the release by GlaxoSmithKline of structures and assay data on thousands of compounds hoped to be useful in the development of novel antimalarials [29].

The size of unlabeled chemical databases (i.e., those without assay information) has also dramatically risen. NCBI's PubChem3D database contains descriptors and computed 3-D structures for, at the time of writing, over 17 million compounds. The ZINC database [45] contains structures with protonation states computed for various pH conditions for approximately 35 million compounds claimed to be purchasable by their vendors. Continuing increases in computer power have inspired databases with even larger ambitions. The GDB-13 [8] database, containing around $10^9$ compounds, claims to enumerate all "reasonable" chemical structures of 13 heavy (non-hydrogen) atoms or fewer containing a restricted subset of atoms often found in organic chemistry; even larger so-called "generated" or exhaustive databases have been proposed. Also in use are combinatorial databases, which are able to contain $10^{12}$ or more compounds implicitly by specifying a chemical scaffold and sets of possible transformations which create a combinatorially-large space of possibilities. Ultimately, it is believed that the size of the synthesizable chemical universe under 30 heavy atoms may be in the vicinity of $10^{60}$ compounds [9].

Unfortunately, computational methods in biochemistry have not kept pace with the accelerating pace of experimental data acquisition. Many analysis methods were originally

developed to handle datasets on the 1,000 to 10,000 molecule scale — a very reasonable size for dealing with single assays. Recent work has examined the similarity network structure of a 400,000 compound subset of ZINC [84]. However, to achieve this, the authors had to use computationally-inexpensive 2D similarity measures, use random subsampling, and limit the scope of their analysis (in particular, no attempt was made at machine learning for ligand activity). Even this work, at the limit of the computational capability in the field, considers a number of compounds less than half the number of compounds with at least one assay annotation in PubChem; it is orders of magnitude smaller than unlabeled databases like PubChem3D or ZINC. There is a 10-100$\times$ gap in the size of computational analyses that have been performed, and the size of databases that are already available (and growing).

The true gap in computational capability is much worse than the 10-100 fold number would indicate; many methods of interest scale supralinearly in both time and space. For example, methods that build graphical models based on the pairwise similarity network on a set of compounds scale approximately as O($N^2$) in time and space, due to the requirement to compute, histogram, and threshold the similarity matrix on compounds to set statistically-relevant cutoffs on edges. A 10-100 fold gap in $N$ implies that our computational capabilities are $10^2$-$10^4$ fold too weak to handle such quadratic-scaling problems.Table 1.1 shows the approximate runtime and storage requirements of such a hypothetical method, based on the ability to evaluate 100,000 pairwise compound similarities per second. Of particular note is that storage becomes a serious concern for such methods. At the ten million molecule scale, runtime is 3 CPU-yr, which is easily achieved on a cluster of modest size; however, the required petabyte of storage is prohibitive with 2011-era technology. The GDB13-scale billion-molecule database is impossible from both runtime and storage standpoints.

| **Problem size** | **CPU time** | **Storage needed** |
|---|---|---|
| 10 mols | 1 ms | 1 kB |
| 10K mols | 1 min | 1 GB |
| 100K mols | 1 day | 1 TB |
| 10M mols | 3 yr | 1 PB |
| 1B mols | 30K yr | 10K PB |

Table 1.1: Runtime and storage requirements for a hypothetical BML method requiring O($N^2$) time and space

For many biochemical machine learning methods, the evaluation of pairwise ligand similarities is a critical bottleneck. The example method of table 1.1 considered only the runtime of similarity computations, ignoring the cost of model training, and already was prohibitive on modern datasets. Furthermore, many similarity measures of interest, particularly 3D similarities, are much slower than hypothesized in the table. ROCS, a widely-used 3D similarity method developed by OpenEye Scientific Software, can compute $\sim$100-1000 similarities per second — thousands of times slower than assumed in the table. For this reason, improving the performance of chemical similarity computation is of critical importance to scaling machine learning to handle modern-scale biochemical data sets.

In this dissertation, I demonstrate that a two-pronged approach combining special-purpose hardware with approximation algorithms is able to solve this scaling challenge for an interesting subset of similarity measures. In the first half of the approach, I exploit the massive parallelism of modern programmable graphics processors (GPUs) to accelerate direct evaluation of both 3D and 2D similarity measures (chapters 2, 3, and 4), achieving 30-100$\times$ speedup. The second half of the strategy involves the development of a metric embedding algorithm named SCISSORS, described in chapter 5. SCISSORS is used to embed molecules into a real vector space such that similarity evaluations in this vector space are a good approximation for the original similarity scores. Importantly, in chapter 8 it is demonstrated that this embedding can be performed in effectively linear time even for a very large library like PubChem3D. Similarity computations in the embedded space are so fast that the time for full pairwise comparison is dominated by the embedding cost, yielding a final speedup from embedding alone on the order of 1000$\times$. In chapter 8, I demonstrate that GPU acceleration forms an excellent complement to the embedding method: the GPU-accelerated approximate similarity presented there is over 250,000$\times$ faster at a PubChem3D-scale O($N^2$) problem than the original technique. The combination is so fast that it effectively solves the storage problem as well as the computation problem; for both 2D and 3D similarities, the techniques described in this thesis can recompute the O($N^2$) similarity matrix from O($N$) stored data faster than the similarity matrix could be read back by a reasonable disk array, obviating the need to store a quadratic amount of data.

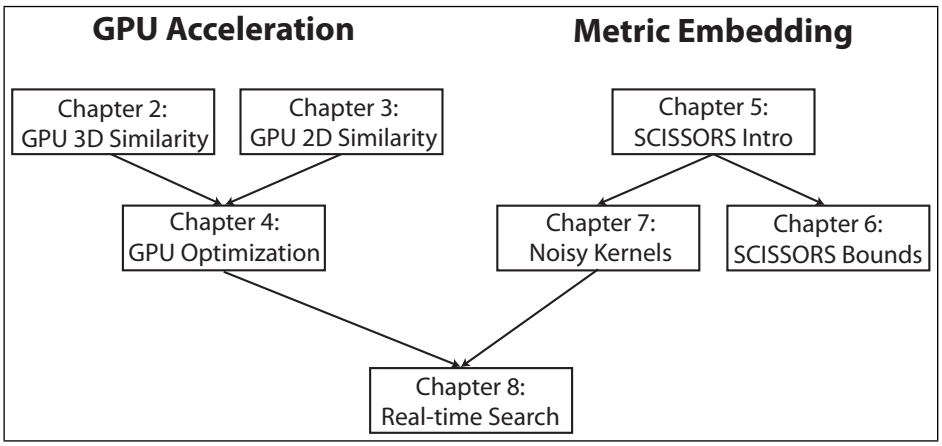


Figure 1.1: Chapter dependency graph

## 1.4 Outline and Reading Order

This thesis consists of two major divisions. The first half (chapters 2, 3, and 4) is systems-oriented, and concerns the design, implementation, and optimization of GPU-accelerated 3D and 2D similarity measures. The second half (chapters 5, 6, and 7), is more theoretical, detailing the SCISSORS metric embedding algorithm, proving bounds on its performance, and discussing interesting implications of imprecise or approximate evaluation on the use of kernel methods in machine learning. Finally, chapter 8 combines the two tracks of the thesis to demonstrate that GPU acceleration plus metric embedding can be used to enable interactive search of large chemical databases.

The chapters of this thesis are structured such that they may be read independently. However, certain chapters follow logically from others and build on their results. Figure 1.1 depicts the suggested reading order on the chapters.

# Chapter 2

# GPU Acceleration of 3D Chemical Shape Similarity

## Abstract

Modern graphics processing units (GPUs) are flexibly programmable and have peak computational throughput significantly faster than conventional CPUs. Herein, we describe the design and implementation of PAPER, an open-source implementation of Gaussian molecular shape overlay for NVIDIA GPUs. We demonstrate one to two order-of-magnitude speedups on high-end commodity GPU hardware relative to a reference CPU implementation of the shape overlay algorithm and speedups of over one order of magnitude relative to the commercial OpenEye ROCS package. In addition, we describe errors incurred by approximations used in common implementations of the algorithm.

This chapter (excluding appendices) has appeared previously in reference [39].

## 2.1 Introduction

Molecular shape comparison is a technique that identifies common spatial features among two or more molecules and can be used as a similarity measure for ligand-based compound discovery efforts. A popular technique of shape comparison, implemented in the ROCS [73] package from OpenEye Scientific Software, applies the technique of Gaussian volume overlap optimization [33] to perform a robust and fast shape overlay. ROCS is used extensively in compound discovery and screening library development efforts [4, 37, 75, 82]. However, even with the efficiency of the Gaussian optimization technique, ROCS can take a very long time to run when scanning over large compound sets, as in virtual high-throughput screening. OpenEye's support for PVM (Parallel Virtual Machine) clusters in its ROCS software demonstrates that such screening with conventional ROCS is too slow to be carried out on single computers. Therefore, new methods to accelerate ROCS-style alignment should be useful for large-scale screening studies.

Recent trends in computer architecture have shifted the balance and nature of computational power on commodity desktops. The GeForce 8 series and Radeon X1000 series of graphics cards from NVIDIA and AMD changed the conventional model of graphics processing units (GPUs) — whereas GPUs began as task-specific engines for 3D rendering, modern graphics cards are general, extremely-parallel computational engines. The CUDA and CAL initiatives from NVIDIA and AMD, respectively, have made GPUs programmable without the use of graphics-specific programming languages. On many measures including peak FLOPS (floating-point operations per second), FLOPS per watt, and memory bandwidth, modern GPUs outperform top-of-the-line CPUs on workloads that map well to their parallelism, making GPU ports of conventional codes attractive from a performance perspective.

In this article we describe PAPER ("PAPER Accelerates Parallel Evaluations of ROCS"), an open-source implementation of ROCS's Gaussian volume overlap optimization on NVIDIA GPUs, available for download at `https://simtk.org/home/paper/`. We begin with an overview of Gaussian overlap optimization (**Section 2.2.2**). We continue with a description of the NVIDIA G80 architecture and the design decisions involved in implementing ROCS-style optimization on such hardware in **Section 2.3**. Finally, we examine

the performance of our implementation. We highlight errors caused by algorithmic approximations made by ROCS (**Section 2.4.2**). Furthermore, we demonstrate virtual screening performance comparable to that of OpenEye ROCS (**Section 2.4.3**). Finally, we show one to two order-of-magnitude speedups relative to a CPU implementation of our program (**Section 2.4.4**), and speedups of over one order-of-magnitude relative to OpenEye ROCS (**Section 2.4.5**).

## 2.2 ROCS: Rapid Overlay of Chemical Structures

### 2.2.1 Theory of Molecular Shape

The volume overlap between a pair of molecules A and B can be expressed as a product integral between density functions representing the two molecules, where the integral is taken over all space:

$$\int d\mathbf{r}\rho_A\rho_B \tag{2.1}$$

These molecular density functions can be constructed from the density functions for the component atoms 1...N by the relation

$$\rho_A(\mathbf{r}) = 1 - \prod_{i=1}^{N}(1 - \rho_{Ai}(\mathbf{r})) \tag{2.2}$$

or, by the principle of inclusion-exclusion, as the following series of summations, which account for overlaps between atoms:

$$\begin{aligned}\rho_A(\mathbf{r}) &= \sum_i \rho_{Ai} - \sum_{i<j} \rho_{Ai}\rho_{Aj} + \sum_{i<j<k} \rho_{Ai}\rho_{Aj}\rho_{Ak} \\ &- \sum_{i<j<k<l} \rho_{Ai}\rho_{Aj}\rho_{Ak}\rho_{Al} + \cdots\end{aligned} \tag{2.3}$$

The simplest definition of these atomic density functions $\rho_{Ai}$ sets them to 1 inside the van der Waals radius of atom i, and 0 outside. Such a "hard-sphere" model is conceptually

simple, but has the disadvantage of being nondifferentiable, and therefore not amenable to numeric optimization techniques. Although analytic hard-sphere models have been developed [21], their complexity hinders performance. For this reason, Grant and Pickup [35] proposed representing each atom as a spherical Gaussian function:

$$\rho_{Ak}(\mathbf{r}) = p_k \exp\left(-\alpha_k ||\mathbf{r}_k - \mathbf{r}||^2\right) \tag{2.4}$$

Such Gaussian functions are smooth and differentiable. Furthermore, simple closed-form expressions for the volumes, volume gradients (with respect to position), and Hessians of the product of an arbitrary number of such Gaussians are known [35].

### 2.2.2 Optimization of Volume Overlap

Our optimization procedure largely follows the prescriptions from the original paper describing Gaussian volume overlap optimization [33], including the parameters defining the atomic Gaussians: we set $p_i = 2\sqrt{2}$ and

$$\alpha_i = \left(\pi\left(\frac{3\sqrt{2}}{2\pi}\right)^{\frac{2}{3}}\right) r_i^{-2}$$

where $r_i$ is the van der Waals radius of atom $i$.

We parameterize the rigid-body transformation as a vector in $\Re^7$, composed of a 3-dimensional translation and a 4-dimensional quaternion. The quaternion component parameterizes the rotation as in the work of Griewank et al. [36]. It is restrained to unity magnitude by a penalty term described by Kearsley[51], which resembles a Lagrange-multiplier technique, but with a fixed multiplier. We calculate both the overlap function and its gradient with respect to the transformation coordinate, and optimize the molecular overlap using a BFGS method [70] reimplemented for parallel execution on the GPU.

Because BFGS is a local optimizer, the starting configurations affect whether or not a global optimum is reached. We initialize starting states similarly, but not identically, to the Grant et al. method [33]. Unlike ROCS, we do not calculate shape centroids and multipoles to determine starting positions and orientations. We determine the starting origin by an

arithmetic mean of all atom centers. The base orientation for each molecule is calculated by rotating the molecule into the axes determined by the singular value decomposition of the point cloud comprised by the atom centers. This SVD is equivalent (for non-degenerate cases) to calculating the principal component axes of the atom centers.

Although the ROCS documentation claims that 4 starting coordinates are sufficient to reach global optima [73], we have found (and discuss below) several cases in which this is not true. This is a known problem — Grant et al. found cases requiring the use of Monte Carlo optimization [33], and a more recent shape similarity paper [62] explains that ROCS uses extra starting positions especially for molecules of high symmetry. We therefore support multiple methods for generating initial configurations, including both deterministic and randomized sampling of starting configurations, with varying sampling resolution.

## 2.3 Implementing Shape Overlay on the NVIDIA G80

### 2.3.1 NVIDIA G80 GPU Architecture

The NVIDIA G80 architecture, underlying all GeForce 8 and 9 series graphics cards, and a derivative of which (GT200) underlies the GTX 200 series, is based on a "scalable processor array" which can simultaneously execute up to 128 threads [55]. At a high level, the GPU is structured as a number of TPCs (texture/processor clusters), each containing 2 (in G80) or 3 (in GT200 [86]) SMs (streaming multiprocessors). Each SM consists of 8 single-precision floating point cores and 2 special-function units (SFUs) to handle transcendental operations. Each SM also contains its own 16KiB of fast "shared memory", which can be treated as a user-controlled cache for the much larger "global memory" on the graphics card, and several thousand (8192 on G80, 16384 on GT200) registers.

### 2.3.2 The CUDA Programming Language

CUDA [63] is a C-like programming language developed by NVIDIA to run general-purpose computation on their G80 and newer graphics hardware. Following closely the structure of the NVIDIA hardware, the CUDA execution model allows the execution on the GPU of massively-multithreaded "kernels", or GPU programs. The threads of each kernel are

arranged into thread blocks such that each block executes on exactly one SM (streaming multiprocessor) on the hardware. Furthermore, each thread block has exclusive use of a programmer-specified amount (up to the 16 KiB limit) of shared memory on its SM. Multiple thread blocks may be assigned to the same SM if shared memory and register allocation permit, in which case the SM time-slices between the blocks to hide latency from memory access and instruction dependence.

CUDA's memory model also reflects the structure of the underlying hardware, and this structure is crucial for extracting maximum performance from the language. The fastest storage is the register file in each SM, which is allocated on a per-thread basis (so that the total number of registers used by a kernel equals the number of registers required per thread times the number of threads per block). Next is the shared memory, which is local to each thread block, and can be used for inter-thread communications. Shared memory is divided into banks, such that under certain addressing restrictions, all threads can simultaneously read from or write to shared memory. The largest and slowest memory is the main memory on the graphics card, which CUDA splits into four categories:

- "Global memory" is general storage which is accessible to all threads and blocks of the GPU program, but with a significant latency (hundreds of clock cycles), and which can only reach its maximum bandwidth if accessed coherently (addressed sequentially within blocks).

- "Local memory" is thread-local storage used to handle situations in which there are insufficient registers on the SM to execute the kernel. Like global memory, it has high latency.

- "Texture memory" describes read-only portions of global memory bound to special pointers; special hardware exists on-chip to cache reads from texture memory, and to do simple linear (or bi- or trilinear, for 2D and 3D textures) interpolation on texture values. This hardware allows efficient implementation of lookup tables in texture memory.

- "Constant memory" is a cached read-only portion of the device memory. Reads from this constant cache are as fast as register reads, if all threads in a *warp* (the scheduling

unit on the hardware) read from the same address; otherwise the latency increases linearly with the number of addresses read.

The primary way of loading data into a kernel from the host (CPU) side, or to bring results back from a kernel execution, is to copy it between system memory and preallocated space in the device global memory. However, because such a copy operation has relatively low bandwidth (around 1GiB/s) and significant latency (tens of microseconds), minimizing the number of GPU-CPU or CPU-GPU transfers is critical for maximizing performance.

### 2.3.3 Mapping ROCS Computation to NVIDIA Hardware

The CUDA programming model maps best to workloads that can be processed by many (hundreds to thousands) of independent blocks of threads, with a large amount of computation taking place on the GPU before more data is required from the CPU. Our implementation moves almost all of the ROCS algorithm onto the GPU to best meet these objectives.

We have designed PAPER for the case in which many molecules are compared against a single query molecule. This case can be expected to be common in virtual screening, in which a library may be scanned for similarity to one or a few actives. The SVD-based preprocessing of the molecules (Section 2.2.2) is handled externally in a Python script, as the results of the preprocessing are easily stored on disk and need not be repeated for every optimization.

In PAPER, the CPU first loads the molecules and then transforms them to an internal data format. Since the algorithm we implement uses a local optimizer, the use of multiple starting positions is important to find the global maximum in overlap. However, each of these molecule-position pairs is a completely independent optimization problem. Therefore, we make multiple copies of each molecule other than the query (the "fit" molecules) and transform each into its unique starting orientation. This input data (the query molecule, the copies of the fit molecules, and the starting coordinates corresponding to each transformed copy) are copied in bulk to the GPU, making it possible to do hundreds of ROCS-type optimizations in batch between CPU-GPU transfers, thereby minimizing transfer overhead.

PAPER maps the optimization onto the GPU in a manner designed to maximize the parallelism accessible. Although the GPU offers thousands of threads worth of parallel

processing, no single ROCS calculation has that much parallelism. Therefore, we run multiple calculations simultaneously — each molecule-orientation pair, as an independent problem, is mapped to a separate CUDA thread block.

Hardware resources used by the GPU are allocated in units of "warps": a warp corresponds to a number of threads that run simultaneously on an SM (32 on current NVIDIA hardware). If a given thread block has a number of threads which is not a multiple of the warp size, hardware resources are wasted. Since each thread block should contain at least one warp's worth of threads to fully utilize the hardware, but the use of more threads increases register pressure (thereby decreasing the number of blocks that can share an SM), we use 64 threads per block. This means that each molecule-orientation pair has its own 64 threads on the GPU.

Once the optimizations are completed in parallel on the GPU, PAPER reads the final overlap values and transformation coordinates back to system memory, and scans over each molecule-orientation pairing to find the orientation for each molecule that produced the maximum overlap. This is a relatively fast operation that can be efficiently performed on the CPU.

### 2.3.4 Memory Layout

In order to minimize the impact of global memory latency on the PAPER kernel, we arrange all data in global memory such that reads and writes can be performed coherently. In the current implementation, all molecular coordinates are copied into shared memory at the start of the kernel, so global memory access is not a limiting factor; however, this limits the size of the molecules that can be compared. PAPER can be easily modified to load molecules from global memory, in which case this coherent access layout will be important for achieving maximum performance.

Device memory arrays for the query molecule and the entire set of fit molecules are allocated using the CUDA call `cudaMallocPitch`, which guarantees address alignment for each row in a 2-D array. An N-atom molecule is represented as a 4xN array, where the first three rows correspond to the $(x, y, z)$ coordinates for each atom, and the last stores the precalculated $\alpha_i$ value for each atom. The starting transforms are similarly allocated as a

2-dimensional aligned array. Because all global memory loads and stores occur with aligned base addresses for each thread block, the hardware can coalesce the accesses made by each thread, maximizing memory bandwidth.

Finally, because of the high latency of global memory access, effective use of shared memory as a cache is crucial. PAPER is designed to solve ROCS problems on small molecules (as opposed to polymers or macromolecules), which have a relatively small number of atoms and whose coordinates therefore can fit entirely within shared memory. Because of this, at the beginning of the kernel execution, each thread block copies the data for the query molecule and its fit molecule into its shared memory. Once the molecules have been loaded at the start of the optimization, the PAPER kernel never needs to access global memory and is therefore unimpeded by the latency of global memory access. As currently implemented, PAPER can handle ROCS problems in which the number of atoms in the query molecule plus three times the number of atoms in the largest fit molecule in a batch is less than or equal to 889 (larger systems require more shared memory than the 16KiB available in current NVIDIA GPUs).

## 2.4 Results

We evaluate the performance of PAPER against two reference codes. The first, here called cpuROCS, is our C++ implementation of the algorithms used in PAPER, targeted to a single-threaded, CPU-execution model. It therefore serves as a benchmark for performance gained by porting to the GPU. The second, which we will denote as oeROCS, is the OpenEye implementation of their ROCS algorithms (as exposed through the Python oeshape toolkit). oeROCS represents a "real" code, which has presumably been optimized for performance, and which contains proprietary algorithmic modifications.

### 2.4.1 Testing Methodology

Accuracy and performance tests were performed on several different machines, the configurations of which are listed in Table 2.1. All molecules used in accuracy and performance testing were drawn from the Maybridge Screening Collection (N=56842), a chemical library

commonly used for screening experiments. Virtual screening tests drew molecules from the Database of Useful Decoys (DUD), release 2 [44] (excluding 2 GART decoys and 1 PDE5 decoy which failed preprocessing). Each molecule was preprocessed with OpenEye's OMEGA conformer generator [67] to generate a single 3D conformer.

| GPU | GPU RAM | CPU | CPU Architecture |
|---|---|---|---|
| NVIDIA GeForce 8600GT (32 SPs @ 1.2GHz) | 256 MiB @ 700 MHz | Intel Celeron 420 (1.6GHz) | Intel *Conroe* |
| NVIDIA GeForce 8800GTX (128 SPs @ 1.35GHz) | 768 MiB @ 900 MHz | Intel Pentium D (2.8GHz) | Intel *Prescott* |
| NVIDIA GeForce GTX 280 (240 SPs @ 1.296GHz) | 1024 MiB @ 1107 MHz | AMD Athlon 64 X2 4800+ (2.5GHz) | AMD *Hammer* |
| N/A | N/A | Intel Xeon E5345 (2.33GHz) | Intel *Conroe* |
| N/A | N/A | AMD Athlon 64 3800+ (2.4GHz) | AMD *Hammer* |

Table 2.1: Hardware configurations tested for performance and accuracy benchmarking. Systems without listed GPUs were used only for CPU-based (cpuROCS or oeROCS) benchmarking.

OpenEye OMEGA, ROCS, and OEOverlap used Bondi van der Waals atomic radii [12]; PAPER used Batsanov van der Waals radii [6], as implemented in OpenBabel's OBElementTable. OpenEye ROCS was run with the color force field disabled, so that optimization was performed purely on shape. ROCS was run in "Exact" mode (OEOverlapMethod_Exact), as its "Analytic" and "Analytic2" modes use approximations to Equation 2.4 which are not implemented in PAPER; Exact is therefore the closest match to the PAPER computation. All testing was done with exact atomic radii (i.e., without coercing all atoms to carbon's radius) and ignoring hydrogens. PAPER includes options to use carbon radii and hydrogens, if so desired.

### Accuracy Testing Methodology

For accuracy testing, we selected 1000 molecules at random from the Maybridge set to act as query molecules. For each query, we subsequently selected 1000 more molecules at random from the non-query set to act as the fit molecules, for a total of 1 million comparisons. For each query-fit pair, OpenEye ROCS and PAPER were used to generate transformation

matrices representing their best guesses at the optimal overlay. Each of these transformations was then evaluated by applying the transformation to the fit molecule and calculating the overlap volume and Tanimoto. To calculate the overlap volume, we used a custom code to numerically integrate Equation 2.2 by quadrature over a grid of resolution 0.5Å. This method accounts for multiple (higher than second-order) overlaps, which are not considered by OpenEye's OEOverlap code. From these overlap values we calculated Tanimoto scores using the relationship

$$Tanimoto_{A,B} = \frac{O_{AB}}{(O_{AA} + O_{BB} - O_{AB})} \tag{2.5}$$

where $O_{xy}$ is the (numerically evaluated) overlap volume between molecules x and y.

### Virtual Screening Methodology

To test virtual screening performance, we used the DUD database, release 2 [44]. DUD is a collection of "systems" consisting of proteins and associated small molecules. For each system, a certain number (varying by system, and here designated $N_\ell$) of molecules which are known to bind to the system's protein are designated as 'ligands'. The rest of the molecules associated with the protein ($N_d$, 36 for each designated ligand molecule) are 'decoys', which have similar physical properties to the ligands (such as molecular weight), but dissimilar chemical topology and therefore are believed to be inactive. For each protein system in DUD, we used oeROCS and PAPER to calculate the optimal overlay transformation of each ligand and decoy onto each ligand molecule. Each transformation was evaluated as for accuracy testing to generate an overlap Tanimoto value. For each ligand, all the molecules compared were ranked in order of decreasing Tanimoto, and the ROC AUC calculated according to the method in Clark [20]. For the AUC calculation, a true positive is a ligand molecule; a false positive is any decoy which is ranked higher than a true ligand. The reported AUC for each system is the mean of the AUCs for each ligand in the system. We used a bootstrapping procedure to estimate confidence intervals on the calculated AUC values. Each round of the bootstrap on a system with $N_\ell$ ligands and $N_d$ decoys involved the following steps:

1. Select a ligand from the system

2. Select $N_\ell - 1 + N_d$ molecules from the system with replacement, excluding the ligand selected in step 1

3. Sort the selected molecules by Tanimoto and calculate an AUC

After every 200 bootstrap rounds, we calculated estimates for the upper and lower bounds on the 68% and 95% confidence intervals of the AUC. Bootstrapping continued for a minimum of 10,000 rounds per system, or more if necessary to converge the estimates of each CI bound. Convergence was defined as the standard deviation of the most recent 25 estimates of the CI bound having magnitude less than 0.5% of the magnitude of the mean of the same estimates. The reported CI bounds are the means of the 25 final estimates.

### Performance Testing Methodology

For performance testing, we first chose three pairs of molecules (Figure 2.1). The 'medium' set (molecules 12290 and 37092) were chosen to have 22 heavy atoms, corresponding to the average heavy atom count in the Maybridge set. The 'small' set (12565 and 24768) were chosen to have 10 heavy atoms, and the large set (6647 and 51509) have 44 heavy atoms each. Each pair was chosen randomly from the set of all molecules with the appropriate number of heavy atoms. For each testing set, we arbitrarily designated the lower-numbered molecule as the query and the higher-numbered molecule as the fit molecule. PAPER and oeROCS were run over the small, medium, and large sets, each time comparing the query molecule to 1, 2, 5, 10, 20, 50, 100, 200, and 500 copies of the fit molecule per batch. cpuROCS was run similarly, but only up to 20 copies (since it was found that batching, as expected, did not impact its performance).

We built and tested cpuROCS using both the GNU C Compiler (gcc) and the Intel C Compiler (icc) on Intel-based systems. gcc is widely available and free for use; icc is not free for commercial or academic usage, but often displays significant speedup relative to gcc on Intel CPUs. On AMD-based machines only gcc was tested, as it is AMD's recommended compiler for the platform, and because of prior issues with icc on AMD CPUs. The following compiler optimization flags were used:

- gcc, Intel: `-O3 -march=nocona -msse -mfpmath=sse`

- gcc, AMD: `-O3 -march=k8 -msse -mfpmath=sse`
- icc, Intel: `-xT -axT -fast -march=core2`

To properly account for the overhead involved in host-device memory transfers, a standard testing iteration for PAPER included the following steps:

1. Copy query molecule, fit molecules, and starting transforms from host to GPU
2. Run PAPER kernel to optimize transformations
3. Copy final transforms and overlap values from GPU to host
4. Synchronize to ensure that kernel execution and memory copy have completed

Ten iterations were run for each initialization mode, molecule size, batch size, and compiler (cpuROCS only) for PAPER and cpuROCS and for each molecule size and batch size for oeROCS. The average optimization time per molecule was calculated by measuring the elapsed time over all ten iterations and dividing by ten times the number of molecules per batch. All speedups reported are in terms of the time-per-molecule.

### 2.4.2 Accuracy vs oeROCS

#### Accuracy versus initialization strategy

Because ROCS's method for initializing starting states has not been publicly disclosed, we tested a variety of initialization strategies (Table 2.2), including the one proposed by Grant et al. in the original Gaussian volume overlap optimization paper (here named mode 1). "Inertial overlay" refers to the SVD-based rotation and centroid overlay described in Section 2.2.2.

Figure 2.2 illustrates PAPER's overlay performance against that of OpenEye ROCS, as measured by the shape Tanimoto of discovered overlays. The results indicate that in most cases, oeROCS does better at finding the global maximum overlap orientation, regardless of initialization mode. This appears to be inherent to the Grant et al. algorithm, and not a GPU issue, as the cpuROCS reference code exhibits the same behavior. This is expected;

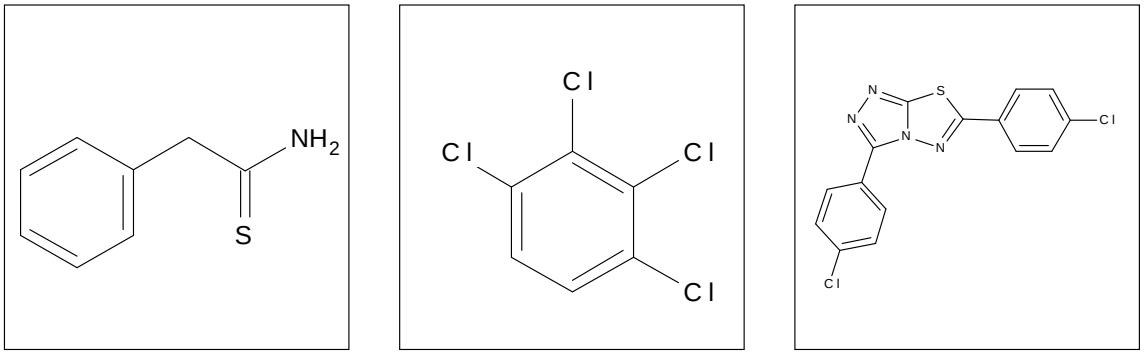


(a) ID 12565 (10 heavy atoms) (b) ID #24768(10 heavy atoms) (c) ID #12290(22 heavy atoms)

(d) ID #37092(22 heavy atoms) (e) ID #6647(44 heavy atoms) (f) ID #51509(44 heavy atoms)

Figure 2.1: Molecules used in PAPER performance testing

| Mode | # of Positions | Description |
|---|---|---|
| 0 | 1 | Inertial overlay |
| 1 | 4 | Mode 0 + $180^\circ$ degree rotations around each axis |
| 2 | 12 | Mode 0 + $90^\circ$ degree rotations around each axis |
| 5 | 31 | Mode 0 + 30 random starting orientations |

Table 2.2: PAPER Initialization Modes Tested
($M$,$N$ = # of cycle domains in query and fit)

OpenEye have disclosed the existence (but not nature) of improvements to their overlay algorithm beyond the Grant et al. prescription [62].

However, the results also clearly demonstrate the importance of using multiple starting positions with the local optimizer. Initialization mode 0 (Figure 2.2(a)), which uses only a single starting position, is clearly the worst performer — adding just three more rotational starting positions, as done by mode 1 (Figure 2.2(b)) improves performance. Although adding even more rotational starting positions, as done by mode 2 (Figure 2.2(c)) helps, the improvement is not as dramatic. Both modes 1 and 2 fail to sample translational space. Mode 5 uses a random initialization strategy to sample both rotations and translations (figure 2.2(d)) and seems to perform similarly overall to deterministic sampling.

Notably, increasing the sampling of starting configurations seems primarily to improve already poor overlaps, rather than significantly improving molecules that ought to overlap well. For example, of the 933,776 alignments with oeROCS Tanimoto $> 0.4$, oeROCS in Mode 0 finds alignments with Tanimoto $< 0.4$ in approximately 30% of cases (with an average Tanimoto difference of 0.129). Switching to Mode 5 halves this count, such that only 15% of such alignments are missed at the 0.4 threshold. However, high Tanimotos present a different picture: at a Tanimoto threshold of 0.6, Modes 0 and 5 perform almost identically (missing 70% and 68%, respectively, of 203,035 alignments). At a threshold of 0.7, Mode 5 actually *underperforms* Mode 0, missing approximately 80% of 27,029

alignments, as compared to 74% for Mode 0. Although Mode 5 has a larger number of alignments below the threshold, its average Tanimoto error on these cases is somewhat smaller (0.106 versus 0.142 for Mode 0).

### ROCS Approximation Errors

One approximation oeROCS makes by default [62] is to treat all atoms as having the same VdW radius as carbon (except protons, which are ignored). Although this often has no effect, it occasionally leads to significant changes in the overlaid pose. This is especially significant for oeROCS's "grid" mode, which *requires* that this approximation be made; the analytic and exact modes allow it to be disabled. An example is the overlay (Figure 2.3) of molecule 6899 from our database (ethyl 4-[(5-mercapto-1,3,4-thiadiazol-2-yl)thio]butanoate) against molecule 49618 (ethyl N-[2-chloro-4-(trifluoromethyl)phenyl]carbamate). This overlay, when carried out in analytic mode with exact atomic radii, correctly overlays the ring systems of the two molecules (Figure 2.3(a)). However, when carried out with the carbon approximation, oeROCS reverses the orientation of the fit molecule (Figure 2.3(b)).

A second approximation made by oeROCS (and also by PAPER) is to truncate the sum-of-products expansion of the Gaussian shape function (equation 2.3) after the second term. This prevents a combinatorial expansion in the number of terms that must be evaluated, but has the side effect that the approximate overlap will always be overestimated (because multiply-counted regions are not removed). One consequence is that the relationship between approximate overlap (as measured by the truncated objective) and exact overlap is not monotonic. Figure 2.4 illustrates this, by examining the relationship in overlays discovered by initialization modes 1 and 2 of PAPER. The starting positions of mode 2 are a strict superset of those used in mode 1. Therefore, if the relationship between the optimization objective and the exact overlap function (which is plotted) were monotonic, all the plotted points would lie on or above the black $Y = X$ line (because mode 2 would dominate mode 1). However, the scatter on either side of the line indicates that sometimes the additional starting states used in mode 2 find maxima of the approximate optimization objective that are not maxima of the true objective. This indicates that although the 2nd-order approximation is convenient for performance in both PAPER and oeROCS, it may not be sufficient to guarantee appropriate convergence behavior.

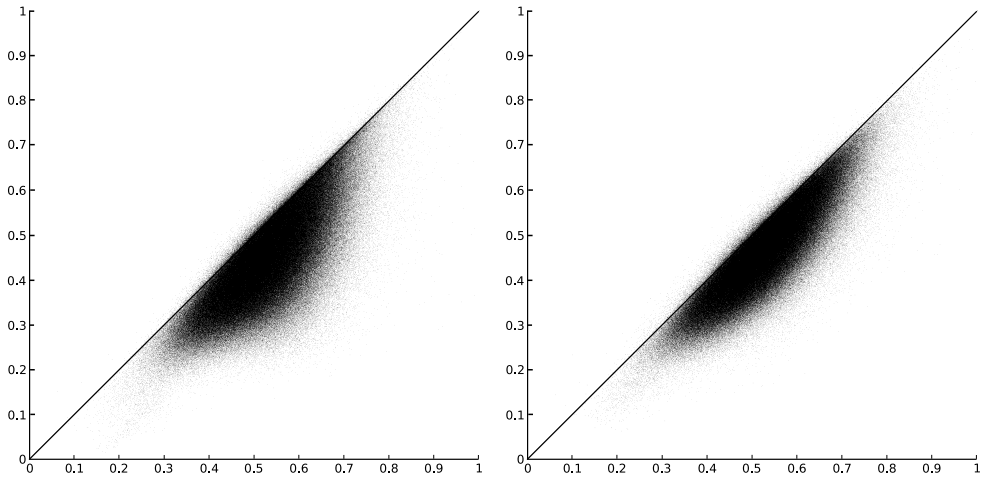


(a) Mode 0 (b) Mode 1

(c) Mode 2 (d) Mode 5

Figure 2.2: Tanimoto scores for selected PAPER initialization modes (Y) vs oeROCS (X)

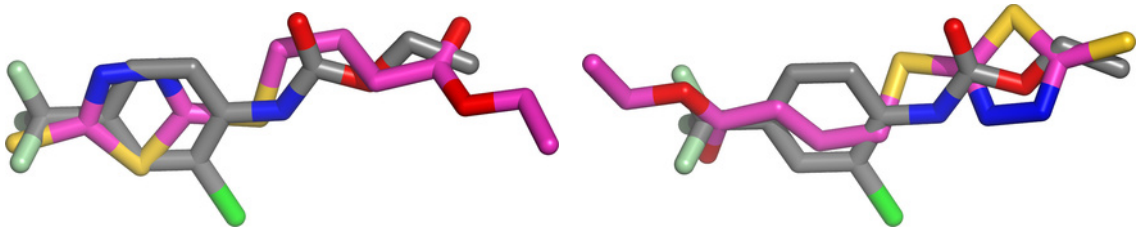

(a) Overlay of molecule 6899 against 49618 with exact radii

(b) Overlay of molecule 6899 against 49618 with carbon approximation

Figure 2.3: ROCS overlay errors with carbon-radius approximation

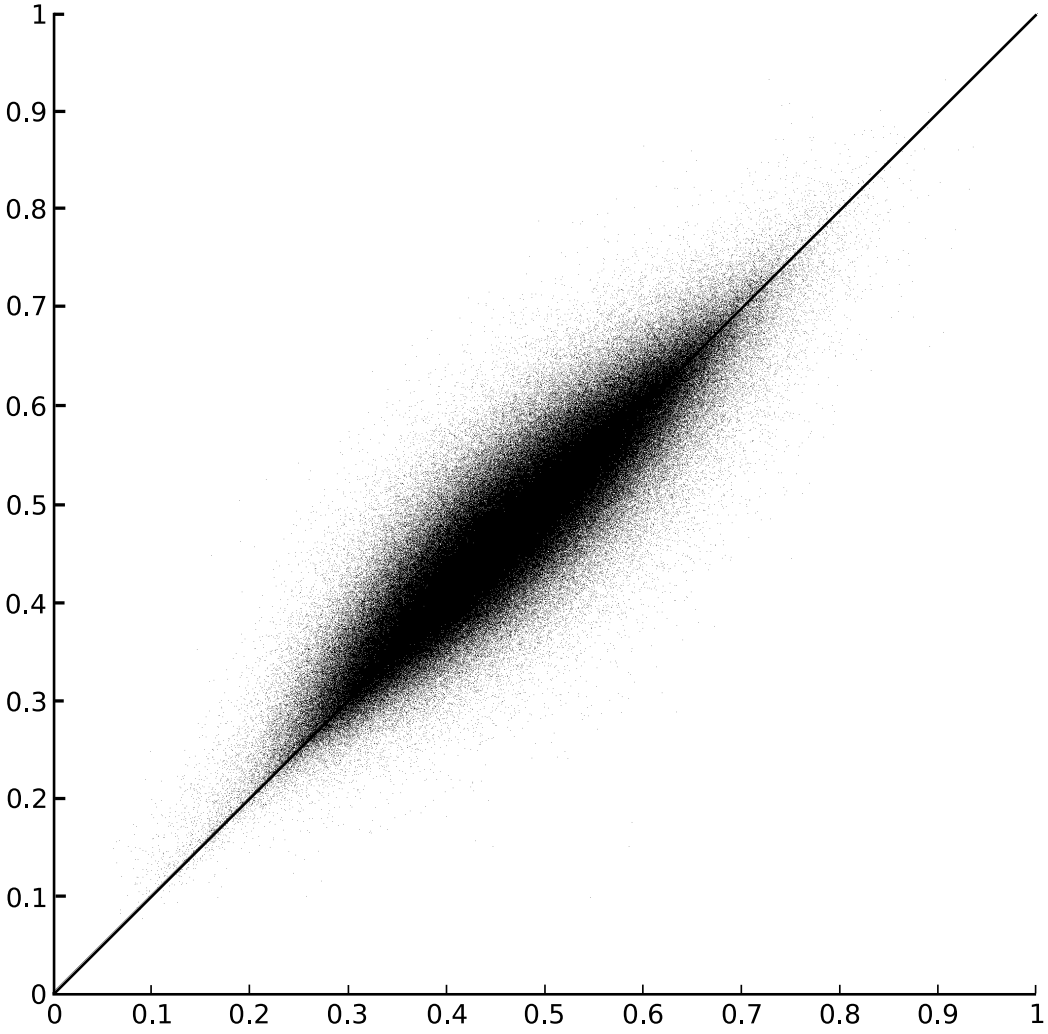


Figure 2.4: Tanimoto scores of PAPER mode 2 vs mode 1

### 2.4.3 Virtual Screening Performance vs oeROCS

To examine PAPER's performance on a standard drug-design dataset, we ran it against the DUD (Database of Useful Decoys), release 2 [44]. We compare its performance against oeROCS in its "exact" mode, for which we were able to disable the carbon-radius approximation discussed in Section 2.4.2. Additionally, we evaluate oeROCS in "grid" mode, in which the carbon-radius approximation is active. Figure 2.5 illustrates the area-under-the-ROC-curve metric (ROC AUC) on each DUD system for exact and grid oeROCS and PAPER initialization modes 0, 1, 2, and 5. In addition to the mean AUC on each system, it shows the 68% and 95% confidence intervals on the AUC metric.

On the majority of systems tested, the virtual-screening performance of PAPER in initialization modes 1, 2, or 5 is statistically indistinguishable from that of oeROCS. On several systems, indeed, PAPER with only one starting position (mode 0) is competitive with the more computationally-expensive methods. Some exceptions to these trends are highlighted in Figures 2.6 and 2.7. Figure 2.6 illustrates the impact of additional starting states on the COX-2, DHFR, HSP90, PNP, and TK test sets. For the first four, PAPER's performance was significantly improved by the addition of starting states. The TK test set is a notable anomaly in the data: although PAPER-0 and PAPER-1 are somewhat competitive with oeROCS on this test set, PAPER's performance gets worse as more starting states are added, indicating the possible impact of false maxima in the optimization objective. Figure 2.7 examines the ER antagonist, FGFr1, RXR-alpha,and SAHH test sets, in which PAPER's performance is significantly poorer than that of oeROCS.

Finally, on all sets tested, oeROCS in grid mode has performance indistinguishable from that of oeROCS in exact mode. This is likely because the overlays found under the carbon approximation have similar overlap volume to those found without the approximation, so that the similarity scores discovered are close. Because the screening protocol followed here is sensitive only to the overlap Tanimoto, and not the discovered pose, the errors discussed likely do not have a significant impact. However, they may still be significant when using ROCS-like algorithms to perform pose prediction based on known structures.

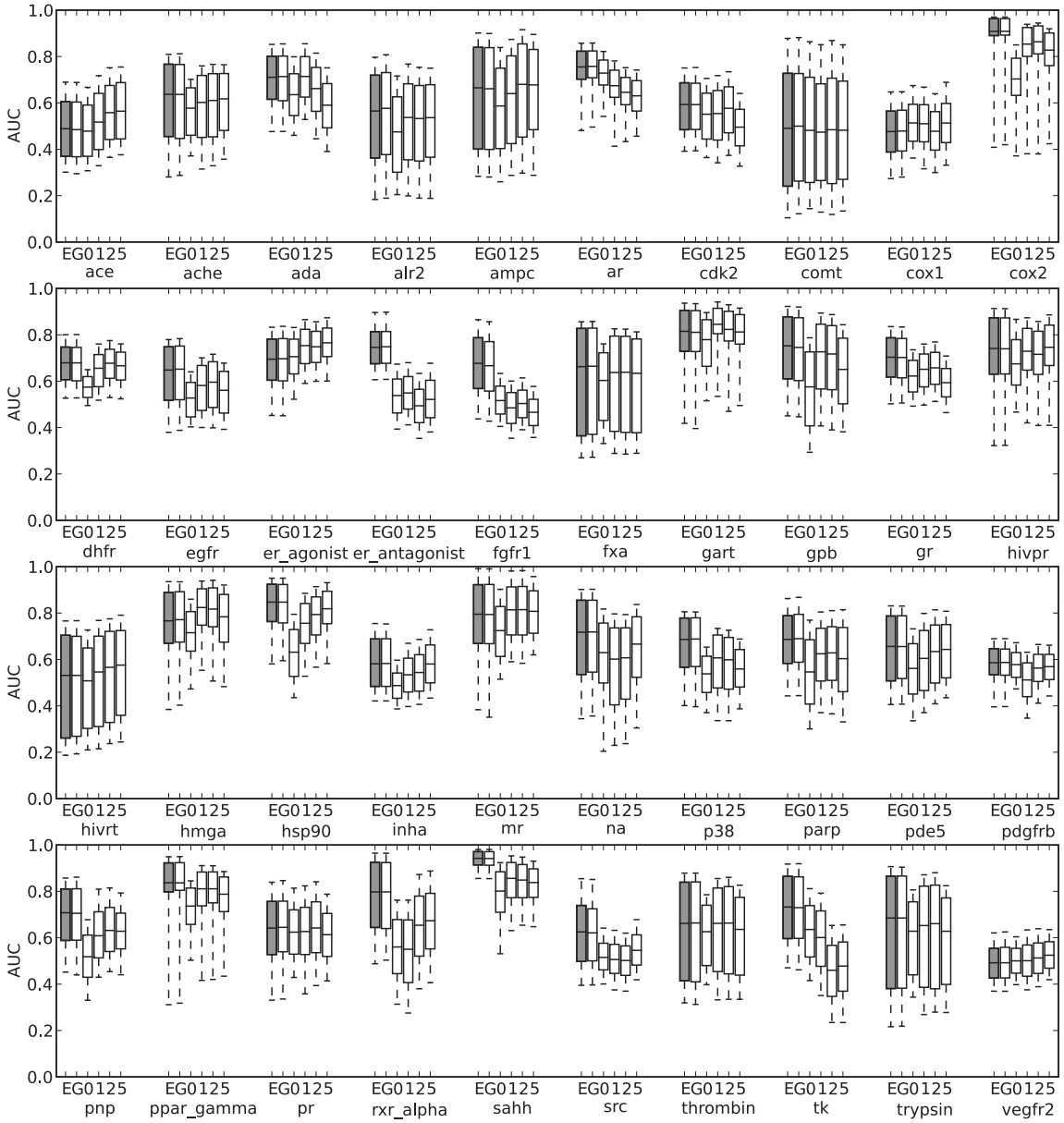


Figure 2.5: ROC AUC values on each system of the DUD test set. Reported are the mean AUC, averaged over each ligand in the system (line), the 68% confidence interval on the AUC (box), and the 95% confidence interval on the AUC (whiskers). Within each system, results are reported for for oeROCS in exact (E) and grid (G) modes, and PAPER in initialization modes 0, 1, 2, and 5 (labeled by mode number). oeROCS exact is highlighted in gray.

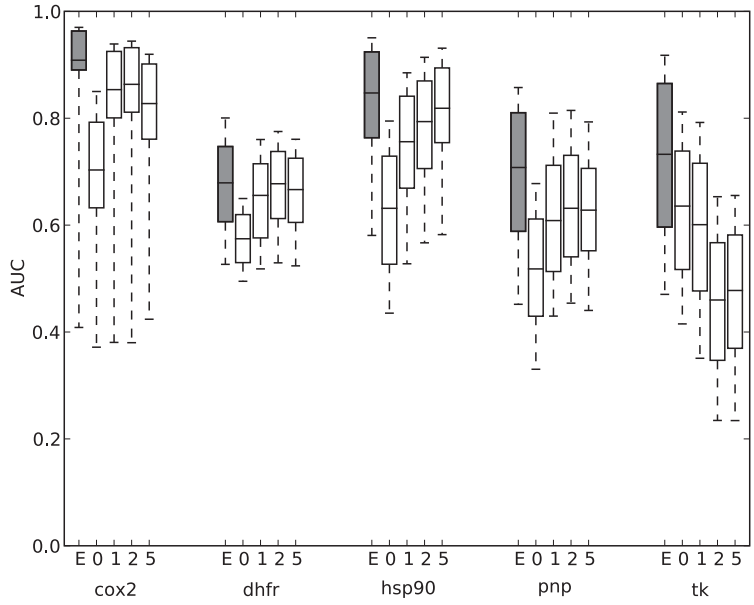


Figure 2.6: Systems for which PAPER performance varied significantly by initialization mode. Reported are the mean AUC, averaged over each ligand in the system (line), the 68% confidence interval on the AUC (box), and the 95% confidence interval on the AUC (whiskers). Within each system, results are reported for for oeROCS in exact (E) mode, highlighted in gray, and PAPER in initialization modes 0, 1, 2, and 5 (labeled by mode number).

### 2.4.4 Speed vs cpuROCS

Because the benchmarking loop iteration (Section 2.4.1) contains an insignificant ratio of CPU work to GPU work, especially in the limit of large batch sizes (the target application domain for PAPER), we separate GPU (PAPER) and CPU (cpuROCS) runtimes. Actual CPU and GPU runtimes for various batch sizes and compilers are available in Tables 2.4 to 2.10. We present three families of speedup plots. Figures 2.8 and 2.9 examine performance on the GeForce GTX 280 (NVIDIA's current top-end graphics card). Figures 2.10 and 2.11 pertain to the GeForce 8800 GTX (the high-end card of the previous generation, still in extensive use). Finally, Figure 2.12 is a "low-cost showdown", examining the speedup between a GeForce 8600GT and an Intel Celeron 420, respectively a low-end GPU and CPU of comparable cost, using the free gcc compiler. While such hardware is unlikely to be found in a dedicated computational cluster, it is widespread in mainstream computers,

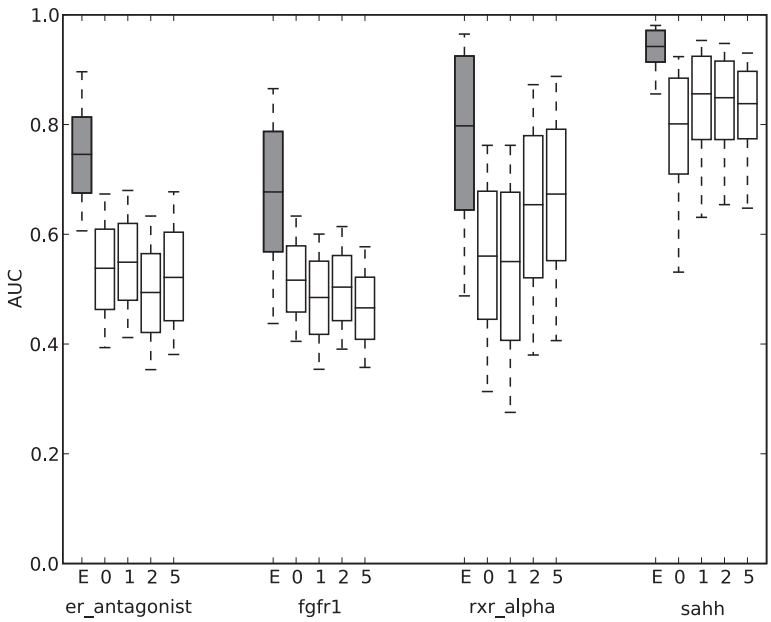


Figure 2.7: Systems for which PAPER performed significantly worse than oeROCS. Reported are the mean AUC, averaged over each ligand in the system (line), the 68% confidence interval on the AUC (box), and the 95% confidence interval on the AUC (whiskers). Within each system, results are reported for for oeROCS in exact (E) mode, highlighted in gray, and PAPER in initialization modes 0, 1, 2, and 5 (labeled by mode number).

making such information especially interesting for distributed computing applications.

Figures 2.8 and 2.9 illustrate speedups obtained using PAPER on an NVIDIA GeForce GTX 280 (NVIDIA's current top-end graphics card) versus cpuROCS on an Intel Xeon or AMD Athlon 64 (with the optimal compiler for each platform). For initialization mode 1, which is directly comparable to the original Grant et al. ROCS prescription, our data for large alignments show nearly 20x speedup relative to icc on an Intel CPU, and over 100x relative to gcc on an AMD CPU. The 8800GTX (Figures 2.10 and 2.11) also displays significant speedup: approximately 8x versus the Xeon, and over 40x versus the Athlon. Finally, the low-cost hardware comparison (Figure 2.12) shows that even at the same (low) price point, GPU hardware can dramatically outperform CPU implementations, with 35x speedup.

These performance gains scale, as expected, with both the number of molecules that are batched into each PAPER optimization as well as the size of the molecules themselves. Two

causes explain the shape of the performance curve. The first is unique to the case in which the number of molecule-orientation pairs (not the size of the molecules themselves) is too small. Below a critical number of thread blocks (the number of SMs on the GPU, e.g. 16 on the 8800GTX or 30 on the GTX280), there is not at least one block per SM on the GPU. Therefore, GPU resources go unused. It is important, however, to have more than one thread block (i.e., molecule-orientation pair) per SM, as the GPU will run multiple blocks on each SM, and switch among them when one stalls (e.g., due to memory access). A larger number of blocks helps hide latency in each, ensuring maximum utilization.

The second cause impacts performance both in the case in which the number of starting states is too small and in which the molecules themselves have few atoms. In these cases, the actual optimization can be completed extremely quickly by the GPU, and the limiting factor in performance becomes the transfer of data between the CPU and GPU.

### 2.4.5 Speed vs oeROCS

For completeness, we also measured the speed of various PAPER modes against that of OpenEye ROCS (Table 2.3), on both the Intel Celeron and AMD Athlon 64 architectures. Figure 2.13 presents the expected speedup for a GeForce GTX 280 versus oeROCS on the higher-performing Athlon. Because the ROCS initialization algorithm is not public, it is not clear which mode presents the most appropriate comparison. Mode 1, which corresponds to the publicly-disclosed part of ROCS, illustrates the general trend: PAPER offers significant speedups with respect to OpenEye ROCS, especially for medium- and large-sized molecules. In Mode 1, PAPER attains speedups of approximately 30-35x on medium and large molecules, and 5-10x for small molecules. The dramatic difference in performance with very small molecules is certainly partly due to the effects mentioned in section 2.4.4; it may also be the case that oeROCS does not use as many starting positions for tiny molecules, and thus does not suffer the linear performance penalty from adding more starting states.

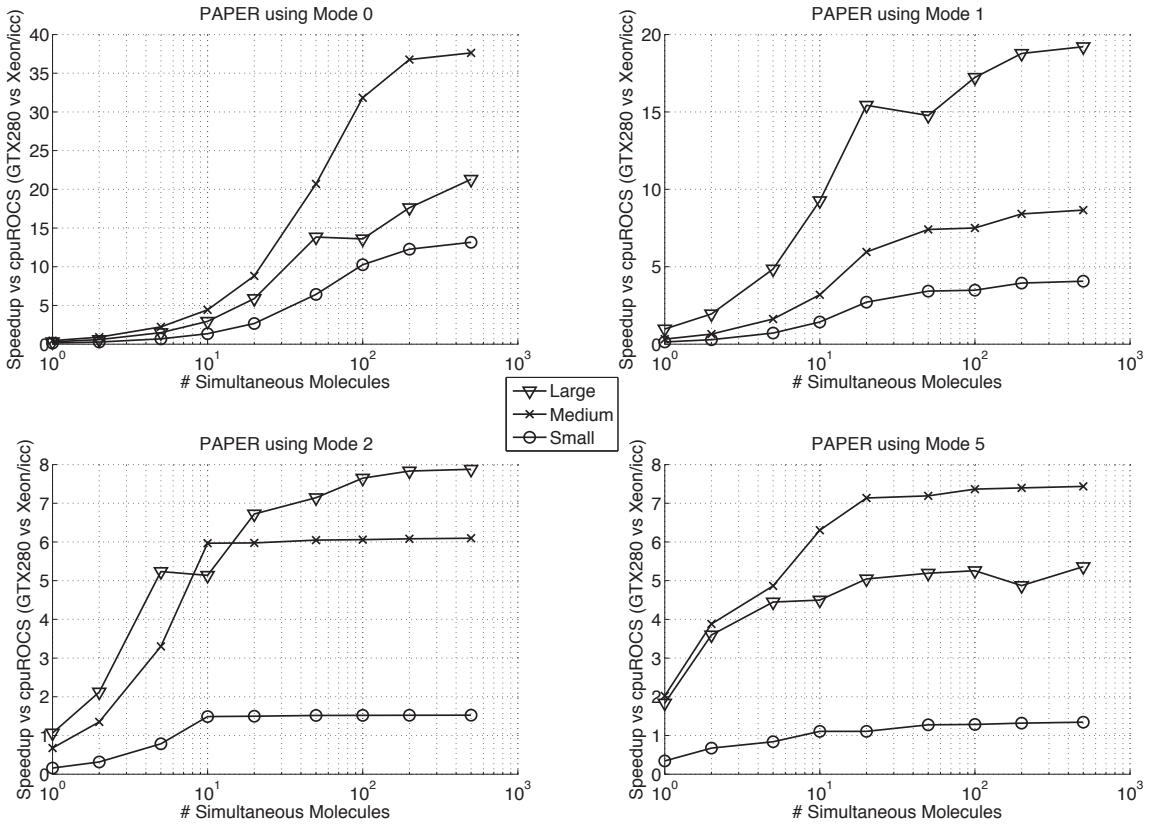


Figure 2.8: PAPER speedup vs cpuROCS: GTX 280 vs Xeon/icc

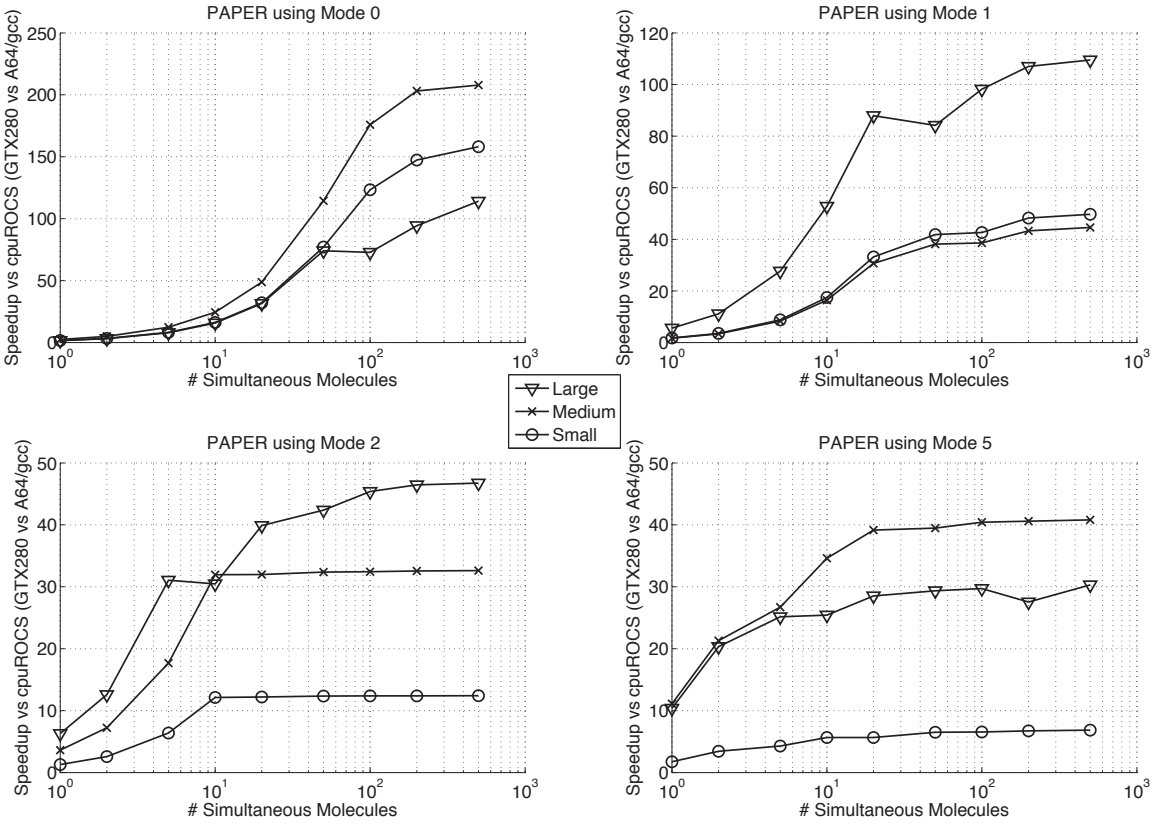


Figure 2.9: PAPER speedup vs cpuROCS: GTX 280 vs Athlon 64 X2/gcc

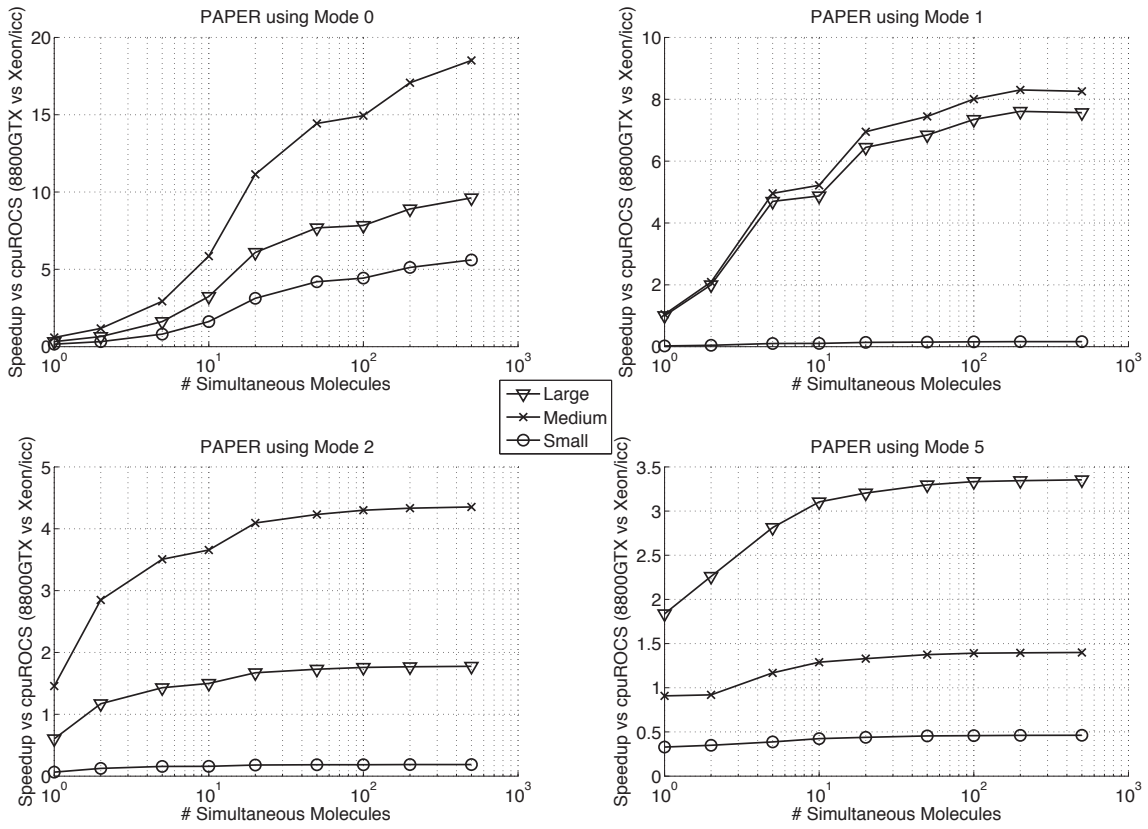


Figure 2.10: PAPER speedup vs cpuROCS: 8800GTX vs Xeon/icc

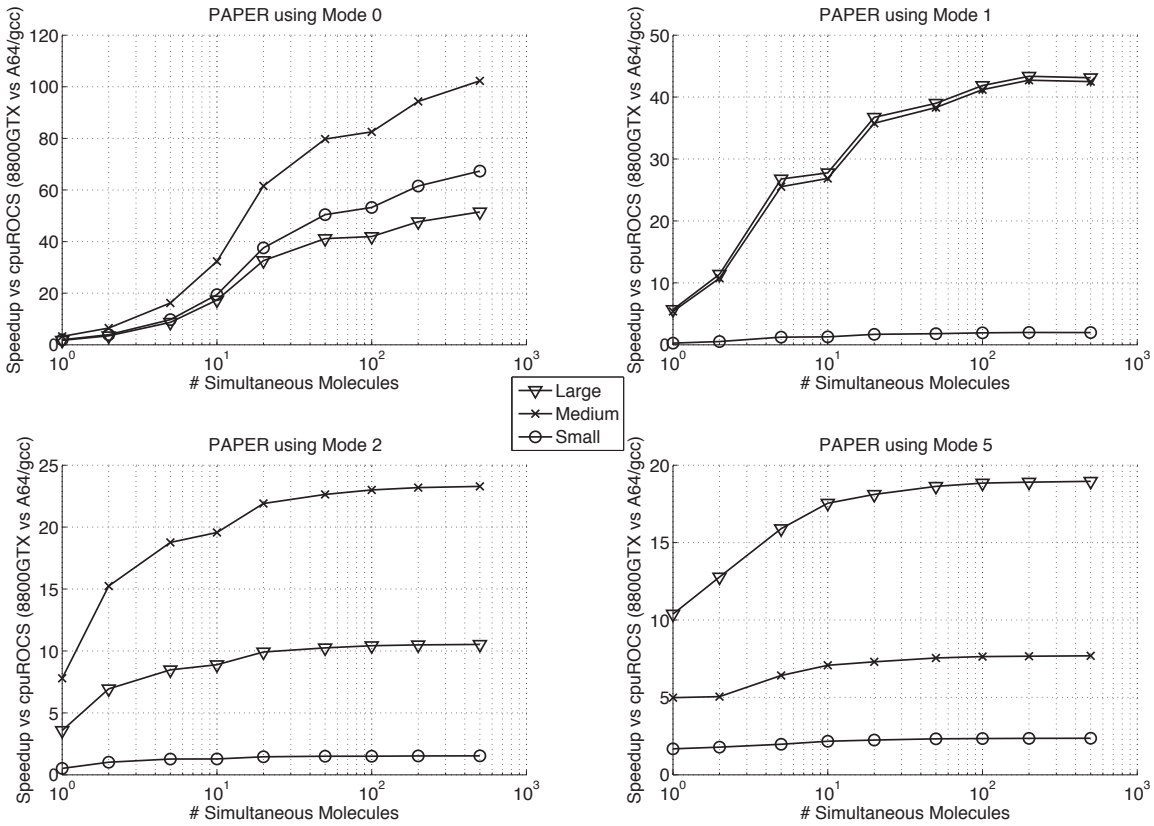


Figure 2.11: PAPER speedup vs cpuROCS: 8800GTX vs Athlon 64 X2/gcc

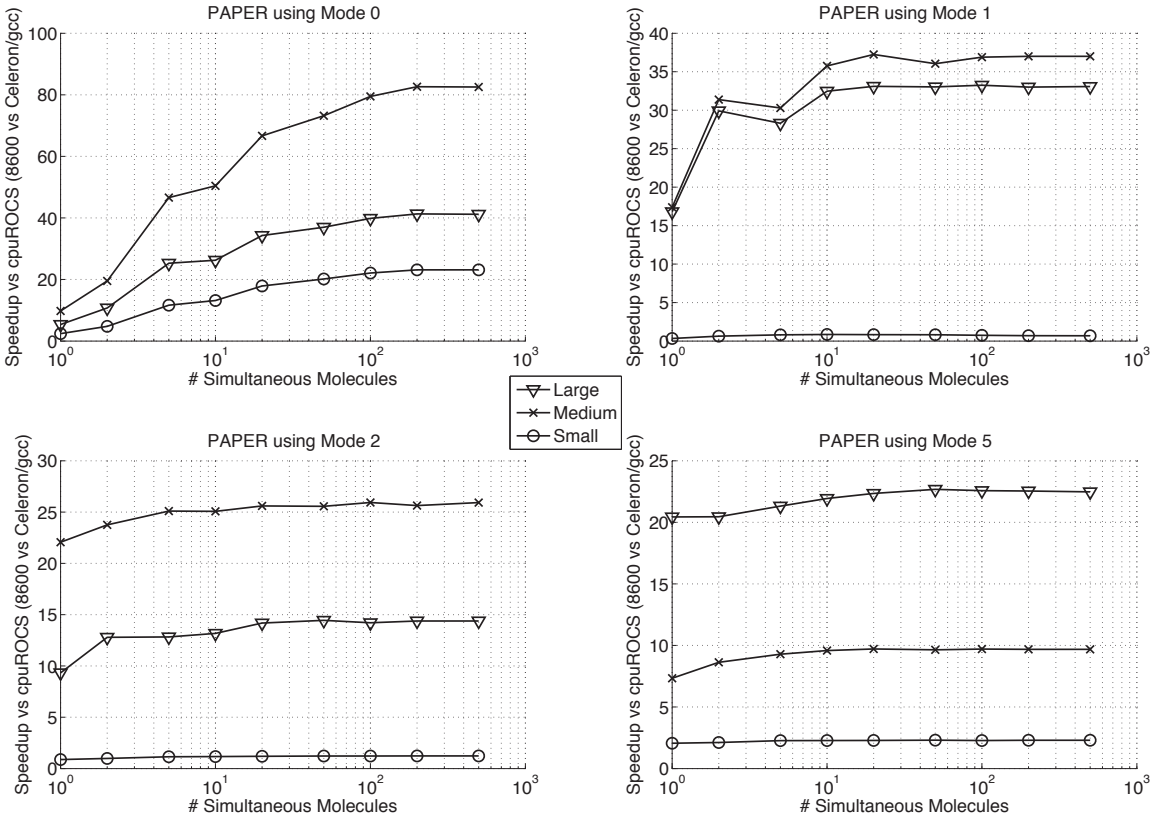


Figure 2.12: PAPER speedup vs cpuROCS: 8600GT vs Celeron/gcc

| CPU | Molecule Size | Runtime (per alignment, ms) |
|---|---|---|
| Intel Celeron 420 1.6GHz | small | 1.38 |
| | medium | 9.91 |
| | large | 15.94 |
| AMD Athlon 64 3800+ 2.4GHz | small | 0.86 |
| | medium | 6.54 |
| | large | 11.01 |

Table 2.3: oeROCS performance in Exact mode. Times reported are time per alignment.

## 2.5 Conclusions

Structural search over a database for molecules similar to a query structure is a canonical embarrassingly parallel problem. PAPER, our GPU-accelerated overlay optimizer, has demonstrated speedup of one to two orders of magnitude on commodity hardware, relative to a CPU-based reference implementation of the same algorithm, and 5-35x speedup against the commercial OpenEye ROCS implementation. Optimal performance is achieved in the case in which at least hundreds of molecules must be compared against each query structure, making the PAPER method extremely well-suited for large-scale database search and screening applications.

Based on the results of our tests, we recommend the use of different initialization modes for different applications. For rapid virtual screening, we recommend the use of PAPER in initialization mode 1 (the original Grant and Pickup prescription). PAPER's mode 1 offers order-of-magnitude speedup over oeROCS (Figure 2.13), with comparable accuracy on most systems tested (Figure 2.5). For pose prediction, we recommend the use of a higher-precision initialization mode — mode 2 or 5 — as these occasionally find orientations of greater overlap than those found in mode 1 (Figure 2.2).

Although the speedup from a straightforward GPU implementation is already significant, there is scope for further acceleration. While we have mostly eliminated latency due to global memory access in the PAPER kernel, little effort has been spent on minimizing latency due to shared memory bank conflicts, which can significantly reduce performance [65]. Additionally, the current structure of PAPER may not be ideal for the resources available in the NVIDIA architecture. In particular, the inner loops of the overlap and gradient

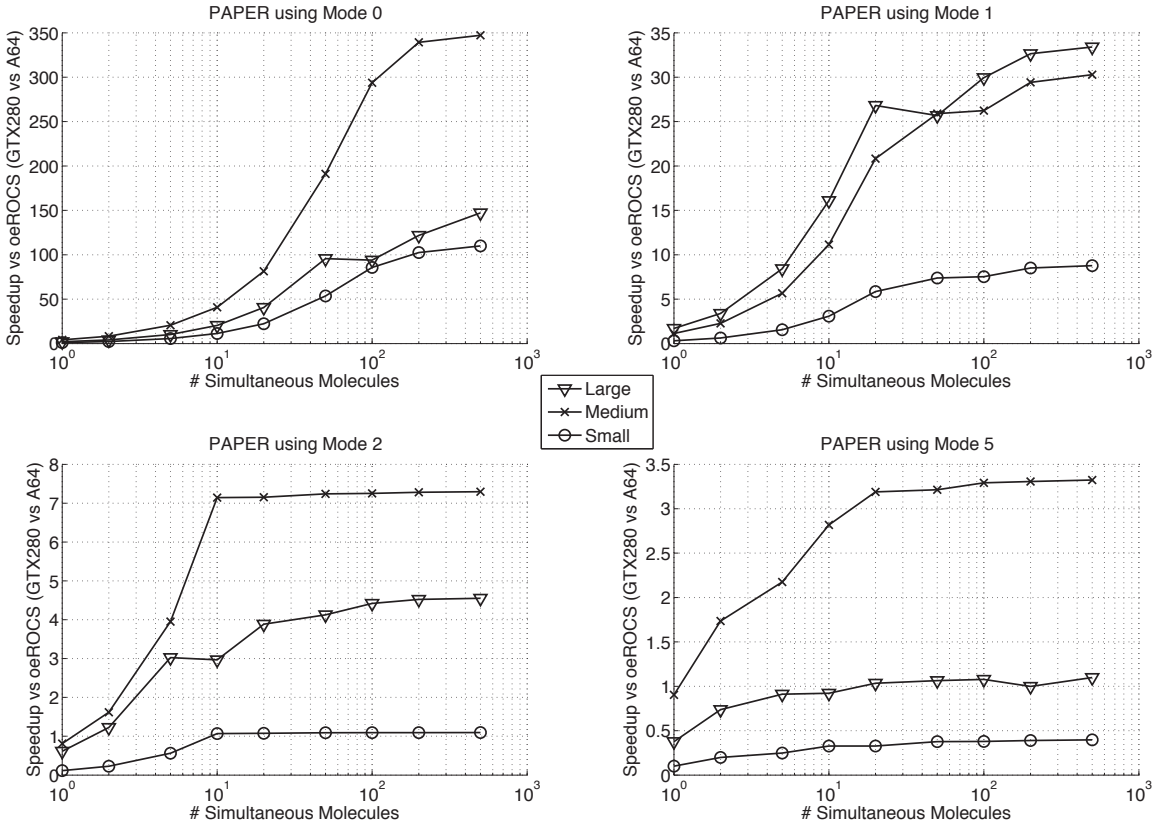


Figure 2.13: PAPER speedup vs oeROCS: GTX 280 vs Athlon 64 3800+

calculations evaluate an exponential function (equation 2.4) in each thread. However, exponential evaluations in each thread block are handled by not the 8 SPs, but rather by the 2 special function units (SFUs). This reduction in parallelism reduces the arithmetic throughput of the PAPER kernel.

Further acceleration of the algorithm may be possible by utilizing features of the NVIDIA hardware which we do not currently use — namely, the constant and texture memories. Both of these are cached read-only memories, from which it may be possible to build an efficient lookup table-based implementation of the exponential function. Although the constant memory has much lower latency than the texture memory (cached reads from constant memory can be as fast as register access), the texture memory has the advantage that it can perform linear interpolation in hardware essentially for “free”. Using these memory features on the hardware may reduce the pressure on the SFUs and thereby further accelerate the

algorithm.

An alternative use for the increased computational power granted by GPU hardware would be to increase the accuracy of the overlap optimization. Our results indicate that approximations currently made to accelerate overlap-optimization calculations (specifically, the carbon-radius approximation, and the truncation of equation 2.3 to second order) negatively impact the quality of resulting poses. Rather than simply speeding up runtime, GPU throughput could be used to evaluate more complex models (e.g., higher-order approximations to equation 2.3) to increase accuracy. We anticipate that the release of PAPER as an open-source code will allow it to be used as an open platform for further development of GPU implementations of molecular shape overlay. PAPER is available for download at https://simtk.org/home/paper/.

## 2.6 Acknowledgments

We would like to thank Kim Branson and John Chodera for helpful discussion and Philip Guo for reading the manuscript. We acknowledge support from an NSF graduate fellowship (to ISH), an NSF grant for Cyberinfrastructure NSF CHE-0535616 (to VSP), and NSF award CNS-0619926 for computer resources.

## 2.7 Appendix: Rotational gradients for shape overlay

Grant et al. provide equations for the translational derivatives of Gaussian volume overlaps [35], and suggest that quaternions are a good coordinate system in which to implement rotational optimization [33], but do not provide derivations of the overlap derivative with respect to quaternion rotation. This appendix derives the rotational derivatives.

In the following sections, it is assumed that the reference molecule is stationary; thus, the overlap is a function of fit molecule coordinates alone, which are in turn a function of the 7-dimensional rigid-body transformation vector. This transformation vector will be represented as $T = [t_x, t_y, t_z, q, r, s, u]$, where the first three coordinates are the translation and the final four the rotation quaternion. We adopt the quaternion convention of Griewank et al. [36]. Given an atomic coordinate $\vec{c} = (x, y, z, 1)$ (with the final 1 representing a

homogeneous coordinate, allowing affine transformations to be expressed in matrix form), the transformed $T(\vec{c})$ can be represented as $M\vec{c}$, with M defined by:

$$\frac{1}{||T||^2}\begin{bmatrix} (r^2-s^2-u^2+q^2) & 2(rs+uq) & 2(ru-sq) & t_x \\ 2(rs-uq) & (-r^2+s^2-u^2+q^2) & 2(su+rq) & t_y \\ 2(ru+sq) & 2(su-rq) & (-r^2-s^2+u^2+q^2) & t_z \\ 0 & 0 & 0 & 1 \end{bmatrix}$$

### 2.7.1 Gradient of volume $V$ with respect to transform $T$

The overlap volume is a function of the coordinates of each fit atom, $x_i$, $y_i$, and $z_i$. The gradient is given by Grant et al. as a function of these coordinates; transform it to the gradient as a function of transformation coordinates $\vec{t} = (t_x, t_y, t_z, q, r, s, u)$ via the chain rule:

$$\nabla V(\vec{t}) = \left[\frac{\partial V}{\partial x_1}, \frac{\partial V}{\partial x_2}, \cdots, \frac{\partial V}{\partial x_N}, \frac{\partial V}{\partial y_1}, \frac{\partial V}{\partial y_2}, \cdots, \frac{\partial V}{\partial y_N}, \frac{\partial V}{\partial z_1}, \frac{\partial V}{\partial z_2}, \cdots, \frac{\partial V}{\partial z_N}\right] \cdot \begin{bmatrix} \frac{\partial x_1}{\partial t_x} & \frac{\partial x_1}{\partial t_y} & \frac{\partial x_1}{\partial t_z} & \frac{\partial x_1}{\partial q} & \frac{\partial x_1}{\partial r} & \frac{\partial x_1}{\partial s} & \frac{\partial x_1}{\partial u} \\ \frac{\partial x_2}{\partial t_x} & \vdots & \vdots & \vdots & \vdots & \vdots & \vdots \\ \vdots & \vdots & \vdots & \vdots & \vdots & \vdots & \vdots \\ \frac{\partial z_N}{\partial t_x} & \frac{\partial z_N}{\partial t_y} & \frac{\partial z_N}{\partial t_z} & \frac{\partial z_N}{\partial q} & \frac{\partial z_N}{\partial r} & \frac{\partial z_N}{\partial s} & \frac{\partial z_N}{\partial u} \end{bmatrix}$$

$$\begin{aligned} \nabla V(\vec{t}) &= \left[\frac{\partial V}{\partial x_1}\frac{\partial x_1}{\partial t_x} + \frac{\partial V}{\partial x_2}\frac{\partial x_2}{\partial t_x} + \cdots, \frac{\partial V}{\partial x_1}\frac{\partial x_1}{\partial t_y} + \cdots, \cdots\right] \\ &= \sum_{k=1}^{N}\left[\frac{\partial V}{\partial x_k}\frac{\partial x_k}{\partial t_x} + \frac{\partial V}{\partial y_k}\frac{\partial y_k}{\partial t_x} + \cdots, \cdots\right] \quad (\frac{\partial \alpha_k}{\partial t_\beta} = \delta_{\alpha\beta}) \\ &= \sum_{k=1}^{N}\left[\frac{\partial V}{\partial x_k}, \frac{\partial V}{\partial y_k}, \frac{\partial V}{\partial z_k}, \frac{\partial V}{\partial x_k}\frac{\partial x_k}{\partial q} + \frac{\partial V}{\partial y_k}\frac{\partial y_k}{\partial q} + \frac{\partial V}{\partial z_k}\frac{\partial z_k}{\partial q}, \cdots (\text{for } r, s, u)\right] \end{aligned}$$

Where $\delta$ is the Kronecker delta.

Defining $\vec{\chi}_k = [x_k, y_k, z_k]$, we reach the following expression for the volume gradient,

expressed as a summation over each fit atom:

$$\nabla V\left(\vec{t}\right) = \sum_{k=1}^{N} \Bigg[ \frac{\partial V}{\partial x_k}, \frac{\partial V}{\partial y_k}, \frac{\partial V}{\partial z_k}, \nabla V(\vec{\chi_k}) \cdot \nabla \vec{\chi_k}(q), \nabla V(\vec{\chi_k}) \cdot \nabla \vec{\chi_k}(r), \quad \nabla V(\vec{\chi_k}) \cdot \nabla \vec{\chi_k}(s), \quad \nabla V(\vec{\chi_k}) \cdot \nabla \vec{\chi_k}(u) \Bigg]$$

### 2.7.2 Coordinate derivatives: $\nabla \vec{\chi}_k(T)$

We begin by differentiating the transformation matrix $M$. Assuming that the quaternion magnitude $||T||^2 = 1$,

$$\frac{\partial M}{\partial q} = \begin{bmatrix} 2q & 2u & -2s \\ -2u & 2q & 2r \\ 2s & -2r & 2q \end{bmatrix} \qquad \frac{\partial M}{\partial r} = \begin{bmatrix} 2r & 2s & 2u \\ 2s & -2r & 2q \\ 2u & -2q & -2r \end{bmatrix}$$

$$\frac{\partial M}{\partial s} = \begin{bmatrix} -2s & 2r & -2q \\ 2r & 2s & 2u \\ 2q & 2u & -2s \end{bmatrix} \qquad \frac{\partial M}{\partial u} = \begin{bmatrix} -2u & 2q & 2r \\ -2q & -2u & 2s \\ 2r & 2s & 2u \end{bmatrix}$$

The following coordinate derivatives then follow by matrix multiplication:

$$\frac{\partial x_k}{\partial q} = 2\left(qx_k + uy_k - sz_k\right) \qquad \frac{\partial x_k}{\partial r} = 2\left(rx_k + sy_k + uz_k\right)$$
$$\frac{\partial y_k}{\partial q} = 2\left(-ux_k + qy_k + rz_k\right) \qquad \frac{\partial y_k}{\partial r} = 2\left(sx_k - ry_k + qz_k\right)$$
$$\frac{\partial z_k}{\partial q} = 2\left(sx_k - ry_k + qz_k\right) \qquad \frac{\partial z_k}{\partial r} = 2\left(ux_k - qy_k - rz_k\right)$$
$$\frac{\partial x_k}{\partial s} = 2\left(-sx_k + ry_k - qz_k\right) \qquad \frac{\partial x_k}{\partial u} = 2\left(-ux_k + qy_k + rz_k\right)$$
$$\frac{\partial y_k}{\partial s} = 2\left(rx_k + sy_k + uz_k\right) \qquad \frac{\partial y_k}{\partial u} = 2\left(-qx_k - uy_k + sz_k\right)$$
$$\frac{\partial z_k}{\partial s} = 2\left(qx_k + uy_k - sz_k\right) \qquad \frac{\partial z_k}{\partial u} = 2\left(rx_k + sy_k + uz_k\right)$$

Note the following equalities, which imply that only 4 of the quaternion derivatives

actually require calculation more complicated than equality or negation:

$$\begin{aligned}
\frac{\partial x_k}{\partial q} &= \frac{\partial z_k}{\partial s} = -\frac{\partial y_k}{\partial u} \\
\frac{\partial x_k}{\partial r} &= \frac{\partial y_k}{\partial s} = \frac{\partial z_k}{\partial u} \\
-\frac{\partial x_k}{\partial s} &= \frac{\partial z_k}{\partial q} = \frac{\partial y_k}{\partial r} \\
\frac{\partial x_k}{\partial u} &= \frac{\partial y_k}{\partial q} = -\frac{\partial z_k}{\partial r}
\end{aligned}$$

| CPU | Compiler | Molecule Size | PAPER Mode | Runtime (per alignment, ms) | Runtime (per start, ms) |
|---|---|---|---|---|---|
| Intel Celeron 420 1.6GHz | gcc | small | 0 | 1.82 | 1.82 |
| | | | 1 | 7.03 | 1.76 |
| | | | 2 | 20.49 | 1.71 |
| | | | 5 | 50.20 | 1.62 |
| | | medium | 0 | 13.74 | 13.74 |
| | | | 1 | 35.89 | 8.97 |
| | | | 2 | 102.45 | 8.54 |
| | | | 5 | 278.31 | 8.98 |
| | | large | 0 | 30.12 | 30.12 |
| | | | 1 | 121.25 | 30.31 |
| | | | 2 | 393.57 | 32.80 |
| | | | 5 | 1007.61 | 32.50 |
| | icc | small | 0 | 0.14 | 0.14 |
| | | | 1 | 0.57 | 0.14 |
| | | | 2 | 1.74 | 0.14 |
| | | | 5 | 4.22 | 0.14 |
| | | medium | 0 | 1.02 | 1.02 |
| | | | 1 | 2.72 | 0.68 |
| | | | 2 | 7.92 | 0.66 |
| | | | 5 | 21.40 | 0.69 |
| | | large | 0 | 2.31 | 2.31 |
| | | | 1 | 9.19 | 2.30 |
| | | | 2 | 27.77 | 2.31 |
| | | | 5 | 78.24 | 2.52 |

Table 2.4: cpuROCS performance for Celeron 420. Times reported are time per alignment over all starting positions (“per alignment”) or per starting position (“per start”).

| CPU | Compiler | Molecule Size | PAPER Mode | Runtime (per alignment, ms) | Runtime (per start, ms) |
|---|---|---|---|---|---|
| Intel Xeon E5345 2.33GHz | gcc | small | 0 | 1.16 | 1.16 |
| | | | 1 | 4.49 | 1.12 |
| | | | 2 | 13.04 | 1.09 |
| | | | 5 | 32.01 | 1.03 |
| | | medium | 0 | 8.78 | 8.78 |
| | | | 1 | 22.84 | 5.71 |
| | | | 2 | 65.50 | 5.46 |
| | | | 5 | 177.16 | 5.71 |
| | | large | 0 | 19.26 | 19.26 |
| | | | 1 | 76.96 | 19.24 |
| | | | 2 | 251.74 | 20.98 |
| | | | 5 | 644.06 | 20.78 |
| | icc | small | 0 | 0.10 | 0.10 |
| | | | 1 | 0.40 | 0.10 |
| | | | 2 | 1.20 | 0.10 |
| | | | 5 | 2.91 | 0.09 |
| | | medium | 0 | 0.71 | 0.71 |
| | | | 1 | 1.87 | 0.47 |
| | | | 2 | 5.46 | 0.46 |
| | | | 5 | 14.63 | 0.47 |
| | | large | 0 | 1.59 | 1.59 |
| | | | 1 | 6.33 | 1.58 |
| | | | 2 | 19.06 | 1.59 |
| | | | 5 | 53.72 | 1.73 |

Table 2.5: cpuROCS performance for Xeon E5345. Times reported are time per alignment over all starting positions (“per alignment”) or per starting position (“per start”)

| CPU | Compiler | Molecule Size | PAPER Mode | Runtime (per alignment, ms) | Runtime (per start, ms) |
|---|---|---|---|---|---|
| AMD Athlon 64 X2 4800+ 2.5GHz | gcc | small | 0 | 1.24 | 1.24 |
| | | | 1 | 4.87 | 1.22 |
| | | | 2 | 9.75 | 0.81 |
| | | | 5 | 14.85 | 0.48 |
| | | medium | 0 | 3.91 | 3.91 |
| | | | 1 | 9.62 | 2.41 |
| | | | 2 | 29.23 | 2.44 |
| | | | 5 | 80.29 | 2.59 |
| | | large | 0 | 8.53 | 8.53 |
| | | | 1 | 36.09 | 9.02 |
| | | | 2 | 113.06 | 9.42 |
| | | | 5 | 303.64 | 9.79 |

Table 2.6: cpuROCS performance for Athlon 64 X2 4800+. Times reported are time per alignment over all starting positions (“per alignment”) or per starting position (“per start”).

| PAPER Mode | Molecule Size | GPU | Batch Size | Runtime (per alignment, ms) | Runtime (per start, ms) |
|---|---|---|---|---|---|
| 0 (1 starting orientation) | small | 8600GT (32 SP) | 1 | 0.76 | 0.76 |
| | | | 20 | 0.10 | 0.10 |
| | | | 100 | 0.08 | 0.08 |
| | | | 500 | 0.08 | 0.08 |
| | | 8800GTX (128 SP) | 1 | 0.63 | 0.63 |
| | | | 20 | 0.03 | 0.03 |
| | | | 100 | 0.02 | 0.02 |
| | | | 500 | 0.02 | 0.02 |
| | | GTX280 (240 SP) | 1 | 0.75 | 0.75 |
| | | | 20 | 0.04 | 0.04 |
| | | | 100 | 0.01 | 0.01 |
| | | | 500 | 0.01 | 0.01 |
| | medium | 8600GT (32 SP) | 1 | 1.41 | 1.41 |
| | | | 20 | 0.21 | 0.21 |
| | | | 100 | 0.17 | 0.17 |
| | | | 500 | 0.17 | 0.17 |
| | | 8800GTX (128 SP) | 1 | 1.21 | 1.21 |
| | | | 20 | 0.06 | 0.06 |
| | | | 100 | 0.05 | 0.05 |
| | | | 500 | 0.04 | 0.04 |
| | | GTX280 (240 SP) | 1 | 1.58 | 1.58 |
| | | | 20 | 0.08 | 0.08 |
| | | | 100 | 0.02 | 0.02 |
| | | | 500 | 0.02 | 0.02 |
| | large | 8600GT (32 SP) | 1 | 5.60 | 5.60 |
| | | | 20 | 0.88 | 0.88 |
| | | | 100 | 0.76 | 0.76 |
| | | | 500 | 0.73 | 0.73 |
| | | 8800GTX (128 SP) | 1 | 4.91 | 4.91 |
| | | | 20 | 0.26 | 0.26 |
| | | | 100 | 0.20 | 0.20 |
| | | | 500 | 0.17 | 0.17 |
| | | GTX280 (240 SP) | 1 | 5.38 | 5.38 |
| | | | 20 | 0.27 | 0.27 |
| | | | 100 | 0.12 | 0.12 |
| | | | 500 | 0.07 | 0.07 |

Table 2.7: PAPER performance for initialization mode 0 on selected batch sizes. Times reported are time per alignment over all starting positions (“per alignment”) or per starting position (“per start”).

| PAPER Mode | Molecule Size | GPU | Batch Size | Runtime (per alignment, ms) | Runtime (per start, ms) |
|---|---|---|---|---|---|
| 1 (4 starting orientations) | small | 8600GT (32 SP) | 1 | 21.25 | 5.31 |
| | | | 20 | 8.52 | 2.13 |
| | | | 100 | 9.42 | 2.35 |
| | | | 500 | 10.22 | 2.55 |
| | | 8800GTX (128 SP) | 1 | 18.73 | 4.68 |
| | | | 20 | 2.89 | 0.72 |
| | | | 100 | 2.54 | 0.63 |
| | | | 500 | 2.46 | 0.62 |
| | | GTX280 (240 SP) | 1 | 2.76 | 0.69 |
| | | | 20 | 0.15 | 0.04 |
| | | | 100 | 0.11 | 0.03 |
| | | | 500 | 0.10 | 0.02 |
| | medium | 8600GT (32 SP) | 1 | 2.06 | 0.52 |
| | | | 20 | 0.96 | 0.24 |
| | | | 100 | 0.97 | 0.24 |
| | | | 500 | 0.97 | 0.24 |
| | | 8800GTX (128 SP) | 1 | 1.79 | 0.45 |
| | | | 20 | 0.27 | 0.07 |
| | | | 100 | 0.23 | 0.06 |
| | | | 500 | 0.23 | 0.06 |
| | | GTX280 (240 SP) | 1 | 5.75 | 1.44 |
| | | | 20 | 0.31 | 0.08 |
| | | | 100 | 0.25 | 0.06 |
| | | | 500 | 0.22 | 0.05 |
| | large | 8600GT (32 SP) | 1 | 7.22 | 1.80 |
| | | | 20 | 3.66 | 0.92 |
| | | | 100 | 3.65 | 0.91 |
| | | | 500 | 3.67 | 0.92 |
| | | 8800GTX (128 SP) | 1 | 6.34 | 1.58 |
| | | | 20 | 0.98 | 0.25 |
| | | | 100 | 0.86 | 0.22 |
| | | | 500 | 0.84 | 0.21 |
| | | GTX280 (240 SP) | 1 | 6.48 | 1.62 |
| | | | 20 | 0.41 | 0.10 |
| | | | 100 | 0.37 | 0.09 |
| | | | 500 | 0.33 | 0.08 |

Table 2.8: PAPER performance for initialization mode 1 on selected batch sizes. Times reported are time per alignment over all starting positions (“per alignment”) or per starting position (“per start”).

| PAPER Mode | Molecule Size | GPU | Batch Size | Runtime (per alignment, ms) | Runtime (per start, ms) |
|---|---|---|---|---|---|
| 2 (12 starting orientations) | small | 8600GT (32 SP) | 1 | 23.26 | 1.94 |
| | | | 20 | 17.11 | 1.43 |
| | | | 100 | 16.74 | 1.40 |
| | | | 500 | 16.67 | 1.39 |
| | | 8800GTX (128 SP) | 1 | 18.74 | 1.56 |
| | | | 20 | 6.69 | 0.56 |
| | | | 100 | 6.49 | 0.54 |
| | | | 500 | 6.38 | 0.53 |
| | | GTX280 (240 SP) | 1 | 7.56 | 0.63 |
| | | | 20 | 0.80 | 0.07 |
| | | | 100 | 0.79 | 0.07 |
| | | | 500 | 0.78 | 0.07 |
| | medium | 8600GT (32 SP) | 1 | 4.64 | 0.39 |
| | | | 20 | 4.00 | 0.33 |
| | | | 100 | 3.95 | 0.33 |
| | | | 500 | 3.95 | 0.33 |
| | | 8800GTX (128 SP) | 1 | 3.75 | 0.31 |
| | | | 20 | 1.33 | 0.11 |
| | | | 100 | 1.27 | 0.11 |
| | | | 500 | 1.26 | 0.10 |
| | | GTX280 (240 SP) | 1 | 8.07 | 0.67 |
| | | | 20 | 0.91 | 0.08 |
| | | | 100 | 0.90 | 0.08 |
| | | | 500 | 0.90 | 0.07 |
| | large | 8600GT (32 SP) | 1 | 42.21 | 3.52 |
| | | | 20 | 27.75 | 2.31 |
| | | | 100 | 27.69 | 2.31 |
| | | | 500 | 27.37 | 2.28 |
| | | 8800GTX (128 SP) | 1 | 31.59 | 2.63 |
| | | | 20 | 11.41 | 0.95 |
| | | | 100 | 10.85 | 0.90 |
| | | | 500 | 10.74 | 0.89 |
| | | GTX280 (240 SP) | 1 | 17.94 | 1.50 |
| | | | 20 | 2.83 | 0.24 |
| | | | 100 | 2.49 | 0.21 |
| | | | 500 | 2.42 | 0.20 |

Table 2.9: PAPER performance for initialization mode 2 on selected batch sizes. Times reported are time per alignment over all starting positions (“per alignment”) or per starting position (“per start”).

| PAPER Mode | Molecule Size | GPU | Batch Size | Runtime (per alignment, ms) | Runtime (per start, ms) |
|---|---|---|---|---|---|
| 5 (31 starting orientations) | small | 8600GT (32 SP) | 1 | 24.38 | 0.79 |
| | | | 20 | 22.02 | 0.71 |
| | | | 100 | 22.06 | 0.71 |
| | | | 500 | 21.86 | 0.71 |
| | | 8800GTX (128 SP) | 1 | 8.84 | 0.29 |
| | | | 20 | 6.62 | 0.21 |
| | | | 100 | 6.34 | 0.20 |
| | | | 500 | 6.29 | 0.20 |
| | | GTX280 (240 SP) | 1 | 8.52 | 0.27 |
| | | | 20 | 2.63 | 0.08 |
| | | | 100 | 2.27 | 0.07 |
| | | | 500 | 2.16 | 0.07 |
| | medium | 8600GT (32 SP) | 1 | 37.93 | 1.22 |
| | | | 20 | 28.66 | 0.92 |
| | | | 100 | 28.68 | 0.93 |
| | | | 500 | 28.73 | 0.93 |
| | | 8800GTX (128 SP) | 1 | 16.11 | 0.52 |
| | | | 20 | 11.00 | 0.35 |
| | | | 100 | 10.51 | 0.34 |
| | | | 500 | 10.45 | 0.34 |
| | | GTX280 (240 SP) | 1 | 7.23 | 0.23 |
| | | | 20 | 2.05 | 0.07 |
| | | | 100 | 1.99 | 0.06 |
| | | | 500 | 1.97 | 0.06 |
| | large | 8600GT (32 SP) | 1 | 49.31 | 1.59 |
| | | | 20 | 45.10 | 1.45 |
| | | | 100 | 44.64 | 1.44 |
| | | | 500 | 44.83 | 1.45 |
| | | 8800GTX (128 SP) | 1 | 29.25 | 0.94 |
| | | | 20 | 16.77 | 0.54 |
| | | | 100 | 16.12 | 0.52 |
| | | | 500 | 16.02 | 0.52 |
| | | GTX280 (240 SP) | 1 | 29.26 | 0.94 |
| | | | 20 | 10.65 | 0.34 |
| | | | 100 | 10.22 | 0.33 |
| | | | 500 | 10.02 | 0.32 |

Table 2.10: PAPER performance for initialization mode 5 on selected batch sizes. Times reported are time per alignment over all starting positions (“per alignment”) or per starting position (“per start”).

# Chapter 3

# GPU Acceleration of SMILES-based 2D Chemical Similarity


## Abstract

LINGOs are a holographic measure of chemical similarity based on text comparison of SMILES strings. We present a new algorithm for calculating LINGO similarities amenable to parallelization on SIMD architectures (such as GPUs and vector units of modern CPUs). We show that it is nearly 3 times as fast as existing algorithms on a CPU, and over 80 times faster than existing methods when run on a GPU.


This chapter has previously appeared in reference [42].

## 3.1 Introduction

The continuing exponential increase in computer power has made searches in chemical databases of thousands to millions of compounds routine. A variety of techniques exist for similarity search [64], ranging in computational complexity from 3-D superposition methods [33, 58, 75] to simple substructure-fingerprint searches [16, 25]. The Lingo method of Vidal, Thormann, and Pons [85] is a particularly simple algorithm that measures chemical similarity by computing the similarity between the SMILES representations of two given molecules. Despite its simplicity, LINGO has demonstrated accuracy comparable to path-based substructural fingerprint methods [34]; its compelling advantages are speed and the ready availability of appropriate SMILES representations for molecules.

While LINGO is one of the fastest similarity techniques in general usage, emerging problems in cheminformatics necessitate dramatically faster methods for calculating similarities. Freely available databases such as ZINC [45] (34 million molecules) and PubChem (31 million molecules) are currently being used for a variety of cheminformatic analyses. Exhaustive calculations on multi-million molecule databases such as these present a challenge to many commonly-used algorithms. Even more difficult are exhaustive databases such as GDB-13 [8], which enumerates all 970 million molecules up to 13 heavy atoms containing C, N, O, S, and Cl, according to a set of simple rules encoding chemical stability and feasibility. Virtual combinatorial libraries can also present a challenge to conventional algorithms, as even a 3 or 4 component combinatorial library can easily exceed a billion molecules.

Scalability problems arise both from database size and the algorithms considered. The largest current enumerated databases are nearly 1 billion ($10^9$) molecules in size [8]; future libraries are likely to be larger. While search for a single query molecule can be done in linear time, useful algorithms such as clustering chemical databases often run in time quadratic in the size of the database or worse [15]. Consequently, as the size of both public and corporate compound collections increases, faster similarity methods are required to handle the increasing computational load.

The GPU revolution in computing offers a way to cope with these issues. Modern GPUs (graphics processing units) are flexibly-programmable processors which offer theoretical

speedups over 30-fold relative to top-end conventional CPUs. GPUs have been applied, with great effect, to related problems in computational chemistry, including molecular dynamics [28, 81] and 3D similarity search [39]. Although GPUs often require algorithms to be redesigned to achieve peak speedup, such changes also often benefit modern CPUs.

In this paper we present SIML ("Single-Instruction, Multiple-LINGO"), a new algorithm (related to sparse matrix-matrix multiply) to calculate the LINGO similarity metric between molecules, especially suited for efficient execution on GPUs and the vector units of current CPUs. We describe a non-vectorized CPU version of our algorithm that is nearly 3 times as fast as existing algorithms for calculating LINGOs and a GPU implementation that is over 80 times as fast as existing methods. Our code is available at `https://simtk.org/home/siml`. We begin by explaining the LINGO similarity metric, continue with a description of our algorithm, present performance benchmarks, and conclude with a discussion of extensions of our work to generalizations of the considered LINGO similarities.

## 3.2 Methods

### 3.2.1 Overview of LINGO

The LINGO algorithm [85] models a molecule as a collection of substrings of a canonical SMILES representation. Specifically, a SMILES string (after some simple transformations, such as resetting all ring closure digits to zero) is fragmented into all its contiguous substrings of length $q$, producing the set of "q-Lingos" for that molecule. The similarity between a pair of molecules A and B is then defined by the following equation:

$$T_{A,B} = \frac{1}{\ell} \sum_{i=1}^{\ell} \left( 1 - \frac{|N_{A,i} - N_{B,i}|}{N_{A,i} + N_{B,i}} \right) \tag{3.1}$$

In this equation, $\ell$ represents the number of Lingos present in either A or B, and $N_{x,i}$ represents the number of Lingos of type $i$ present in molecule $x$. In this paper, we will use the lowercase "Lingo" to refer to a substring of a SMILES string and the all-capitals "LINGO" to refer either to the method, or the Tanimoto similarity resulting from the method.

Grant et al. have presented an efficient algorithm to calculate this Tanimoto value given

a pair of SMILES strings [34]. Their algorithm, given two SMILES strings of lengths $m$ and $n$, first constructs in $\Theta(m)$ time a finite state machine representation of one SMILES string and all its valid Lingos. It then processes the second string through this FSM in $\Theta(n)$ time, yielding a total runtime linear in the sum of the length of the two strings.

The use of the LINGO algorithm requires choosing a particular value of $q$, the SMILES substring length. Values of $q$ that are too small retain little structural information about molecules; values that are too large induce too many distinct Lingos, making it increasingly unlikely that a pair of molecules will have Lingos in common. Both Vidal et al. [85] and Grant et al. [34] demonstrated that setting $q = 4$ (i.e., considering SMILES substrings of length 4) had the best performance in a variety of cheminformatics applications.

### 3.2.2 Our Algorithm

The LINGO Tanimoto equation can be written in a simpler form using set notation. Specifically, we treat a molecule as a multiset of q-Lingos; a multiset is a generalization of a set that allows each element of a set to have multiplicity greater than 1. The union of two multisets contains all elements present in either set, with multiplicity equal to the maximum multiplicity of that element in either set. Similarly, the intersection of two multisets has only those elements present in both sets, with multiplicity equal to the minimum multiplicity in either set. In this model, the LINGO Tanimoto between a pair of molecules takes the following simple form:

$$T_{A,B} = \frac{|A \cap B|}{|A \cup B|} \tag{3.2}$$

Computer systems typically represent a character with 8 bits; thus, there is a one-to-one correspondence between q-Lingos and $8q$-bit integers. The optimality of $q = 4$ is fortuitous, as 4-Lingos correspond to 32-bit integers, which map directly to the typical word length of modern CPUs and GPUs (but see the conclusion for discussion of efficient implementations where $q \neq 4$). This mapping means that current hardware can perform a comparison between two 4-Lingos in one operation, rather than the 4 that would be needed for individual characters. We thus represent each molecule as a multiset of 32-bit integers: a sorted vector of 4-Lingos (represented as integers), and a parallel vector containing the multiplicity of

each Lingo.

This multiset intersection/union can also be interpreted as a modified vector Tanimoto operating on sparse vectors $A$ and $B$. In this interpretation, $A$ and $B$ are extremely-high dimensional vectors, in which each coordinate specifies the number of Lingos present in the molecule of a given type; the dimensionality is determined by the number of possible Lingos. If each Lingo consists of four 8-bit characters, then the implicit dimensionality is $2^{32}$; however, since most of these Lingos will not be present, the vector is highly sparse. Consider the vector Tanimoto equation:

$$T_{AB} = \frac{\langle A, B \rangle}{\langle A, A \rangle + \langle B, B \rangle - \langle A, B \rangle} \tag{3.3}$$

If addition is kept as normal and multiplication of two numbers is replaced by taking the minimum of the two it is trivial to prove that this modified vector Tanimoto calculates the exact same quantity as the multiset definition given above (indeed, an equivalent expression, motivated differently, is given by Grant et al. [34]). This interpretation (which uses the same representation in memory as the multiset interpretation) has the advantage that the set magnitudes $\langle A, A \rangle$ and $\langle B, B \rangle$ need not be calculated for every Tanimoto calculation; only the intersection size $\langle A, B \rangle$ must be calculated each time. Indeed, the set magnitudes are determined by the SMILES length $\ell$ and Lingo size $q$: $\langle x, x \rangle = \ell_x - q + 1$. This sparse vector algorithm therefore saves the computation involved in calculating the set union in the multiset algorithm.

Given a pair of molecules represented in the paired-array manner listed above, the LINGO Tanimoto between them can be calculated in linear time using an algorithm similar to merging sorted lists (Algorithm 1).

### 3.2.3 GPU implementation

The finite-state-machine algorithm of Grant et al. [34] is poorly adapted to execution on a GPU or other SIMD processor because it requires either a large amount of branching or a moderately-sized lookup table to implement FSM state transitions. While it is possible to write branch-dense code for a GPU, such code typically performs poorly because different

**Data**: sorted lists a and b containing Lingos, sorted lists $a_c$ and $b_c$ containing Lingo counts, scalars $\ell_a$ and $\ell_b$ the lengths of lists a and b, and scalars $m_a = \sum a_c$ and $m_b = \sum b_c$.
**Result**: LINGO Tanimoto between molecules a and b
`Indices into lists` $a/a_c$ `and` $b/b_c$
i = j = 0;
`Accumulator for magnitude of intersection between a and b`
isct = 0;
**while** $i < \ell_a$ *and* $j < \ell_b$ **do**
  **if** *a[i] == b[j]* **then**
    isct += min($a_c[i]$,$b_c[j]$) ;
    i += 1;
    j += 1;
  **else if** $a[i] < b[j]$ **then**
    i += 1;
  **else**
    j += 1;
  **end**
**end**
**return** $(isct/\left(m_a + m_b - isct\right))$

**Algorithm 1**: Sparse-vector algorithm to calculate LINGO Tanimoto between two molecules in sorted multiset representation

lanes in the vector unit must execute different code paths. The latter option, a large random-access lookup table, falls prey to memory constraints. The GPU has only a very small amount of low-latency "shared" memory with true random access on-chip (16KB on recent NVIDIA GPUs). If the lookup table is larger than the available shared memory, then it must be placed in off-chip "global" memory; however, good performance on GPUs requires that global memory be accessed with spatial locality among threads. This behavior is unlikely for a state-transition lookup table.

In contrast, our algorithm is well-suited for GPU implementation. In calculating a similarity matrix, we assign each row of the matrix to a "thread block", or virtual core, on the GPU. Each thread block executes many threads, which calculate elements of the row in parallel. Each thread block stores the multiset representation of its query molecule (the molecule against which all column elements are compared) in shared memory to minimize global memory accesses. Furthermore, we store database molecules (ones along the columns of the similarity matrix) in column-major layout (such that the Lingos/counts for each molecule lie in one column). This layout maximizes the spatial locality of memory accesses by consecutive threads.

In architectures that require loads by adjacent lanes of a vector unit to be adjacent in memory for high performance (e.g., Intel/AMD SSE, GPUs without texture caching), it is possible to make a small modification to our algorithm to guarantee this characteristic. We let $j$, the database molecule multiset index, be shared among all threads. We ensure that each thread has advanced its $i$ pointer (query multiset index) as far as possible before $j$ is incremented, so all threads always read from the same row in the transposed database multiset matrix. In architectures with relaxed locality requirements (e.g., GPUs with 2-D texture caching support), this row-synchronization can be removed, allowing higher performance.

## 3.3 Results

### 3.3.1 Benchmarking Methodology

Our benchmark problem is the calculation of an all-vs-all LINGO Tanimoto matrix for a set of compounds, which is a common first step for many algorithms in cheminformatics, such as clustering. It is also relevant to doing multiple similarity searches, as the calculation of each row of the matrix is equivalent to performing a database search against a different query molecule.

For this particular problem it would be possible to halve the calculation by only evaluating the upper or lower triangle of the Tanimoto matrix, since using the same molecule set for both query and database compounds induces a symmetric matrix. However, in the general case different molecule sets may be used for the query and database sets (along the rows and columns of the resulting matrix), resulting in an asymmetric matrix. We therefore benchmarked the computation of the full Tanimoto matrix, rather than only the upper or lower half, for greater generality. We benchmark the following Tanimoto calculation methods:

- OE: OpenEye implementation (OELingoSim) of the LINGO similarity method
- CPU: CPU implementation of our sparse vector algorithm using precalculated magnitudes and normal (row-major) database layout
- GPU: GPU implementation of our sparse vector algorithm using precalculated magnitudes, transposed (column-major) query layout, and 2-D texture fetching

All CPU performance testing was performed at Vertex on machine 1. GPU performance testing was performed on two different machines at Stanford to assess code scaling:

- Machine 1: CPU: AMD Phenom II X4 920 (4 cores @ 2.8GHz)
- Machine 2: CPU: Intel Core 2 Quad Q6600 (4 cores @ 2.4GHz); GPU: NVIDIA GeForce GTS 250 (128 SP @ 1.84 GHz)
- Machine 3: CPU: Intel Xeon E5420 (4 cores @ 2.5GHz); GPU: NVIDIA Tesla T10 (240 SP @ 1.44 GHz)

| # molecules | **Average SMILES length** (characters) | **Average # distinct Lingos** |
|---|---|---|
| 4,096 | 35.17 | 29.31 |
| 8,192 | 35.41 | 29.52 |
| 32,768 | 38.23 | 31.65 |

Table 3.1: Characteristics of SMILES sets from Maybridge used for benchmarking

The performance of our CPU code and the OpenEye LINGO implementation were measured using a test code written in C++. We used OpenMP (a multi-platform standard API for shared memory parallel programming) to parallelize both CPU methods to obtain multi-core results. Our GPU implementation is written in Python, using the PyCUDA library to access the GPU. Tanimoto calculations for both GPU and CPU codes were implemented as requesting 240 rows of a Tanimoto matrix at a time to enable parallelization over rows. All timing results were averaged over 6 runs.

Machines 1 and 2 used gcc 4.3.2; machine 3 used gcc 4.1.2. CPU code was compiled with `gcc -O2 -fopenmp`. CUDA version 2.3 and NVIDIA driver version 190.29 were used on both machines 2 and 3.

All SMILES strings used for testing were obtained from the ZINC database's subset of molecules from Maybridge [45]. Relevant statistics for the chosen benchmark sets are shown in 3.1.

### 3.3.2 Performance

As a baseline performance benchmark, we evaluated the performance of the OpenEye algorithm and our CPU multiset/sparse-vector algorithm on the construction of a similarity matrix for a 4,096 molecule subset of the Maybridge database. The performance results on Machine 1 are shown in 3.2. To evaluate GPU performance, we measured the time to construct a similarity matrix on sets of 4,096, 8,192, and 32,768 molecules from Maybridge, on machines 2 and 3. Measured times include the time to transfer sparse-vector-representation molecules to the GPU as well as the time to transfer calculated Tanimotos back to the host. GPU results are presented in 3.3.

| **Algorithm** | **Time** (ms) | **Throughput** (kLINGOS/sec) |
|---|---|---|
| OE | 15060 | 1113 |
| CPU | 5460 | 3070 |
| OE parallel | 3880 | 4320 |
| CPU parallel | 1420 | 11830 |
| Read SMILES + construct multisets | 10.5 | — |

Table 3.2: Similarity matrix construction performance on CPU, 4,096 molecules, Machine 1 (parallel = 4 cores)

| **Machine** | **Number of molecules** | **Time** (ms) | **Throughput** (kLINGOS/sec) |
|---|---|---|---|
| 2 | 4096 | 275 | 60900 |
| 2 | 8192 | 1026 | 65410 |
| 2 | 32768 | 16717 | 64230 |
| 3 | 4096 | 215 | 77900 |
| 3 | 8192 | 778 | 86300 |
| 3 | 32768 | 11637 | 92270 |

Table 3.3: Similarity matrix construction performance on GPU. Times include transfer of molecules to GPU and transfer of Tanimotos back to host. Note that total work performed is quadratic in the number of molecules.

## 3.4 Analysis

Our multiset/sparse-vector methods for calculating LINGO Tanimotos show significant speedup relative to the existing best-in-class techniques for calculating LINGOs. The CPU implementation shows a 2.75x speedup relative to the OpenEye method. This algorithm incurs additional initialization overhead for each query string at the start of each row, whereas in our method the preprocessing (constructing sorted-array multiset representations of the SMILES strings) is performed at startup and not repeated. However, this startup cost is amortized over the large calculation, amounting to less than 1% of the execution time even for the parallel implementation of the CPU-based algorithm (last row, 3.2), and does not significantly affect the achieved speedups. It is notable as well that our CPU implementation is not vectorized to take advantage of the SSE capabilities on the tested Phenom II CPU. As explained above, our algorithm is amenable to vectorization, and it may be possible to obtain even larger speedups on the CPU.

Even larger speedups are achieved by moving the algorithm onto a GPU. On the 4K-size problem, machine 2's midrange GPU shows nearly 20x speedup relative to our CPU sparse-vector algorithm, and nearly 55x relative to the OE algorithm. The throughput for this midrange GPU falls off somewhat as the matrix size increases; this is likely due to the increasing average size (29.3 Lingos at 4K to 31.6 Lingos at 32K) increasing the work per Tanimoto calculation. In contrast, the throughput on the high-end GPU (machine 3) continues to rise as the matrix size increases, indicating that even higher throughput may be possible on larger problems. At the largest size we tested, the high-end Tesla T10 GPU shows 30x speedup relative to our CPU method and nearly 83x speedup relative to the OE technique.

Because they take advantage of the inherent parallelism in large-scale similarity calculations by parallelizing over row computations, our methods also scale very well to larger hardware. Our CPU algorithm reaches 96.3% of linear speedup when parallelized over 4 cores with OpenMP. Our GPU code also shows excellent scaling; at the largest problem size, we observe 97.9% of the expected throughput scaling, based on the increased number of shaders and decreased clock speed on the Tesla T10 relative to the GeForce GTS 250.

While our algorithm is well suited to very-large-scale similarity calculations involving

the calculation of multiple rows of a Tanimoto matrix, it is not a good choice for small calculations such as the scan of a single molecule against a SMILES database. Our algorithm has a setup cost linear in the total number of molecules considered (query+database), whereas the Grant et al. FSM-based algorithm only incurs cost for each query molecule. In the 1xN (one query versus database of size N) case, the FSM algorithm thus has O(1) initialization cost, whereas our sparse vector algorithm has O(N) initialization cost. For large (multiple-row) calculations this setup cost is amortized because the same sparse-vector representations of database molecules are reused at each row.

## 3.5 Conclusions

The growing size of chemical databases requires the development of faster methods of chemical similarity comparison in order to implement database search, clustering, and other cheminformatic algorithms. We have described a new algorithm for calculating the LINGO similarity measure which is nearly 3x faster than the current best-in-class method. This algorithm is well-suited to implementation on SIMD architectures like GPUs, and demonstrates over 80-fold speedup versus OpenEye's implementation of LINGO similarities when run on a high-end GPU. Furthermore, this algorithm scales well to large hardware, enabling high performance on new generations of CPU and GPU hardware. Implementations of our algorithm are available at `https://simtk.org/home/siml`.

Our current implementations are focused on the LINGO algorithm with $q = 4$ (that is, considering SMILES substrings of length 4) because they have been shown to be optimal for typical similarity searches [34, 85]. However, in some cases, a different value of $q$ may be desirable (for example, extremely small molecules, in which there are few distinct Lingos, or cases in which more specificity, and a larger Lingo size, is required). Our algorithm is trivially extensible to $q < 4$; such Lingos correspond one-to-one with integers smaller than 32 bits, so the remaining available bits can be replaced by zero and the algorithm remains as previously described. It is also possible to extend the method to larger $q$. One possibility is to extend the integer size — by using 64-bit integers, up to $q = 8$ can be handled using the same method. Recent CPUs and upcoming GPUs natively support 64-bit integers, potentially imposing little overhead (except doubled memory traffic) relative to the

use of 32-bit integers. Another option is to compress the Lingos. SMILES does not have a full 256-character alphabet, and therefore does not require a full 8 bits per character. By preprocessing strings the width of each character in a Lingo can be reduced. For example, if only 64 characters are used in a set of molecules, each character will only require 6 bits, and up to $q = 5$ can be supported still using 32-bit integers. Our algorithm is insensitive to these issues, as it operates on integers of arbitrary width. While certain integer sizes may be faster on given hardware, methods such as Lingo compression can be handled in preprocessing, and do not affect the core multiset algorithm.

By providing nearly 2 orders of magnitude in speedup, our algorithm enables dramatically larger calculations than previously possible. The use of GPU acceleration in particular allows searches that previously required use of a cluster of hundreds of machines to be performed on a user's desktop; alternatively, lengthy searches can be performed in near-realtime. We anticipate that these search capabilities will enable a new class of large-scale cheminformatics applications for data fusion on very large databases.

## Acknowledgments

The authors would like to thank Kim Branson for assistance with running CPU benchmarking and Anthony Nicholls and Roger Sayle for helpful comments on the manuscript. ISH and VSP acknowledge support from Simbios (NIH Roadmap GM072970).

# Chapter 4

# Optimization of GPU Chemical Similarity

## Abstract

In this chapter we present the design and optimization of GPU implementations of two popular chemical similarity techniques: Gaussian shape overlay (GSO) and LINGO. GSO involves a data-parallel, arithmetically-intensive iterative numerical optimization; we use it to examine issues of thread-parallelism, arithmetic optimization, and CPU-GPU transfer overhead minimization. LINGO is a string similarity algorithm that, in its canonical CPU implementation, is memory bandwidth- and branch-intensive and has limited data parallelism. We present an algorithmic redesign allowing GPU implementation of such a low arithmetic-intensity kernel, and discuss techniques for memory optimization that enable large speedup. Source code for the programs described here is available online: PAPER (for Gaussian shape overlay) can be downloaded at `https://simtk.org/home/paper` under the GPL, and SIML (for LINGO) at `https://simtk.org/home/siml` under a BSD license.

This chapter has previously appeared in reference [41].

## 4.1 Introduction, Problem Statement, and Context

Chemical informatics uses computational methods to analyze chemical datasets for applications that include search and classification of known chemicals, virtually screening digital libraries of chemicals to find ones which may be active as potential drugs, and predicting and optimizing the properties of existing active compounds. A common computational kernel in cheminformatics is the evaluation of a similarity (using various models of similarity) between a pair of chemicals. Such similarity algorithms are important tools in both academia and industry.

A significant trend in chemical informatics is the increasing size of chemical databases. Public databases listing known chemical matter exceed 30 million molecules in size, the largest exhaustive libraries (listing all possible compounds under certain constraints) are near 1 billion molecules, and virtual combinatorial libraries in use in industry can easily reach the trillions of compounds. Unfortunately, similarity evaluations are often slow, at or below 1000 evaluations/sec on a CPU. Adding to the problem, typical analyses in this field (such as clustering) must execute a number of similarity evaluations that is supralinear in the size of the database. The combination of rapidly growing chemical data sets and computationally-expensive algorithms creates a need for new techniques.

The massive data and task parallelism present in large-scale chemical problems makes GPU reimplementation an attractive acceleration method. In this article, we demonstrate 10-100$\times$ speedup in large-scale chemical similarity calculations, which allows the analysis of dramatically larger datasets than previously possible. Search problems which formerly would have required use of a cluster can now be efficiently performed on a single machine; alternatively, formerly supercomputer-scale problems can be run on a small number of GPUs. In particular, we show that two commonly used algorithms can be effectively parallelized on the GPU: Gaussian shape overlay (GSO) [39], a 3-dimensional shape comparison technique, and LINGO [42], a string comparison method.

### 4.1.1 Gaussian shape overlay: background

Gaussian shape overlay is an algorithm that measures the similarity of two molecules by calculating the similarity of their shapes in 3-dimensional space. In this method, a molecule

is represented as a scalar field or function in 3-space, where the value of the function at each point in space indicates whether or not the point is "inside" the molecule. Given a set of functions $\rho_{Ai}(\mathbf{r})$ that represent the density functions for each atom of a molecule (i.e., functions that are 1 inside the volume of an atom and 0 outside), the function for an entire molecule can be defined using one of the formulas in equation 4.1. The first computes interior points by taking the product of the complement of all atoms — defining an "exterior point" as one which is not inside any atom. The latter method uses the principle of inclusion-exclusion between sets to compute the same union of all atoms.

$$\begin{aligned} \rho_A(\mathbf{r}) &\equiv 1 - \prod_{i=1}^{N} (1 - \rho_{Ai}(\mathbf{r})) \\ \rho_A(\mathbf{r}) &\equiv \sum_i \rho_{Ai} - \sum_{i<j} \rho_{Ai}\rho_{Aj} + \sum_{i<j<k} \rho_{Ai}\rho_{Aj}\rho_{Ak} - \sum_{i<j<k<l} \rho_{Ai}\rho_{Aj}\rho_{Ak}\rho_{Al} + \cdots \end{aligned} \tag{4.1}$$

Equation 4.1 is motivated by considering each atom to be a set of points, and constructing the union of these sets. Defining atomic densities as indicator functions (one inside a given radius around a point and zero outside) generates the "hard-sphere" model of molecular shape. This model has several shortcomings (including nondifferentiability) that makes it difficult to use in computations. Consequently, Grant and Pickup developed the Gaussian model of molecular shape, in which each atom's density function is defined not as a hard sphere, but as an isotropic spherical Gaussian function:

$$\rho_{Ak}(\mathbf{r}) = p_k \exp\left(-\alpha_k ||\mathbf{r}_k - \mathbf{r}||^2\right) \tag{4.2}$$

Such Gaussian functions are smooth and differentiable. Furthermore, simple closed-form expressions for the volumes, volume gradients (with respect to position), and Hessians of the product of an arbitrary number of such Gaussians are known [35]. This enables the calculation of the similarity of two molecules by calculating the maximum overlap possible between their shapes, maximized over all rigid-body transformations (translations and rotations). Mathematically, GSO seeks to maximize equation 4.3 over all rigid body transformations. In this integral, the functions $\rho_A$ and $\rho_B$ are the density fields for each molecule and the integral is taken over all space.

$$\int d\mathbf{r}\rho_A\rho_B \tag{4.3}$$

The computation is performed by numerical optimization to orient a pair of molecules in their optimally-overlapping poses, and then computing the overlap volume (Figure 4.1) [33]. The objective function in such a calculation is typically a truncated form of Equation 4.1, including only the single-overlap terms (Equation 4.4). Thus, both the objective and gradient calculations are arithmetically-intensive and data-parallel, involving a double-loop over the atoms of each molecule and an exponential evaluation inside the loop body. These aspects make GPUs an attractive platform to implement GSO. In the first half of this chapter, we describe PAPER, our open-source implementation of GSO on NVIDIA GPUs [39].

$$\int d\mathbf{r}\rho_A\rho_B \approx \int d\mathbf{r} \left( \sum_{i,j} \rho_{Ai}\rho_{Bj} \right) \tag{4.4}$$

### 4.1.2 LINGO: background

Whereas GSO represents a molecule by its three-dimensional shape in space, the LINGO algorithm of Vidal, Thormann, and Pons takes a much simpler, text-based approach [85]. LINGO is a 2-D similarity method: one that operates on molecules as graphs (with vertices representing atoms and edges representing atomic bonds), ignoring their 3-dimensional shape. Instead of operating directly on this molecular graph, LINGO processes a linear representation of the graph called a SMILES string, which is constructed by a depth-first traversal of the graph. The characters in the SMILES string represent various graph features, such as atom types, bond orders, ring openings and closings, and branching. Given a SMILES string, LINGO represents a molecule as the set of all overlapping $q$-character substrings in the SMILES (known as "Lingos", as opposed to "LINGO" for the algorithm as a whole). $q$ is typically set to 4 (i.e., Lingos have length 4), as this has been demonstrated to have superior performance in several applications. Figure 4.2 presents an example of a molecule and its SMILES representation, and its LINGO substrings for $q = 4$.

The similarities between a pair of molecules A and B is defined by the following equation,

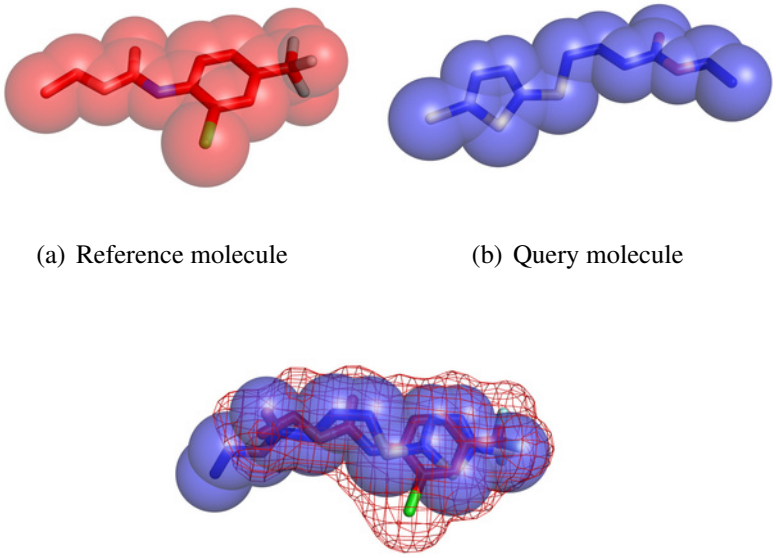

(a) Reference molecule (b) Query molecule

(c) Calculated overlay

Figure 4.1: 3D shape overlay of molecules. The reference and query molecules are depicted as sticks (to visualize bond structure) embedded within their space-filling representation. GSO rotates the query molecule to maximize its volume overlap (blue spheres) with the volume of the reference (red mesh).

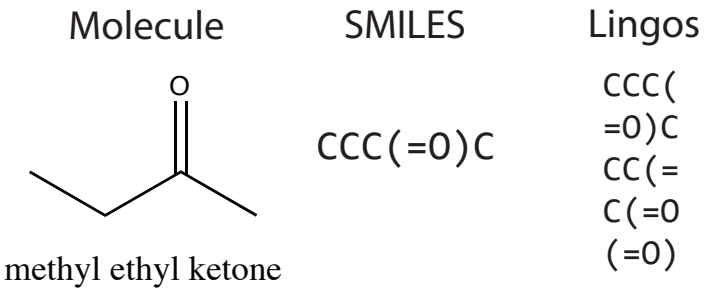


Figure 4.2: Chemical graph structure of a common solvent, its SMILES representation, and its constituent Lingos.

where $N_{x,i}$ represents the number of Lingos of type $i$ in molecule $x$:

$$T_{A,B} = \frac{1}{\ell} \sum_{i=1}^{\ell} \left( 1 - \frac{|N_{A,i} - N_{B,i}|}{N_{A,i} + N_{B,i}} \right) \tag{4.5}$$

The canonical high-performance CPU implementation to rapidly evaluate this similarity on a CPU was presented by Grant et al. [34]. This algorithm is optimized for the case in which many SMILES strings must all be compared against one query. The Lingos of the query string are inserted into a trie, a tree data structure allowing fast prefix search of strings. This trie is then converted into a deterministic finite state automaton [3]; successive database strings can then be efficiently processed through this DFA. This algorithm suffers from a large amount of branching and poor memory locality in the simulation of the DFA, and generally has poor data-parallelism within each LINGO calculation. It is thus relatively unattractive for GPU implementation. In the latter half of this chapter, we discuss the algorithmic transformations and memory optimizations that enable the high-speed GPU implementation in SIML, our open-source package to calculate LINGO similarities on GPUs [42].

## 4.2 Core Methods

Large-scale chemical informatics calculations involve the calculation of many similarities at the same time, and so have a large amount of task parallelism; we exploit this structure in both problems by calculating a large number of similarities at a time. The GSO problem in particular is arithmetic-bound: its inner loop involves the calculation of $O(MN)$ exponential functions (where $M$ and $N$ are the number of atoms in the molecules being compared), and must be executed many times in a numerical optimization scheme (Equation 4.4). We make use of SIMD data parallelism and hardware evaluation of exponentials to maximize the arithmetic throughput of GSO on the GPU. LINGO, as implemented for high performance on the CPU, uses a deterministic finite-state automaton algorithm that exhibits large branch penalties and poor memory access locality on the GPU. We describe an algorithmic redesign for LINGO that minimizes branch divergence and makes special use of GPU hardware (texture caching) to maximize memory throughput.

## 4.3 Gaussian Shape Overlay: Parallelization and Arithmetic Optimization

The GSO calculation is a numerical maximization of equation 4.4 over a seven-dimensional space (3 translational coordinates and a 4-dimensional quaternion parameterization of a rotation). In this section, we describe the design and optimization of PAPER, our GPU implementation of GSO [39].

PAPER uses the BFGS algorithm [70], a "pseudo-second-order" method that uses evaluations of the objective function and its first derivative (gradient), but no second-derivative evaluations. Because BFGS is a local optimizer, and GSO is a global optimization problem, we start each optimization from several initial points. The key computational steps in this calculation are:

1. Repeatedly evaluate objective at test points along a search direction to find a "sufficiently" improved point (line search)

2. Evaluate gradient at new point from line search

3. Update BFGS approximation to inverse Hessian matrix, and use this to calculate new search direction

The primary consideration in software architecture for the GPU is partition of work: what work should be done on the CPU vs the GPU, how work should be partitioned among independent GPU cores (CUDA thread blocks or OpenCL work-groups), and how work can be partitioned among threads or vector lanes in each core. PAPER makes use of the extensive task-parallelism in chemical informatics to allocate work to GPU cores. Our target applications focus on searches with hundreds to thousands of comparisons to be performed. Because for each calculation we optimize from several (typically 4) starting points, GSO yields a large number (# starting points $\times$ # molecules) of independent problems, each of which can be assigned to an independent core (CUDA thread block or OpenCL work-group ). Partitioning work among GPU threads and between the CPU and GPU is more involved, and is the focus of this section.

### 4.3.1 Evaluation of data-parallel objective function

Equation 4.4 describes the objective function that must be implemented in GSO. It is inherently data-parallel, containing a double-loop over the $M$ atoms of the reference molecule and $N$ atoms of the query molecule with an arithmetically-intensive loop body. This section describes the parallelization of the objective calculation (which has the same structure as the gradient), and presents several versions illustrating consecutive optimizations.

PAPER uses blocks of 64 threads to maximize the number of registers available to each thread. While it can be advantageous in some cases to use larger thread blocks to hide memory latency, in our application we typically have multiple thread blocks available on each multiprocessor. Since scheduling is done on a per-warp basis, using many, smaller, thread blocks is sufficient. In typical use cases, the number of terms to be calculated in the objective is larger than the number of available threads: typical molecules are 20-40 atoms, so that normal calculations will have 400-1600 terms. To parallelize the problem, we assign threads to calculate thread-block size "strips" of the interaction matrix consecutively, until the entire set of interactions has been evaluated. Instead of using atomic operations to accumulate the volume among threads, the function keeps an array in shared memory and does a parallel reduction at the end to sum the final overlap volume. Figure 4.3 illustrates the order of the computation, and Listing 4.1 provides code for a simple version of the objective evaluation.

We perform an addressing calculation (lines 12-13) at each loop iteration so that each thread evaluates the correct matrix element. Another strategy would be to disallow thread blocks to span rows of the interaction matrix; however, this has the potential to leave many threads idle, as there are usually more threads than the width of the matrix. Another option would be the use of a two-dimensional thread block. However, because the number of atoms varies by molecule in a batch, and because the number of atoms is not likely to be a multiple of the GPU warp size, this also is likely to leave the GPU partially idle. Using the given loop structure ensures that all threads do useful work as long as there are terms left to compute.

While the objective function in Listing 4.1 is effectively parallelized across all GPU threads, several changes can be made to improve its performance. The first point of concern is the addressing calculation. Because the number of atoms in either molecule is unlikely

```
1 /* Data: molecules ref and query
2  *       .natoms contains number of atoms in molecule
3  *       .xyz[i] contains coordinates for atom i
4  *       .a[i] is a scalar computed from the van der Waals radius of
       atom i
5  */
6 float overlap(molecule ref, molecule query) {
7   __shared__ float temp[]; // Has size equal to blockDim.x
8   temp[threadIdx.x] = 0;
9   for (int base = 0; base < ref.natoms * query.natoms;
10        base += blockDim.x) {
11     int mycord = base + threadIdx.x;
12     if (mycord < ref.natoms*query.natoms) {
13       int ref_idx   = mycord / query.natoms;
14       int query_idx = mycord - ref_idx*query.natoms;
15
16       float Rij2  = distance_squared(ref.xyz[ref_idx],
17                                      query.xyz[query_idx]);
18       float ref_a = ref.a[ref_idx], query_a = query.a[query_idx];
19
20       float Kij = expf(-ref_a*query_a*Rij2/(ref_a+query_a));
21       float Vij = Kij * 8 * powf(PI/(ref_a+query_a),1.5f);
22       temp[threadIdx.x] += Vij;
23     }
24   }
25   for (int stride = blockDim.x/2; stride > 0; stride >>=1) {
26     __syncthreads();
27     if (threadIdx.x < stride)
28       temp[threadIdx.x] += temp[threadIdx.x+stride];
29   }
30   __syncthreads();
31   return temp[0];
32 }
```

Listing 4.1: First version of GSO objective function

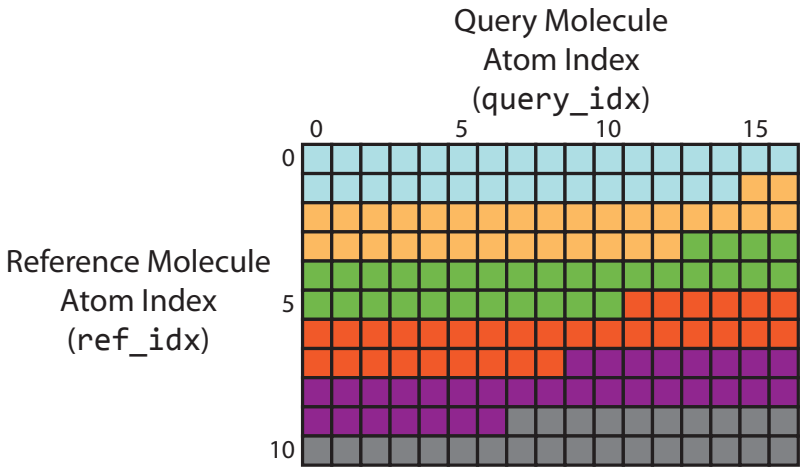


Figure 4.3: Thread parallelization scheme in PAPER. Depicted is the full matrix of interactions between a reference molecule of 11 atoms and a query molecule of 17 atoms. Thread blocks of 32 threads process consecutive 32-element strips of the matrix. Each color represents one iteration of a thread block. Note that no more than a thread block-sized strip of matrix elements must be materialized at any time during the computation.

to be a power of two, it is necessary to use a division to calculate the row index for each thread. However, integer division is a very expensive operation on current GPUs; when performed in the inner loop, as in the original objective, it adds significant overhead. It is possible to restructure the addressing such that the division is only performed once (Listing 4.2; non-addressing computations have been elided). Restructuring the calculation in this way reduces the in-loop addressing overhead to two adds, a comparison, and two conditional adds, which are much cheaper than the integer division. In the full PAPER implementation, the objective is called multiple times per kernel invocation in the course of a line search; thus, `row_per_block` and `col_per_block` are precalculated at the start of the kernel invocation and stored in shared memory to amortize the cost of the division. Implementing this change to the objective and gradient functions leads to a measured 13% speedup in total optimization time.

With the integer division removed, the runtime becomes dominated by the evaluation of `Kij` and `Vij` at lines 18-19 in Listing 4.1, which involves two divides and two transcendental function evaluations — relatively expensive operations. The simplest optimization to apply here is the use of CUDA intrinsic functions for the division and transcendentals.

```
1 float overlap(molecule ref, molecule query) {
2   const int row_per_block = blockDim.x / query.natoms;
3   const int col_per_block = blockDim.x - query.natoms*row_per_block;
4   const int startrow = threadIdx.x / query.natoms;
5   const int startcol = threadIdx.x - startrow * query.natoms;
6   int ref_idx = startrow, query_idx = startcol;
7   /* Shared memory setup goes here */
8   while (ref_idx < ref.natoms) {
9     /* Floating-point core computation goes here */
10
11    ref_idx   += row_per_block;
12    query_idx += col_per_block;
13    if (query_idx >= query.natoms) {
14      query_idx -= query.natoms;
15      ref_idx++;
16    }
17  }
18  /* Parallel reduction and return go here */
19 }
```

Listing 4.2: Abbreviated GSO objective function with fast addressing

```
1 float exp_arg = __fdividef((-ref_a * query_a * Rij2),
2                            (ref_a + query_a));
3 float Kij     = __expf(exp_arg);
4 float pow_arg = __fdividef(PI,(ref_a + query_a));
5 float Vij     = Kij * 8 * __powf(pow_arg,1.5f);
```

Listing 4.3: GSO core computation with CUDA intrinsics

CUDA intrinsics are low-level hardware operations that are often much faster than their library versions, but at the cost of accuracy. In the GSO calculation, experimentation showed that the reduced accuracy of intrinsic functions is not a problem. Listing 4.3 shows the use of the `__expf`, `__powf`, and `__fdividef` intrinsics to speed up the slow operations in the objective core. Adding these three intrinsics more than doubles GSO performance with respect to the previous version (Listing 4.2).

However, careful attention to instruction performance shows that this instruction stream can be further improved. In particular, `__powf` is expensive to evaluate, and it can be replaced in this case by cheaper CUDA intrinsics: reciprocal and reciprocal square root. As is often the case, this optimization produces results that are not numerically identical

```
1 const float PIRTPI = 5.56832799683f; // pi^1.5
2 float sum = ref_a + query_a;
3 float inv = 1.0f/sum;     // CUDA intrinsic reciprocal
4 float rsq = rsqrtf(sum); // CUDA intrinsic reciprocal square root
5 float Kij = __expf(-ref_a * query_a * Rij2 * inv);
6 float Vij = 8 * PIRTPI * rsq * inv * Kij;
```

Listing 4.4: GSO core computation with restructured CUDA intrinsics

| Version | Runtime per molecule ($\mu$s) | Speedup vs original |
|---|---|---|
| Original | 201 | — |
| No-divide addressing | 175 | 1.15× |
| Intrinsic FP divide/transcendentals | 84.9 | 2.37× |
| Restructured intrinsics | 77.5 | 2.59× |

Table 4.1: Effects of objective/gradient loop tuning on PAPER performance. Measured on GTX 480 with "large" molecule set at 2000 molecules/batch.

to the original; however, regression tested showed that the accuracy is sufficient for GSO. The final computational core is provided as Listing 4.4 and is 10% faster than Listing 4.3. Table 4.1 illustrates the performance gains from various tuning strategies on the overlap and gradient kernels, as measured by their effect on the overall program runtime (not just the overlap or gradient evaluation).

### 4.3.2 Kernel fusion and CPU/GPU balancing

It is common in multistage calculations such as GSO to have one or more steps which are not efficiently parallelized on the GPU. In the case of GSO, while the line search/objective evaluation and the gradient evaluation are very efficiently executed on the GPU (because of high data parallelism and arithmetic intensity), the BFGS direction update is not well parallelized. In PAPER, the BFGS update requires a large number of sequential low-dimensional (7-D) vector operations and small (7x7) matrix operations. These operations create a large amount of thread synchronization and many idle threads; it is thus not attractive to compute them on the GPU. However, moving them to the CPU also imposes a cost. In the case of the BFGS update, the coordinates, gradients, and objective values must be retrieved

| Kernel | Original runtime ($\mu$s) | Fused runtime ($\mu$s) |
|---|---|---|
| Line search | 17000 | 17000 |
| Gradient update | 4700 | 5400 |
| GPU-CPU data transfer | 2660 | 10 |

Table 4.2: Effects of kernel fusion on PAPER performance. Measured on GTX 480 with "large" molecule set at 2000 molecules/batch.

from the GPU to do the update, and the new direction uploaded to the GPU after the CPU has calculated the update.

Using the CUDA Visual Profiler, it is possible to easily measure the overhead of the two strategies. Table 4.2 shows the timings for various execution stages of PAPER on a 2000-molecule test set. Measurements examine two versions of PAPER: one in which the gradient kernel only calculates the gradient, with BFGS updates on the host, and one with a "fused" gradient kernel, which both calculates the gradient and does the (poorly-parallelized) BFGS update on the GPU. In both versions, a small amount of data is copied from the GPU to the CPU on each iteration, to check for convergence.

The results in Table 4.2 demonstrate that on this problem, it is extremely advantageous to keep some poorly parallelized work on the GPU. While the BFGS update takes a significant amount of GPU time (over 12% of the total kernel time, despite having much less arithmetic work than the gradient itself), it is much cheaper than moving the necessary data back to the CPU. The results also show that fusing the line search and gradient+BFGS kernels is unlikely to lead to significant gains: the 10 $\mu$s data-transfer overhead in copying completion flags is dominated by the total kernel execution time. This was borne out in testing: a single-kernel version (with all operations in the same kernel call) had essentially identical performance to the two-kernel version.

## 4.4 LINGO — Algorithmic Transformation and Memory Optimization

Unlike GSO, which is an arithmetic-bound computation with extensive internal data parallelism, LINGO has few arithmetic operations per memory access and has poor data

parallelism. Furthermore, while the GSO algorithm for the GPU is essentially a parallelized version of the CPU GSO algorithm (BFGS), the canonical CPU algorithm for high-performance LINGO is ill-suited to the GPU. This algorithm [34] compiles reference strings into a deterministic finite state automaton, which is simulated for each query string. To implement the DFA state transitions requires either significant amounts of branching, or a moderately-sized, randomly-accessible lookup table (LUT); neither option is good for GPUs. Branch-heavy code will pay a significant penalty in warp divergence. Worse, none of the memory spaces in the CUDA memory model are well-suited to implement a high-performance LUT of the type required: global memory requires aligned, coherent access, texture memory requires spatial locality, constant memory requires that all threads in a warp access the same element for high performance, and shared memory is limited in size. Global, texture, and constant memory are inappropriate for a random-access LUT because different threads are unlikely to use coherent accesses; shared memory is small and may not be able to hold the LUT while maintaining reasonable SM occupancy (necessary to hide the latency of streaming database Lingos in from global memory). In this section, we discuss the design and optimization of SIML, our algorithm to calculate LINGOs efficiently on the GPU [42].

Consequently, an algorithmic transformation is necessary to implement LINGO efficiently on the GPU. The standard LINGO equation (Equation 4.5) can be recast into a different form:

$$T_{A,B} = \frac{|A \cap B|}{|A \cup B|} = \frac{|A \cap B|}{|A| + |B| - |A \cap B|} \tag{4.6}$$

In this equation, each molecule (A or B) is represented as a multiset, a generalization of a set in which each element can have cardinality greater than one; the multiset for a molecule contains its Lingos and their counts. The cardinality of each element in a multiset intersection is the minimum of its counts in either set (or maximum, for a multiset union). SIML thus represents each molecule as a pair of integer vectors: one containing the Lingos in sorted order, and one with corresponding counts. Here, the optimality of $q = 4$ is fortuitous, as it allows us to trivially pack a 4-character Lingo into a 32-bit integer (each character is 8 bits). SIML also precalculates the cardinality of each set independently; thus, the only

```
/* Data: sorted lists A and B containing Lingos,
 *       sorted lists A_c and B_c with Lingo counts,
 *       scalars L_a and L_b the lengths of A/A_c and B/B_c,
 *       scalars m_a = sum(A_c) and m_b = sum(B_c)
 */
float siml(int* A,  int* B,  int* A_c, int* B_c,
           int L_a, int L_b, int  m_a, int  m_b) {
    int i = 0, j = 0;
    int intersection = 0;
    while ( i < L_a && j < L_b) {
        if (A[i] == B[j] {
            intersection += min(A_c[i],B_c[j]);
            i++, j++;
        } else if (A[i] < B[j]) {
            i++;
        } else {
            j++;
        }
    }
    return ((float) intersection) / (m_a + m_b - intersection);
}
```

Listing 4.5: SIML multiset algorithm for calculating LINGO similarities

| **Algorithm** | **Runtime for 8K $\times$ 8K (ms)** | **Throughput (LINGO $\times$ $10^3$/sec)** |
|---|---|---|
| DFA | 11875 | 5651 |
| Multiset/SIML | 19746 | 2888 |

Table 4.3: Multiset vs. DFA algorithm performance on CPU, measured by calculating an 8,192 $\times$ 8,192 LINGO similarity matrix on a Core i7-920.

quantity needed to calculate the similarity between two SMILES string is the size of their multiset intersection. This can be efficiently calculated using the algorithm in the following listing, similar to merging sorted lists (Listing 4.5).

While the simple structure of the algorithm makes it attractive on the GPU, it is not optimal for the CPU. Table 4.3 compares the performance of the SIML multiset algorithm on the CPU against a DFA-based LINGO implementation. The DFA method has nearly twice the throughput of the multiset method. This reflects a common theme in GPU programming: algorithms optimal for the GPU may in fact represent de-optimization for the CPU.

### 4.4.1 SIML GPU implementation and memory tuning

Because of the poor data parallelism in any single LINGO similarity calculation, we use an individual CUDA thread per similarity; each thread in a block calculates the similarity of its query molecule against a common reference molecule for the entire block. While this approach makes good use of task parallelism in large-scale LINGO calculations, simply running Listing 4.5 per-thread on the GPU results in very poor performance. The first optimization is to load the block's reference molecule into shared memory, rather than global memory. Since all threads access the same reference molecule, this significantly reduces global memory traffic. However, this is sufficient only to reach approximate performance parity with the CPU.

The key to performance in the SIML kernel is memory layout. If multisets are laid out in "molecule-major" order (all elements for a single molecule stored contiguously, followed by the next molecule, etc.), as would be appropriate for the CPU implementation of SIML, consecutive GPU threads read from global memory with a stride equal to the length of the largest multiset (Figure 4.4(a)). This stride is typically larger than the global memory request size, so a separate read transaction must be dispatched for every thread. This becomes the critical bottleneck: with molecule-major multiset layout, the CUDA Visual Profiler indicates that the kernel's arithmetic throughput is only 15% of peak on a GeForce GTS 250.

Transposing the multiset layout, such that all multisets' first elements are contiguous, followed by the second elements, and so on, nearly solves the problem (Figure 4.4(b)). However, each thread maintains its own index into its query multiset (a row index in the "Lingo-major" multiset-matrix); if these indices differ, then memory access will be uncoalesced. One option is to have a shared row index among all threads: each thread increments its query multiset pointer as far as possible, and then waits at a barrier (`__syncthreads`) before the block moves on to the next multiset row. While this solution ensures that all global loads are coalesced, it has a relatively high overhead in threads that must wait idle at the barrier; it is able to achieve 80% of peak arithmetic throughput. The best option on GPU hardware is to associate a 2-dimensional texture with the multiset matrix, and use texture loads instead of uncached global loads. Because the texture cache is optimized for spatial locality, it is able to absorb the overhead of the misalignment in row indices between

threads. The SIML kernel using a 2-D texture for global memory access is able to achieve 100% of peak single-issue arithmetic throughput (as measured by CUDA Visual Profiler), demonstrating that careful optimization of memory layout and access method can turn a problem traditionally considered to be memory-bound into one that is arithmetic-bound. An implementation of this transposed, textured kernel is provided as Listing 4.6.

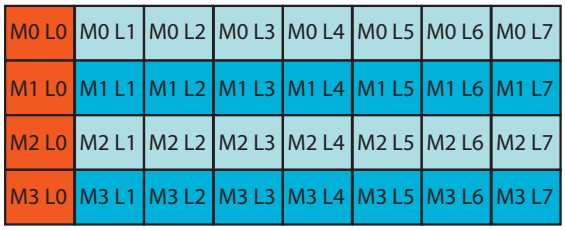


(a) Molecule-major layout for CPU. Each thread proceeds rightwards from a different row, leading to strided, uncoalesced global reads on the GPU without caching.

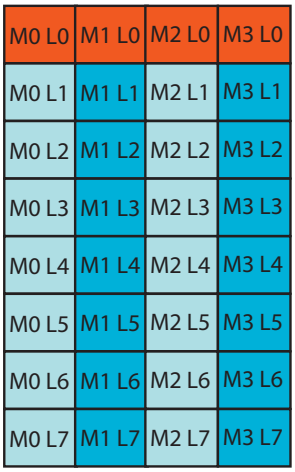


(b) Lingo-major layout for GPU. Threads proceed downwards in adjacent columns. Using a barrier on row index, or a 2D texture, ensures that reads stay coalesced as the calculation proceeds.

Figure 4.4: "Molecule-major" and "Lingo-major" layouts for storing the Lingos of multiple molecules in memory. Red squares indicate the memory addresses read by consecutive threads. "MX LY" indicates the Yth Lingo of the Xth molecule.

## 4.5 Final evaluation

Figure 4.5 compares the performance of the tuned PAPER implementation against OpenEye ROCS, a commercial implementation of Gaussian shape overlay. ROCS supports various "modes", which represent different approximations to the GSO objective function. The objective implemented in PAPER is equivalent to the "Exact" mode in ROCS. ROCS

```
/* Data:
 * sorted list A containing Lingos for reference molecule
 * sorted list A_c containing counts for reference molecule
 * textures B_tex and B_c_tex, pointing to Lingo-major
 *          matrices of query Lingos and counts
 * scalars L_a and L_b the lengths of A/A_c and B/B_c
 * scalars m_a = sum(A_c) and m_b = sum(B_c)
 * scalar maxL_b the longest length of any query molecule
 *               list (height of matrix pointed to by B_tex)
 * scalar b_offset the column index in B_tex containing data
 *        for the query molecule to be processed
 */

texture<int,2> B_tex, B_c_tex;

float siml_colmajor(int* A,   int* A_c, int L_a,    int m_a,
                    int  m_b, int  L_b, int maxL_b, int b_offset) {
    int i=0, j=0, intersection=0;
    int Bj,B_cj;

    // Special-case the empty set
    if (m_a == 0 || m_b == 0) return 0.0f;

    while (j < maxL_b) {
        if (j < L_b) {
            // Use 2D texture to coalesce loads through cache
            Bj   = tex2D(B_tex,   b_offset, j);
            B_cj = tex2D(B_c_tex, b_offset, j);

            while ( i < L_a && a[i] < Bj) i++;

            // Now a[i] >= bj or i == L_a
            if (i < L_a && a[i] == Bj) {
                intersection += min(A_c[i], B_cj);
                i++;
            }
            // Now a[i] > b[j] or i == L_a
        }
        j++;
        // If texturing is not used, synchronize here to coalesce
           loads
    }
    return intersection/((float)(m_a + m_b - intersection));
}
```

Listing 4.6: Transposed SIML algorithm for LINGO using 2D texturing to coalesce reads on the GPU

performance was measured on one core of an Intel Core i7-920; PAPER was run on an NVIDIA GeForce GTX 480. Because the complexity of the GSO kernel varies by the size of the molecules being compared, we present speedup plots for small (10 atoms), medium (22 atoms), and large (44 atoms) molecules. The chosen "medium" size corresponds to the average heavy atom (non-hydrogen) count in a popular chemical screening library.

Two trends are immediately obvious from the graph. First, PAPER requires a large number of molecules to be optimized at the same time for effective speedup. This is typical for GPU algorithms, especially those relying on task-parallelism. Because PAPER only dispatches one optimization per thread block, and the GPU can run multiple thread blocks per GPU core (streaming multiprocessor, or SM, in NVIDIA terminology), it is necessary to dispatch many optimizations before the GPU is fully loaded. Performance continues to improve past this lower bound (present around 25 optimizations in the plot) because CPU-GPU copy overhead and kernel dispatch latency can be more effectively amortized with larger batch sizes. The second trend is that the GPU is less effective for very small molecules, which only achieve slightly more than 10x speedup, rather than the 90-100x possible on larger molecules. The number of interaction terms is very small for such molecules, so that kernel setup, kernel dispatch time, and idle threads come to dominate performance. Ultimately, however, PAPER is able to demonstrate two orders of magnitude speedup on problem sizes typical in our application domain.

Figure 4.6 illustrates the performance of SIML on three generations of NVIDIA GPU, compared to the performance of a DFA-based LINGO implementation (contributed by NextMove Software) running on one core of an Intel Core i7-920. The benchmark problem for both data sets was the computation of an all-vs-all similarity matrix on 32,768 molecules. As shown in Table 4.3, the multiset-based algorithm runs at about half the speed of the DFA algorithm on a CPU. However, the multiset algorithm performs very well on a GPU. SIML achieves over 11x greater throughput than the CPU DFA LINGO implementation on a G92-architecture GeForce GTS 250, and over 23x higher throughput on a GF100-based GeForce GTX 480.

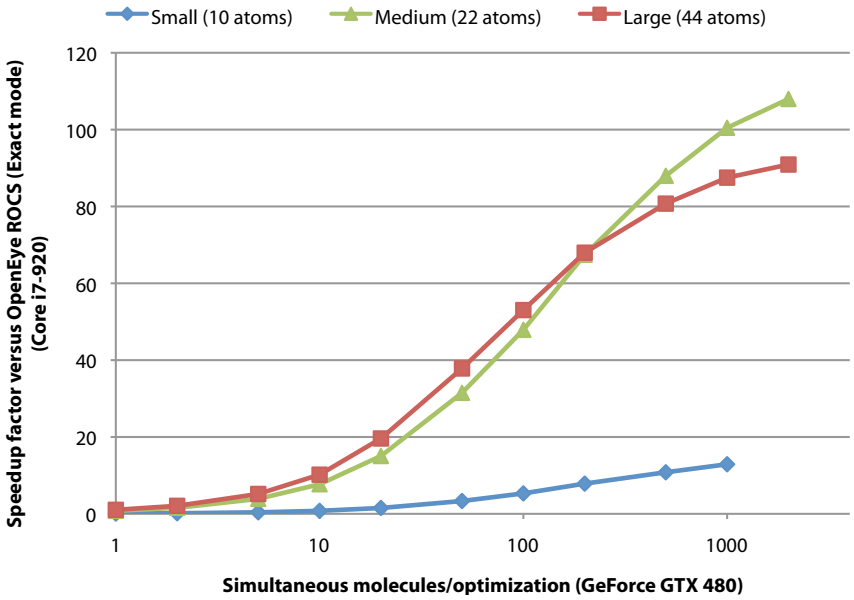


Figure 4.5: PAPER performance versus OpenEye ROCS

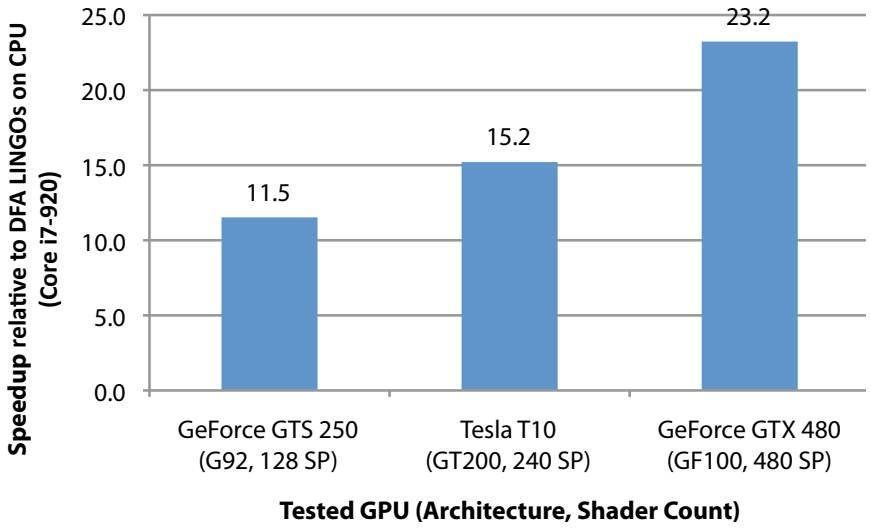


Figure 4.6: SIML performance versus DFA-based LINGOs

## 4.6 Future Directions

We are investigating possible optimizations to both PAPER and SIML. In the PAPER objective/gradient computational core (Listing 4.4), a significant amount of time is spent calculating functions of the reference and query radii that are invariant over the course of the optimization. In particular, the reciprocal and reciprocal square root functions together are as expensive as the following exponential evaluation. One possible option is to precalculate the relevant functions of the radii (`ref_a * query_a * inv` and `8 * PIRTPI * rsq * inv`) and store them in lookup tables in shared memory. This approach has the potential to significantly reduce the number of operations in the core computation, but at the cost of higher memory usage.

The SIML kernel is extremely sensitive to the design of the memory subsystem of the underlying hardware. The version presented has been optimized for the G80/G92 and GT200 NVIDIA architectures, for which texture reads are the only cached reads from global memory. However, the recent GF100 (Fermi) architecture features, in addition to the texture cache, L1 and L2 caches for global memory. It is possible that tuning access methods (such as using non-textured global memory reads) or block sizes (to better fit cache sizes) may significantly affect performance. In general, because LINGO is a memory-sensitive kernel, investigating cache tuning beyond the simple texturing done here is an interesting avenue for future work.

## 4.7 Acknowledgments

We thank Roger Sayle of NextMove Software for his contribution of a DFA-based LINGO implementation for benchmarking and comparison.

# Chapter 5

# SCISSORS: A Linear-Algebraical Technique to Rapidly Approximate Chemical Similarities

## Abstract

Algorithms for several emerging large-scale problems in cheminformatics have as their rate-limiting step the evaluation of relatively slow chemical similarity measures, such as structural similarity or 3-D shape comparison. In this article we present SCISSORS, a linear-algebraical technique (related to multidimensional scaling and kernel principal components analysis) to rapidly estimate chemical similarities for several popular measures. We demonstrate that SCISSORS faithfully reflects its source similarity measures for both Tanimoto calculation and rank-ordering. After an efficient pre-calculation step on a database, SCISSORS affords several orders of magnitude of speedup in database screening. SCISSORS furthermore provides an asymptotic speedup for large similarity matrix construction problems, reducing the number of conventional slow similarity evaluations required from quadratic to linear scaling.

This chapter has previously appeared in reference [40].

## 5.1 Introduction

A fundamental problem in cheminformatics is the calculation of similarity between two given molecules. As a consequence, a large variety of similarity techniques exists [64]. These measures have as their underlying information content a variety of molecular properties, including various encodings of molecular substructure [16, 25, 85], molecular volume [33, 89], molecular surface similarity [46], and electrostatic similarity [61]. While many of the more complicated techniques are able to uncover relevant chemical similarities not found by simpler methods [59, 75], they are often computationally expensive to evaluate.

Many important algorithms in cheminformatics contain as a critical subroutine these pairwise similarity comparisons. For example, database search against a single query (without filters) amounts to the evaluation of a similarity measure once for each database molecule. More complicated algorithms, such as those for clustering [15] or network construction [84] may require the evaluation of a number of similarities quadratic in the size of the database, rather than linear. Evaluation of similarities can be a bottleneck, limiting performance as well as the size of problems that can be considered. While fingerprint-style methods have been developed to approximate these similarity measures [38], they lack rigorous justifications of their accuracy.

A significant continuing trend in cheminformatics is the increasing size of virtual chemical databases. Public libraries listing known chemical matter, such as PubChem (31 million molecules) and ZINC [45] (34 million molecules), are routinely used in database searches. Continuing advances in both computational power and storage space enable the use of even larger exhaustive and combinatorial databases. GDB-13 [8] is an exhaustive database enumerating all 970 million possible compounds composed of 13 or fewer heavy atoms (C, N, O, S, and Cl) according to simple stability and synthesizability criteria. Virtual combinatorial libraries can similarly reach or exceed the $10^9$ molecule mark, even with as few as three or four points of substitution. In the limit, it is believed that as many as $10^{60}$ molecules are potentially synthesizable [9]. The combination of rapidly growing chemical libraries with computationally-difficult similarity metrics suggests a need for dramatically faster methods of calculating chemical similarity.

In this article, we present SCISSORS ("SCISSORS Calculates Interpolated Shape

Signatures Over ROCS Space"), a mathematical technique that allows extremely rapid approximate evaluation of compound similarity for a variety of different similarity measures. In one application of interest, the calculation of an all-pairs similarity matrix over a large number of compounds, SCISSORS offers an asymptotic speedup in terms of the number of similarity calculations required from quadratic to linear scaling. We begin with a mathematical derivation of the SCISSORS algorithm and demonstrate its accuracy at Tanimoto estimation and generalizability to various similarity measures. In the discussion, we present links to a method from machine learning known as kernel principal components analysis, and show how these links justify optimality properties for SCISSORS and offer interesting insights into the nature of chemical shape space. Finally, we present a method by which SCISSORS allows asymptotic speedup (in terms of number of slow similarity evaluations) on the quadratic-scaling problem of similarity matrix construction.

## 5.2 Method

One commonality among otherwise diverse techniques to calculate chemical similarity is that regardless of the underlying method, similarities are often returned as a Tanimoto score. While Tanimotos are often treated simply as real-valued similarities in the range [0,1], they have additional mathematical structure which can be profitably used; this is seen in the definition of the Tanimoto $T_{AB}$ between vectors $A$ and $B$:

$$T_{AB} \equiv \frac{\langle A, B \rangle}{\langle A, A \rangle + \langle B, B \rangle - \langle A, B \rangle} \tag{5.1}$$

Equation 5.1 can be rearranged to obtain an expression for the inner product between two vectors in terms of their Tanimoto:

$$\langle A, B \rangle = \frac{T_{AB}}{1 + T_{AB}} \left( \langle A, A \rangle + \langle B, B \rangle \right) \tag{5.2}$$

Using this equation, the derivation of the SCISSORS method proceeds with two assumptions. We first assume that molecules can be represented as vectors in some (unspecified) inner product space. Given this assumption and a similarity measure on two molecules $f$ and $g$, one can identify these molecules with vectors $A$ and $B$ in Equation 5.2. It then

makes sense to ask for the inner product between the two molecules. Since the Tanimoto between the two is known, we must somehow calculate the "magnitude" of each molecule (the $\langle A, A\rangle$ terms).

In the absence of further information, a parsimonious decision is to arbitrarily set all magnitudes equal to 1 (that is, $\langle A, A\rangle = \langle B, B\rangle = 1$); this is equivalent to assuming that all molecules should lie on the surface of a hypersphere of arbitrary dimension $N$. Alternatively, for certain measures we have more information and can assign meaningful values to the magnitude (see Discussion for an example). For the purpose of the derivation, we take the magnitudes as given (either from parsimony or knowledge of the measure). This implies that it is possible to calculate the inner product between two molecules given their pairwise Tanimoto score.

We further assume that the inner product space in question is $\Re^N$, the space of vectors with $N$ real-number coordinates. Under this assumption, it becomes meaningful to try to map molecules to vectors in $\Re^N$ in such a way as to preserve their inner products. Given a "basis" set of molecules $B = B_1, \cdots, B_k$, $k \geq N$ we require that similarities be computed between all pairs in $B$. These similarities are then transformed to inner products (using a method appropriate for the measure in question), and placed into a matrix $G$ such that $G_{ij}$ contains the inner product between molecules $B_i$ and $B_j$ (a matrix of this form is known in the statistical literature as a "Gram matrix"). We wish to find a factorization of $G$ of the form $G = MM^T$, where $M$ is an NxN matrix containing the molecule vectors along its rows.

Since the elements of $G$ are constructed from molecular similarities, $G$ is real and symmetric, and therefore has a spectral decomposition into eigenvectors V and eigenvalues (in diagonal matrix D). From this, the desired factorization follows by simple algebraic manipulation:

$$\begin{aligned} G &= MM^T = VDV^T \\ &= VD^{\frac{1}{2}}D^{\frac{1}{2}}V^T \\ &= \left(VD^{\frac{1}{2}}\right)\left(VD^{\frac{1}{2}}\right)^T \\ M &= VD^{\frac{1}{2}} \end{aligned} \tag{5.3}$$

The method described in equation 5.3 is also used to derive vector coordinates from inter-point distances in classical multidimensional scaling (MDS) [22]. It has several properties which make it an appealing choice relative to other matrix factorizations (such as the Cholesky decomposition, which also finds matrix $M$ such that $G = MM^T$ [31]). First, the MDS reconstruction of molecule vectors in N dimensions is guaranteed to most closely approximate the given inner products, in a least-squares sense. Furthermore, the reconstruction dimension can easily be chosen by sorting the eigenvalues in order of decreasing value, and setting to zero all eigenvalues after the first $K$ (for an $K$-dimensional reconstruction). Our method is also very closely related to a technique known as kernel PCA [77, 78]; this relationship has interesting consequences explored in the Discussion.

One mathematical detail skipped in the derivation of equation 5.3 relates to the square root performed on the eigenvalues. If the measure described by the inner products in $G$ is a Euclidean metric, then $G$ will be positive semi-definite (i.e., it will have only zero- or positive-valued eigenvalues) [22], and the square root will exist. However, there is no guarantee that a generic molecular similarity measure will be a Euclidean metric (and we show in our results that several popular measures are not). Because of the optimality properties of MDS, however, the impact that these negative eigenvalues have on the approximation depends on their magnitude relative to the positive eigenvalues. If no negative eigenvalue has magnitude within the top $K$, then it would not be used in the $K$-dimensional reconstruction, and does not affect the solution. We demonstrate in our results that for many popular measures, negative eigenvalues are of sufficiently small magnitude that they do not affect the reconstruction, and that these non-Euclidean measures can therefore be well-approximated by Euclidean inner products. Furthermore, in the following section we describe a correction factor that can be added to the basic MDS formula to allow interpolation of coordinates associated with negative eigenvalues.

### 5.2.1 Correction Factors

One drawback of our inference procedure is that the optimization procedure (Equation 5.3) does not respect the vector magnitude assumptions made at the beginning in the first step. In particular, given any molecule $A$ in the basis set with square-magnitude $\langle A, A\rangle = x$ and its

low-dimensional vector approximation $\hat{A}$, the approximated square-magnitude $\left\langle \hat{A}, \hat{A} \right\rangle$ will always be smaller than $x$, because we have ignored the magnitude associated with higher (less-significant) dimensions.

As will be shown in the Results, this loss of magnitude can cause problems with the absolute accuracy of resulting Tanimoto values (though rank orderings are often preserved). One possible strategy for solving this problem would be to replace Equation 5.3 with a constrained optimization method; however, the simplicity and ubiquity of implementation of a method based on the spectral decomposition suggest that a procedure to correct the results of the eigenvector decomposition would be useful. Consequently, we choose not to examine constrained optimization methods, although this may be an interesting direction for future work.

A simple correction technique is to simply scale each result vector to force its magnitude to 1. Our testing showed this to be ineffective (data not shown). However, one correction technique, which we call the slack coordinate method, did improve accuracy and furthermore allows us to represent non-Euclidean geometries.

### Slack coordinate method

Without loss of generality, we consider only the case in which we wish to correct all vector magnitudes to unity. Given real vectors $A$ and $B$ of arbitrary dimension $n$ (i.e., $A, B \in \Re^n$) with magnitude less than one, we construct vectors $\tilde{A}$ and $\tilde{B}$ of unity magnitude by augmenting them with one additional "slack" coordinate, as follows:

$$\begin{aligned} \tilde{A} &= [a_0\, a_1\, \cdots\, a_{n-1}\, a_n]^T \\ \tilde{B} &= [b_0\, b_1\, \cdots\, b_{n-1}\, b_n]^T \\ ||\tilde{A}|| &= \hat{A}^T \hat{A} = 1 \\ a_n &= \pm\sqrt{1 - \sum_{i=0}^{n-1} a_i^2} \qquad b_n = \pm\sqrt{1 - \sum_{i=0}^{n-1} b_i^2} \end{aligned} \tag{5.4}$$

An interesting aspect of this correction is that the slack coordinate is incompletely specified, as the sign is indeterminate. As in the scaling case, we can derive an analytic

correction for the resulting Tanimoto. For convenience, we define variables $k_1$ and $k_2$, corresponding to the numerator and denominator, respectively, of the uncorrected Tanimoto equation:

$$T_{AB} = \frac{\sum_{i=0}^{n-1} a_i b_i}{\sum_{i=0}^{n-1} a_i^2 + \sum_{i=0}^{n-1} b_i^2 - \sum_{i=0}^{n-1} a_i b_i} = \frac{k_1}{k_2} \tag{5.5}$$

We can then define the corrected Tanimoto in terms of these variables, and simple algebraic transformations allow us to express the correction as a function of the uncorrected Tanimoto and the (uncorrected) magnitudes of $A$ and $B$:

$$\begin{aligned}
||A||^2 &= \sum_{i=0}^{n-1} a_i^2 \qquad ||B||^2 = \sum_{i=0}^{n-1} b_i^2 \\
T_{\tilde{A}\tilde{B}} &= \frac{\sum_{i=0}^{n} a_i b_i}{\sum_{i=0}^{n} a_i^2 \sum_{i=0}^{n} b_i^2 - \sum_{i=0}^{n} a_i b_i} \\
T_{\tilde{A}\tilde{B}} &= \frac{k_1 + a_n b_n}{k_2 + a_n^2 + b_n^2 - a_n b_n} \\
T_{\tilde{A}\tilde{B}} &= \frac{k_1 \pm \sqrt{1 - ||A||^2}\sqrt{1 - ||B||^2}}{(2 - k_1) \mp \sqrt{1 - ||A||^2}\sqrt{1 - ||B||^2}} \\
k_1 &= \frac{T_{AB}\left(||A||^2 + ||B||^2\right)}{(1 + T_{AB})} \\
k_3 &= \pm\sqrt{1 - ||A||^2}\sqrt{1 - ||B||^2} \\
k_4 &= k_1 + k_3 \\
T_{\tilde{A}\tilde{B}} &= \frac{k_4}{2 - k_4}
\end{aligned} \tag{5.6}$$

Although the sign of the slack coordinate ($\pm\sqrt{1 - ||A||^2}$ or $\pm\sqrt{1 - ||B||^2}$ for molecules A and B, respectively) is unspecified, the analytic correction term $k_3$ is not directly dependent on the particular signs of the slack coordinates. Rather, if A and B are real vectors, $k_3$ has sign determined by whether A and B have the same or opposite signs in their slack coordinate. The case in which $k_3$ is always negative (that is, all pairs of vectors A and B have

opposite signs in their slack coordinates) turns out to be especially useful. However, this case is not realizable if we restrict our vectors $\tilde{A}$ and $\tilde{B}$ to lie in $\Re^{n+1}$. As a demonstration, consider three vectors $\tilde{A}$, $\tilde{B}$, and $\tilde{C}$ with slack coordinates $a_n$, $b_n$, and $c_n$. Without loss of generality, let $a_n$ be negative and $b_n$ be positive. For $c_n$ to always have opposite sign to any molecule it was compared to, it would have to be positive when molecule C is compared with molecule A and negative when compared to B; this is a contradiction.

Although this style of correction term cannot be implemented with real vectors, by generalizing the vector space, this result is easily understood. The case in which every pair of vectors is associated with a negative correction term $k_3$ corresponds to vectors lying in $\Re^n \times \Im$, where the slack coordinate is always positive in sign and purely imaginary (e.g., in equation 5.4, let $a_n = i\sqrt{1 - \sum_{i=0}^{n-1} a_i^2}$, with $i = \sqrt{-1}$). Strictly, this interpretation requires that equation 5.4 be modified so that the Hermitian transpose is used, but does not affect the rest of the derivation. The geometry implied by this vector space is known as pseudo-Euclidean, in contrast with the Euclidean geometry of $\Re^{n+1}$, and has the capability to represent curved spaces. In particular, imaginary coordinates of this form can be used to represent the curved dimensions induced by negative eigenvalues in the Gram matrix [68]. The slack coordinate correction, by generalizing from real to complex vectors, allows approximation of non-Euclidean distance measures.

### 5.2.2 Fast approximation of new vectors

The above procedure for deriving molecule vectors requires computation of O($k^2$) molecular similarities. It therefore does not scale to computing vectors over large libraries of millions of compounds. However, given a fixed "basis" set of molecules, it is possible to approximate vectors for new molecules in a fixed amount of time for each new molecule by least-squares. Specifically, given a "library" molecule (that is, one not originally in the basis set) $L_i$ and the matrix $M$ of basis vectors, a vector for $L_i$ can be constructed by the following procedure:

1. Compute similarities between $L_i$ and all basis molecules $B_j$
2. Transform similarities to inner products $G_{ij}$
3. Store inner products in a vector $T = [G_{i1}, G_{i2}, \cdots, G_{ik}]^T$

4. Solve equation $M\vec{x} = T$ by linear least squares

The resulting vector $\vec{x}$ contains the vector that best approximates the given inner products, in a least-squares sense, and therefore is the molecule vector for molecule $L_i$. This procedure allows the approximation of vectors for a large library of molecules in time linear in the size of the library. It is, furthermore, embarrassingly parallel once the basis set has been computed, making it a computationally attractive method for operation on large libraries.

## 5.3 Results

Full details of the testing methods used in this work, including exact molecule counts, software versions used, and software settings, are included in the Appendix.

### 5.3.1 Similarity Measures

To demonstrate the generality of the SCISSORS technique, we have tested it against similarity measures of various types, as implemented in the OpenEye Scientific Software oechem, oeshape, and oeet toolkits[1]. Representing substructure-fingerprint-based methods is LINGO, a similarity measure which counts the number of substrings in common between the SMILES representation of a pair of molecules [85]. ROCS [75], a 3D shape comparison method which finds the maximal volume overlap between Gaussian representations of molecule shape, represents 3D shape methods. A variation on shape-based ROCS, known as the ROCS Color Tanimoto, uses a similar volume overlap optimization on virtual "color" atoms representing chemical functionalities. We use this color ROCS to demonstrate the generalizability of SCISSORS to 3D methods that include distinct atom types, not all of which interact with one another. Finally, ZAP [59], a Poisson-Boltzmann solver which calculates and compares electrostatic fields around molecules, represents electrostatic similarity methods.

[1] OpenEye Scientific Software, Santa Fe, NM

### 5.3.2 Molecules Tested

We draw molecules for testing from a diverse set of collections of drug- and drug-like molecules. Most of our tests are performed on a 57,253 molecule database, hereafter named "Maybridge+BBP" constructed from the union of the Maybridge Screening Collection and a blood-brain barrier penetration dataset [54]. For Maybridge+BBP, 3-D conformers were generated using OpenEye's OMEGA software. When calculating Tanimotos using ROCS, multi-conformer (200 conformer maximum) fit molecules were aligned against single-conformer references, and the maximum Tanimoto over any pair of conformations for the molecule pair was used. Detailed configuration parameters passed to ROCS and OMEGA are included in the Appendix.

In the test for generalizability of SCISSORS, we used the 1,665 molecules tested in PubChem Assay #677, an assay for novel allosteric modulators of the M1 muscarinic receptor. To test the sensitivity of the SCISSORS technique against the source of molecules for the basis set, we draw basis molecules from the Maybridge+BBP set and also from the Asinex Gold Collection and the Maybridge Fragment Library, commercial libraries used for compound and fragment screening. Finally, the virtual screening test draws its molecules from the Directory of Useful Decoys, version 2 [44], a computational drug-discovery data set specifically designed to confound methods based on common physical parameters, such as molecular weight and cLogP. For all 3-D similarity measures other than the 57,253 molecule Maybridge+BBP set, molecules were assigned single conformers by OpenEye's OMEGA software. Charges for all molecules were assigned using the AM1-BCC charge model implemented in OpenEye's oequacpac toolkit.

Differences in setup (i.e., multi-conformer vs single-conformer) between datasets are due to the fact that we made use of existing databases already in use for other drug discovery projects. These differences are not significant to the content of the paper. Insofar as the goal of SCISSORS is to reproduce the results of existing similarity measures, we demonstrate comparable performance to the source similarity measure regardless of how the molecules were prepared for the source measures.

### 5.3.3 Basis size and dimensionality

To evaluate SCISSORS' ability to approximate molecular similarities on data sets of varying size, we used SCISSORS to approximate the ROCS shape Tanimoto for test sets of 19,000 and 50,000 molecules drawn at random from Maybridge+BBP. This was performed multiple times over a large number of basis sizes and dimensionalities (in all cases, the 19,000 or 50,000 library molecules were disjoint from the basis molecules). Tanimotos were computed using multi-conformer query molecules matched against single-conformer references; the Tanimoto of the best-matching query conformer against the reference was used as the Tanimoto for the molecule pair. Detailed settings for ROCS are provided in the Appendix. As a measure of performance, we calculated the RMS deviation between the SCISSORS Tanimoto and the ROCS Tanimoto over all pairings of these 19,000 molecules (5.1; 19,000 x 19,000 = 361 million Tanimotos) or 50,000 molecules (5.2; 50,000 x 50,000 = 2,500 million Tanimotos).

Two trends are evident from the data. First, the error in the SCISSORS approximation of the shape Tanimoto falls rapidly at first with the addition of more dimensions, and then levels off around 75-100 dimensions. Most of the error falloff occurs in the first few dimensions, with gains beyond 30 dimensions coming much more slowly. A similar trend also appears for basis size — a large error is present for small basis sizes (especially in high-dimensional approximations), as a consequence of overfitting the vector model, but this falls off rapidly as the basis size increases. This result is stable even as we scale to a data set more than double the size. The test set comprising 50,000 molecules required neither more eigenvectors nor a larger basis set to achieve RMS error comparable to that found on the 19,000 molecule test set. Ultimately, SCISSORS is able to approximate the ROCS shape Tanimoto to within approximately 0.08 RMS error around 75-100 dimensions and a basis size of 500-1000, for both the 19,000- and 50,000-molecule test sets.

### 5.3.4 Basis selection strategies

To test the sensitivity of the SCISSORS technique to how the basis set is chosen, we compared randomly-chosen basis sets with basis sets chosen such that basis molecules corresponded to "representative" shapes in the dataset. To choose representative molecules,

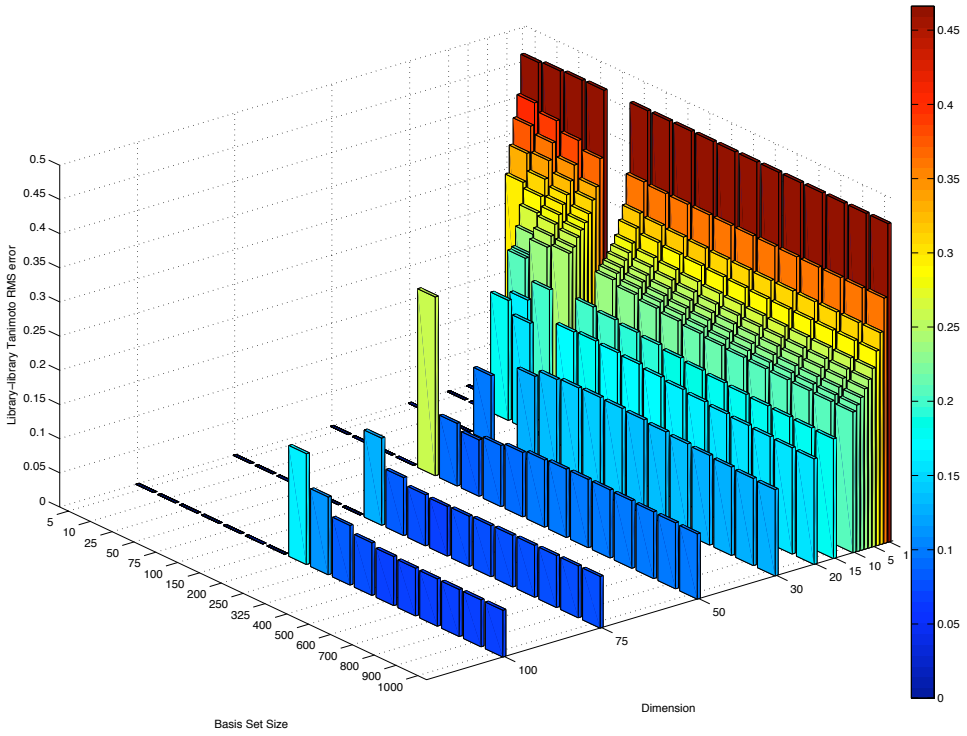


Figure 5.1: RMS Tanimoto error versus basis size and dimensionality of approximation for standard SCISSORS technique on ROCS Shape Tanimoto. 19000 library molecules (361M total Tanimotos) used to calculate RMSE. Each bar averaged over at least 10 random bases of given size.

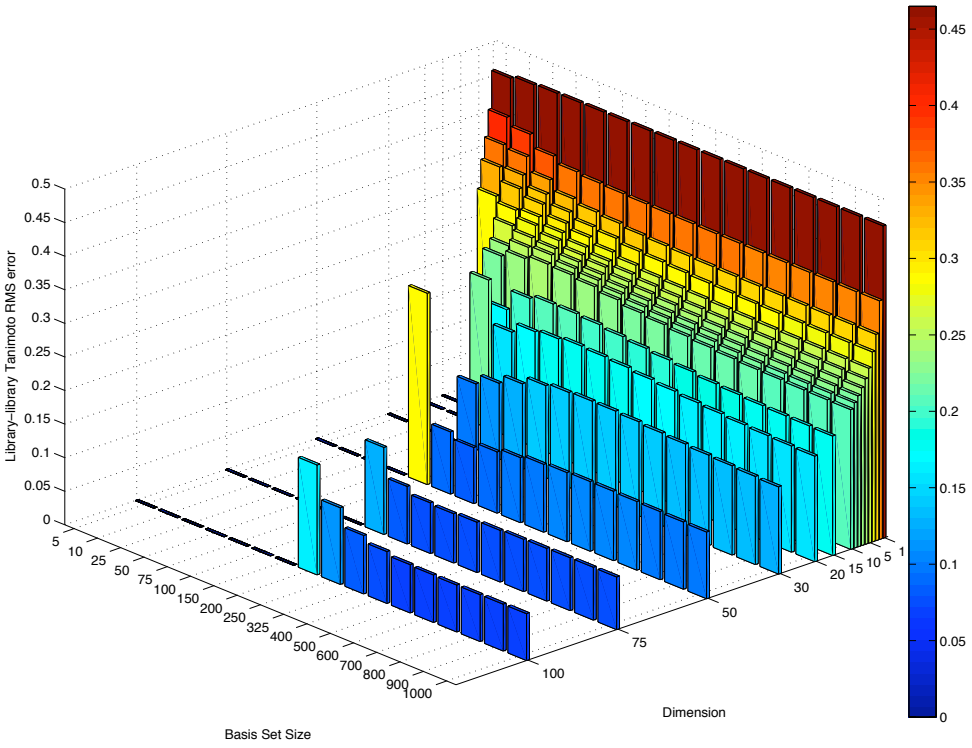


Figure 5.2: RMS Tanimoto error versus basis size and dimensionality of approximation for standard SCISSORS technique on ROCS Shape Tanimoto. 50000 library molecules (2500M total Tanimotos) used to calculate RMSE. Each bar averaged over at least 10 random bases of given size.

we clustered the Maybridge set using the dbclus algorithm [15] at several Tanimoto cutoff values; the cluster centers chosen were used as the representative shapes. For each measured basis size N, we ran SCISSORS in 75 dimensions using a basis consisting of N randomly-chosen molecules, or the N cluster centers with largest number of neighbors (ties broken at random). The resulting library RMS errors are plotted in 5.3.

For any basis set larger than 200 molecules, it was possible to find a SCISSORS approximation with lower error than that resulting from the random basis; however, in all cases such error reduction was extremely small: on the order of 0.005 Tanimoto units. Interestingly, the optimal clustering Tanimoto value differed by basis size. The optimal Tanimoto (that is, the cluster set with lowest RMS error) increased with increasing basis size, suggesting that as more basis molecules are added, it is somewhat advantageous to select tighter clusters as basis elements.

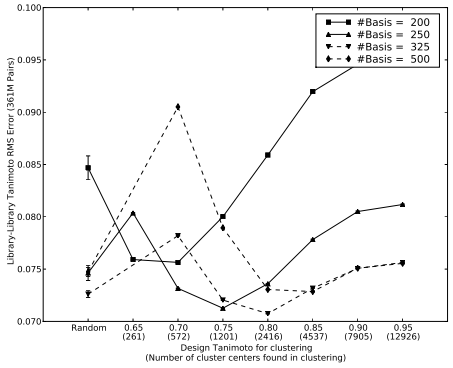


Figure 5.3: RMS Tanimoto errors for SCISSORS approximations to ROCS shape Tanimoto constructed from randomly-selected basis sets and basis sets chosen by molecule clustering. All Tanimotos evaluated over 361M molecule pairs.

### 5.3.5 Corrected Tanimotos

In 5.4 we examine the effect of the slack coordinate correction term introduced earlier. Because the purpose of the correction term is to account for eigenspectrum density truncated in a low-dimensional approximation, we examine two cases, 10 and 75 dimensional approximations. 5.4 is a density plot of SCISSORS standard and corrected Tanimotos versus ROCS Tanimotos using the 19,000 molecule test subset of Maybridge+BBP also used in 5.1. In

5.4, density contours that are symmetric about $Y = X$ indicate that the plotted Tanimoto values have an unbiased or independent error with respect to the original Tanimoto value, which aids in the preservation of rank ordering.

As expected from the earlier results, in 75 dimensions, the standard SCISSORS Tanimoto values are tightly clustered along the $Y = X$ line, and the contours of the density plot continue to be aligned along this $Y = X$ axis even out to low densities, indicating an overall preservation of rank-ordering. In contrast, in 10 dimensions, the SCISSORS Tanimotos, as expected, almost always overestimate the true Tanimoto. Furthermore, the contours are no longer ellipses symmetric about $Y = X$ (or a parallel line), which indicates poorer rank-ordering performance.

As expected, the slack coordinate correction leaves the high-dimensional case largely unaffected, with the major exception of a large group of errors at ROCS Tanimoto = 1.0. These are caused by self-comparisons — the slack coordinate method does not respect the constraint that the Tanimoto of a vector against itself ought to be 1. However, in the low-dimensional case, the slack correction makes a significant difference. Leaving aside the known artifact at ROCS Tanimoto = 1.0, the overall shape of the density contours is shifted below the diagonal, but is symmetric. This indicates that with the exception of a constant shift, the slack-corrected values are much more accurate than the uncorrected low-dimensional values.

### 5.3.6 Virtual screening

To illustrate the utility of SCISSORS-derived Tanimoto values in virtual screening, we used SCISSORS on the ROCS shape Tanimoto to do a virtual screen on the Directory of Useful Decoys (DUD) test set. DUD is a collection of "systems" consisting of target proteins and associated small molecules. For each system, a certain number of molecules known to bind the target are designated as "ligands"; the rest of the molecules (36 times the number of ligands) are "decoys" with similar physical properties believed to not bind the target. We used a previously-published protocol [39] to evaluate performance and statistical significance; for clarity, we summarize the protocol below.

For each protein system in DUD, we used ROCS and SCISSORS (with three different

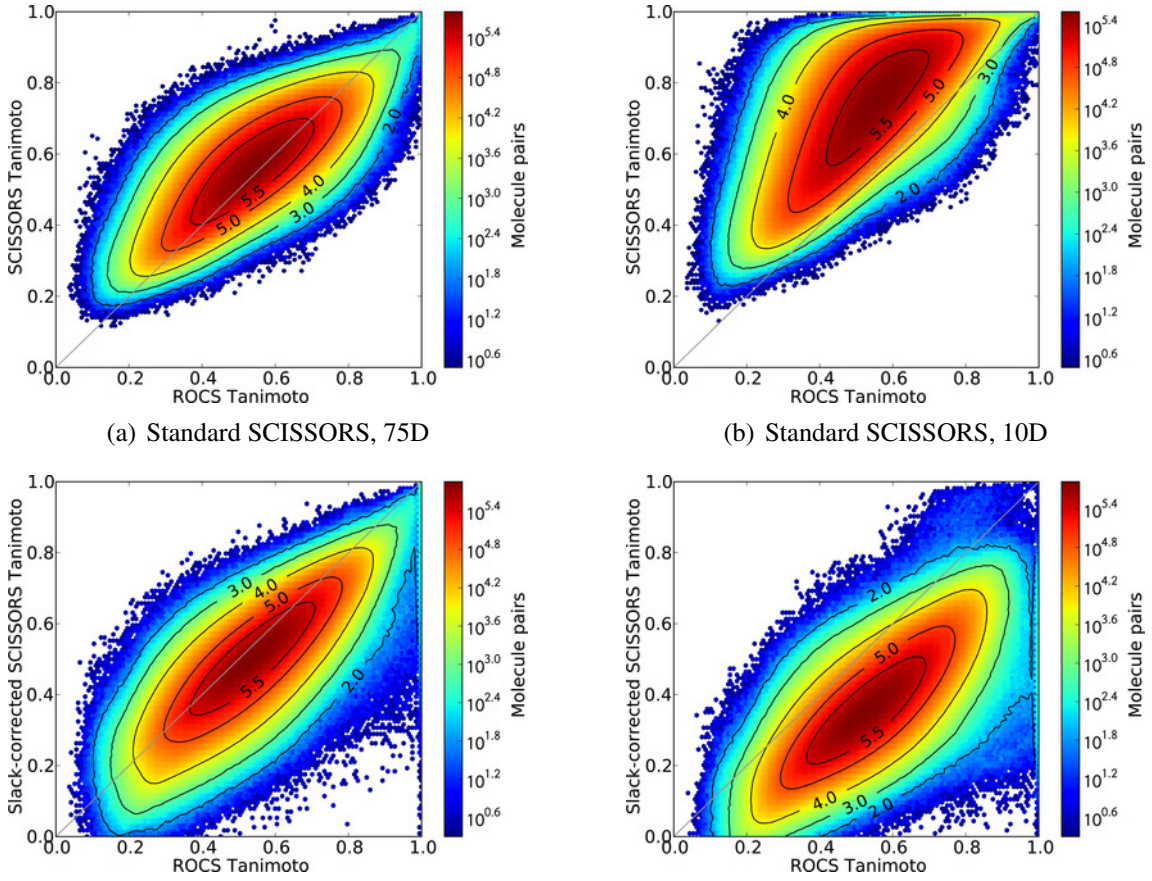


(a) Standard SCISSORS, 75D

(b) Standard SCISSORS, 10D

(c) Slack-corrected SCISSORS, 75D

(d) Slack-corrected SCISSORS, 10D

Figure 5.4: Density plots of SCISSORS and slack-corrected SCISSORS Tanimoto approximations of ROCS Shape Tanimoto for 361M molecule pairs from Maybridge. Contours are labeled as $\log_{10}$ of contour height. Light gray $y = x$ line drawn for reference.

basis sets) to calculate the Tanimoto of every ligand molecule against every other molecule in the system. For each ligand molecule, we ranked all other molecules in order of decreasing Tanimoto similarity, modeling a screening experiment in which given one active compound, one wishes to find other actives in a pool of inactive molecules. All molecules used were single-conformer; settings for ROCS are given in the Appendix. All SCISSORS Tanimoto values were computed in 10 dimensions as uncorrected SCISSORS Tanimotos. Basis sets were drawn from the Maybridge Screening Collection, the Asinex Screening Collection, and the Maybridge Fragment Library to illustrate the effects of different basis choices on performance.

The ROC AUC for this ranking was calculated according to the method in Clark [20]. Ligand molecules were considered true positives; false positives were any decoys ranked higher than a true ligand. A bootstrapping procedure [39] was used to estimate the 68% and 95% confidence intervals on the calculated AUC values. These AUCs and confidence intervals are illustrated in 5.5.

For almost all systems, the performance of the different SCISSORS basis sets are statistically indistinguishable from each other and from that of the original ROCS Tanimoto. In particular, the Maybridge and Asinex basis sets, which are drawn from different libraries but which likely have overall similar characteristics (as both are screening libraries) perform almost identically. The Maybridge Fragment basis is an outlier on several systems; it is likely that this is because these molecules are significantly smaller (in volume/mass) than the druglike molecules in DUD, indicating that at least rudimentary physical property matching is a prudent step in the use of SCISSORS. It is interesting, however, that there were so few outliers using the fragment basis set, as similarity measures often fail when comparing fragments to elaborated molecules; we have not explored the reasons for this performance in detail.

### 5.3.7 Similarity measure generalizability

To assess the generalizability of SCISSORS to chemical similarity measures other than the ROCS shape Tanimoto, we evaluated the performance of SCISSORS on four similarity measures: ROCS shape, ROCS color, LINGO, and ZAP's ET, or electrostatic Tanimoto.

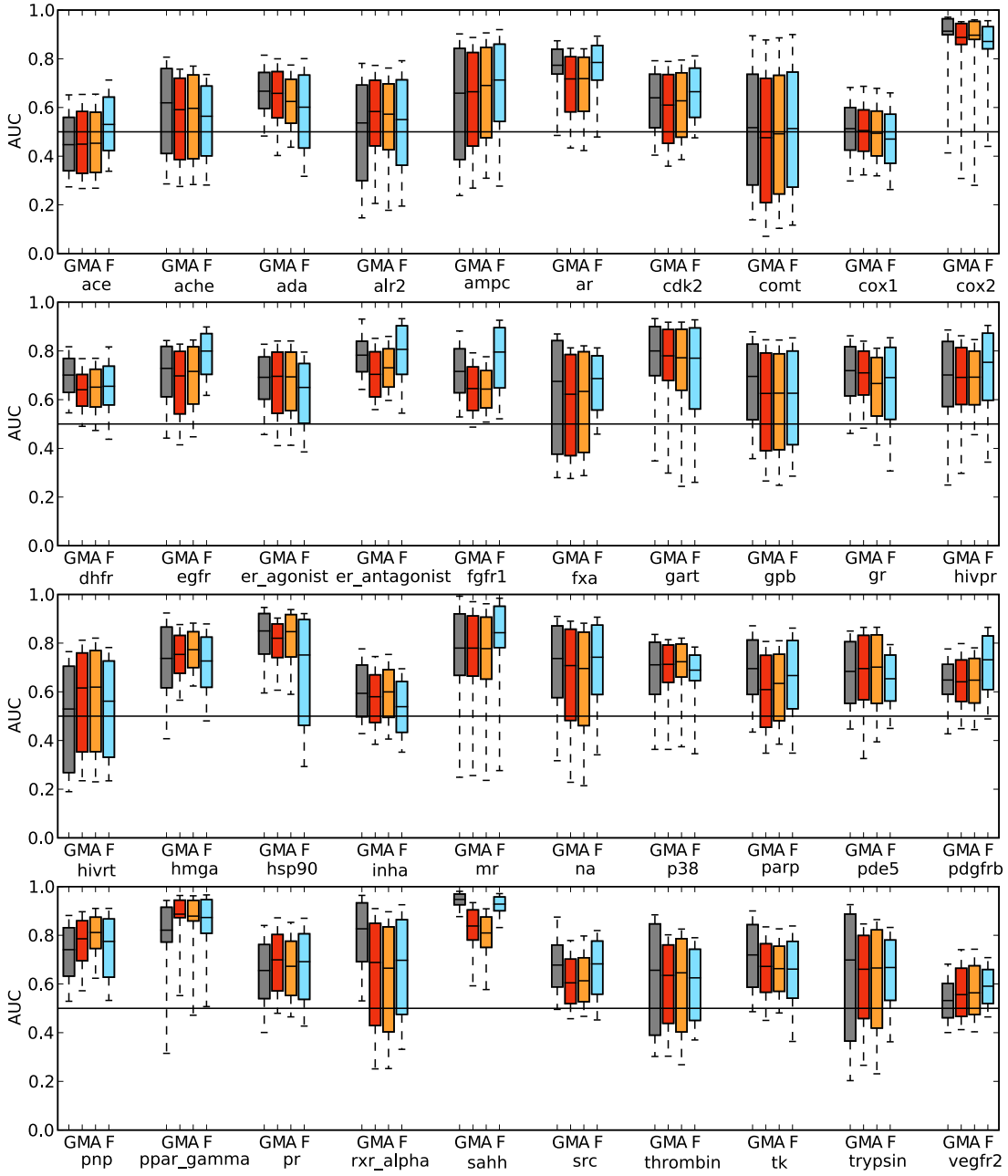


Figure 5.5: ROC AUC values on each system of the DUD test set. Reported are the mean AUC, averaged over each ligand in the system (line), the 68% confidence interval on the AUC (box), and the 95% confidence interval on the AUC (whiskers). Within each system, results are reported for ROCS (G, gray) and SCISSORS using basis sets from the Maybridge Screening Collection (M, red), the Asinex Screening Collection (A, orange), and the Maybridge Fragment Library (F, blue). All SCISSORS approximations were done in 10 dimensions; Maybridge and Asinex sets used a 500-molecule basis set; the Maybridge Fragment set was 473 molecules, the size of the entire library.

All Tanimotos were originally evaluated on a collection of 1,665 small molecules from a screen for allosteric modulators of the M1 muscarinic receptor; for SCISSORS, both basis and library molecules were drawn from this same pool. All tests were conducted with 1,000 library molecules, with RMS errors evaluated over an all-pairs (1,000 x 1,000 = 1 million Tanimotos) similarity comparison. For the electrostatic Tanimoto, molecules were first overlaid using ROCS before electrostatic field calculation.

5.6 plots the SCISSORS Tanimoto RMS error for each similarity measure in the large basis (600 molecules) limit as a function of dimensionality. Three trends are particularly notable. First, on this dataset, all the similarity measures show non-monotonic error behavior as the number of dimensions increases, most likely reflecting eventual overfitting (an insufficient number of basis molecules for further dimensions). Second, SCISSORS generalizes well to approximating both the ROCS color and the LINGO Tanimotos, with RMS errors under 0.1 in both cases. Finally, ZAP's electrostatic Tanimoto appears to be inapproximable by the SCISSORS method.

5.7 explores why only certain measures are approximable by SCISSORS. Each subplot plots the value of the top 300 eigenvalues from a basis set of size 1000 computed for each of the four similarity measures, on a log scale. For all three well-approximated measures, the magnitude of the 100th eigenvalue has fallen off more than 2 log units relative to the first (largest) one, indicating that high dimensions rapidly become less important to the approximation. In contrast, the ET Tanimoto's eigenspectrum falls off much more slowly — even after 300 dimensions, it has not fallen 2 log units. It is this characteristic of the eigenspectrum (insufficiently rapid falloff) that makes a low-dimensional linear approximation to the ET Tanimoto impossible.

### 5.3.8 Tanimoto Computation Speed

The precalculation step of SCISSORS is extremely efficient compared to the evaluation of the source similarity measure. We benchmarked the precalculation step for calculating molecule vectors on a 20,480 molecule subset of Maybridge+BBP, using a 500 molecule basis set drawn from the same database. Timings for each phase of SCISSORS precalculation on one core of a 3GHz Intel Xeon-based (Core 2-architecture) Mac Pro are presented in 5.1 (further

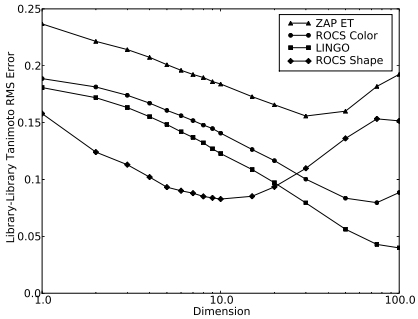


Figure 5.6: RMS Tanimoto error from SCISSORS approximations to several molecular similarity measures, as a function of dimensionality of approximation. All tests conducted with basis size of 600 molecules and test set size of 1000 molecules.

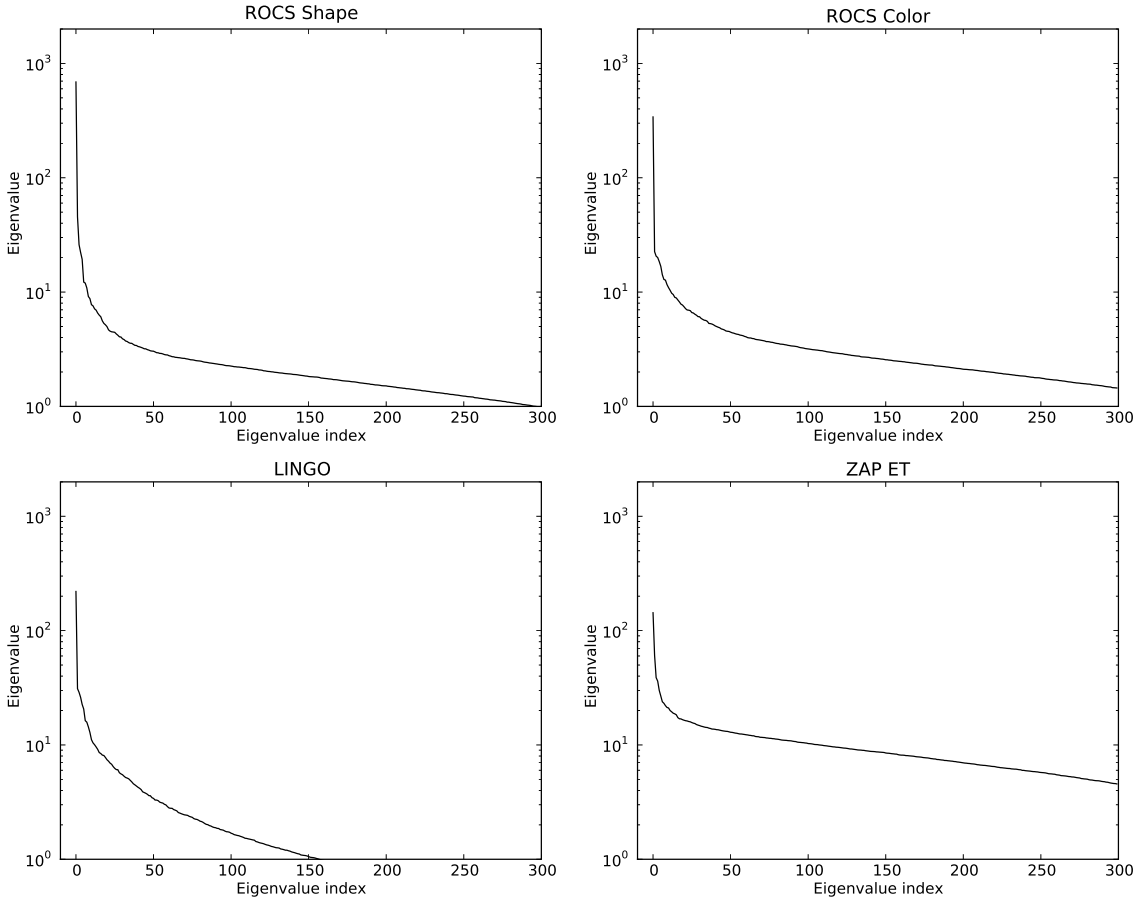


Figure 5.7: Eigenvalue spectra for Gram matrices resulting from four similarity measures on 1000 molecules from the M1 muscarinic data set

machine details are presented in the Appendix). The precalculation time is dominated by ROCS calculations; the spectral decomposition and least squares inference for SCISSORS take less than 5 seconds, compared to nearly 11 000 seconds for the basis-vs-basis and library-vs-basis ROCS computations.

A significant benefit of SCISSORS is that it calculates accurate estimates of molecular similarity extremely rapidly once library vectors have been inferred. This is particularly true in the case of the ROCS shape and color similarities, which are industrially important, but expensive to calculate. We measured the OpenEye ROCS implementation's performance at approximately 1000 comparisons/sec per core on a 3GHz Mac Pro while performing the basis-basis and library-basis ROCS comparisons for the above benchmark. In contrast, our C code to evaluate SCISSORS Tanimotos (compiled with gcc 4.0.1 and GotoBLAS2 [32]) is capable of computing approximately 50 million similarities (in 64 dimensions) per second on one core of the same CPU. With precomputed library vectors, then, SCISSORS is around 50,000 times faster than a direct calculation of Gaussian overlap.

Indeed, SCISSORS is fast enough that for very large similarity-matrix problems, it can be faster to recalculate similarities on the fly from SCISSORS vectors than to precalculate all similarities and read them back from disk. This leads to a significant savings in storage, as the storage required for the molecule vectors scales as O(N), while storage for a similarity matrix scales as O($N^2$). The combination of high computation speed and reduced storage makes similarity calculations computationally feasible for datasets with N on the order of $10^5$ to $10^7$ for large scale virtual screening and data analysis. While SCISSORS does not solve other issues involved with large data sets (e.g., file handling and molecule preparation), it is able to reduce both the computational and total data storage burdens for large-scale problems. In terms of CPU time alone, it can make difficult problems easy, and impossible problems difficult.

| **Step** | **Time** (sec) |
|---|---|
| Basis-matrix ROCS calculation | 262 |
| Basis vector calculation (eigendecomposition) | 0.33 |
| Library-vs-basis ROCS calculation | 10732 |
| Library vector calculation (least squares) | 4 |

Table 5.1: SCISSORS precalculation step timings for 20,480 library molecules using 500 molecule basis set, using one core of a 3GHz Intel Xeon-based Mac Pro

## 5.4 Discussion

### 5.4.1 Connections to Previous Work

#### Previous Methods to Characterize Chemical Space

Several methods have been applied in past work to characterize chemical space by learning relevant dimensions along which chemicals vary to find vector embeddings of molecules. In this section we discuss past work which has used multidimensional scaling and other similar techniques to find vector embeddings of molecules based on particular similarity representations.

Multidimensional scaling has previously been applied to chemical datasets in order to reduce the dimensionality of binary molecular fingerprints [17, 57]. This approach has been used for combinatorial library design; by computing coordinates for each molecule and treating each dimension as a property, it is possible to maximize the distance among molecules to select a maximally diverse library [57]. However, using MDS directly in this manner is not scalable to large compound sets, as it requires a full $N^2$ similarity matrix.

There have also been prior efforts to develop scalable versions of MDS-based methods. One method, due to Nicholls [60], focuses on similarity *metrics*; that is, on similarity measures that compute a distance between pairs of molecules, such that these distances obey the triangle inequality. The Nicholls method, after computing coordinates for a basis set of molecules using MDS, computes coordinates for a new non-basis molecule by triangulation based on distances to each of the basis molecules.

The principal difference between SCISSORS and these older MDS-based methods is our use of least-squares approximation to calculate coordinates for non-basis molecules. Least

squares allows SCISSORS to scale well to large datasets, unlike the original methods using MDS for dimensionality reduction. Furthermore, because we approximate inner products rather than distances, and use least-squares rather than triangulation to calculate coordinates, we do not assume that the approximated similarity measures are true metrics. In particular, the use of least squares allows SCISSORS to calculate approximate coordinates even in the non-metric source similarity case (in which the triangulation equations would have no consistent solution). The SCISSORS similarity is a metric (or pseudometric, in the case of the slack-corrected Tanimoto) approximation to the source measure.

Raghavendra and Maggiora [71] developed a symmetric-orthogonalization method (similar in some respects to SCISSORS) to calculate vector embeddings of molecules in an arbitrary similarity space. Like SCISSORS, the Raghavendra and Maggiora (RM) method calculates a pairwise similarity matrix on a small set of basis molecules, uses this to find vectors for the basis, and then projects library molecule vectors onto this space by transforming library-basis similarity values. It is presented only as a method to describe chemical space, and not as a method to approximate similarities. Several mathematical limitations impact the applicability of this method for both purposes.

One critical difference is in the treatment of the basis similarity matrix, the entries of which are Tanimotos. The RM method treats these entries as though they were inner products; however, as equation 5.1 shows, the Tanimoto is a function of an inner product, but not an inner product itself. This inaccuracy will distort vector spaces inferred by the method. Furthermore, this method is unable to handle molecular similarities which do not result in positive definite Gram matrices (i.e., non-Euclidean measures). SCISSORS handles these in two ways. First, the use of the slack correction allows approximation of dimensions associated with the negative eigenvalues in a non-positive-definite similarity measure. Second, a typical use of SCISSORS will retain fewer eigenvalues/eigenvectors (SCISSORS dimensions) than can be computed from the matrix. This allows a positive-definite approximation of non-positive-definite measures. It also improves the statistical reliability of our vector approximations. The RM method projects library molecules onto the full number of dimensions computed from the basis matrix (i.e., number of dimensions = number of basis molecules). However, as shown in 5.1 and 5.2, fitting to a number of dimensions similar to the number of molecules leads to large approximation errors from

overfitting. Thus, we argue that the SCISSORS method is more faithful to the mathematics behind similarity coefficients, is more flexible by allowing approximation of non-Euclidean measures, and is more accurate because it adds the ability to avoid overfitting.

### Connections to Kernel PCA

Kernel principal components analysis (kernel PCA) is a nonlinear variant of principal components analysis that, given data in some input vector space, finds the principal components of the data in a different vector space known as the feature space [77, 78]. The dimensionality of this feature space is often very high (possibly infinite). The computation is achieved by the use of kernel functions, which map a pair of points in the input space to a real number that is interpretable as the inner product of the two points in the feature space, without requiring an explicit expansion of the points into the feature space.

In the Methods, we derived the SCISSORS algorithm from classical multidimensional scaling. The method used in SCISSORS to derive basis vectors is also closely related to kernel PCA (which is itself closely linked to multidimensional scaling [88]. In particular, by transforming chemical similarity Tanimoto values to inner products, we treat transformed chemical similarity functions as kernels that map molecules from some hypothetical "molecule space" into a feature space induced by the particular similarity function. Because the mathematical methods underlying SCISSORS are essentially identical to those of kernel PCA, several optimality properties of kernel PCA [77] carry over to SCISSORS. As was previously argued from the derivation from multidimensional scaling, a SCISSORS/kernel-PCA expansion of a molecule in k-dimensions of a chemical feature space has minimum mean-squared approximation error, compared to any other choice of k directions (e.g., as might be derived from a truncation of a Cholesky decomposition).

Furthermore, the k directions calculated from kernel PCA have minimal representation entropy. As a consequence, no other orthogonal basis transformation can reproduce the given inner product matrix with the same accuracy in fewer bits. This property provides a rigorous bound on the accuracy of vectors calculated by SCISSORS — no other method evaluating chemical similarity inner products by dot products between real vectors can achieve a better coverage of the variance in the training (basis) matrix with fewer bits than used by SCISSORS.

There are several key differences between SCISSORS and kernel PCA related to the treatment of the Gram matrix. First, following multidimensional scaling, we do not rescale the eigenvectors obtained in the diagonalization of the Gram matrix. Additionally, most commonly used chemical similarity measures, when transformed from Tanimotos to inner products, do not induce the type of kernel usually used with a kernel PCA approach (known as a Mercer kernel), as their Gram matrices usually have negative eigenvalues. More importantly, prior to diagonalizing the Gram matrix, we do not center the data to have zero mean. As a consequence, the first eigenvector reflects the mean value in the feature space [49]. As will be shown in the next section, this is key to partial interpretability of coordinates derived from SCISSORS.

### 5.4.2 Interpretation of chemical similarities

Besides its use in constructing vector approximations, the SCISSORS inference procedure also gives insight into the nature of the chemical space induced by a given similarity measure. In particular, for well-approximated measures for which a molecule-molecule inner product can be defined, we can interpret the meaning of the first vector coordinate and gain an understanding of the measure. Our example here is the Gaussian volume overlap measure used by ROCS.

ROCS defines its "shape Tanimoto" as equation 5.7, in which $O_{xy}$ represents the value of the overlap volume between molecules x and y, which have been rotated and translated to maximize their volume overlap.

$$T_{AB} = \frac{O_{AB}}{O_{AA} + O_{BB} - O_{AB}} \tag{5.7}$$

This equation has clear similarity to the conventional vector Tanimoto equation (5.1); by analogy, for ROCS we can treat the maximum overlap volume between a pair of molecules as the inner product between these two molecules. Recall that for a similarity measure to be well-approximated by SCISSORS, we require that the eigenvalue spectrum of the similarity measure falls off sufficiently rapidly, such that each successive dimension is significantly less important than the one preceding it.

Consider such a measure on molecules $A$ and $B$, and their vector approximations $\hat{A} =$

$[a_0 \cdots a_n]$ and $\hat{B} = [b_0 \cdots b_n]$. Because SCISSORS is able to approximate the measure well, it is true that $\langle A, B \rangle \approx \left\langle \hat{A}, \hat{B} \right\rangle$. The assumption that the measure is approximated well implies (by the discussion in section on generalizability) that the eigenvalue spectrum falls off rapidly. This in turns means that the first coordinate will be the dominant component of the inner product (since further coordinates are decreasingly important), or formally, that $\langle A, B \rangle \approx \left\langle \hat{A}, \hat{B} \right\rangle \approx a_0 b_0$. In the special case in which $A = B$ (the self-similarity of molecule A), $\langle A, A \rangle \approx a_0^2$.

For the ROCS similarity measure, this implies that the first coordinate of the vector for a given molecule, and therefore the first principal coordinate of the shape space induced by the measure, is approximately equal to the square root of the molecular volume. This is illustrated in Figure 5.8(a), which plots the first coordinate of many molecule vectors inferred by SCISSORS on the ROCS shape overlap quantity against their molecular volumes. The lines show that the data are well-fit by a square-root function multiplied by a constant that represents the relative importance of molecular volume to the whole similarity measure. This demonstrates that shape-based virtual screening is largely controlled by differences in molecular volume, which correlates very closely with molecular weight (Figure 5.8(b)).

As explained by analogy to kernel PCA, this first coordinate (which for ROCS is approximately equal to the square root of the molecular volume) reflects the mean location of the molecules in the feature space learned from the similarity measure. We do not know whether a similar chemically-interpretable understanding of the second and later eigenvectors (projections onto which are the molecular coordinates) exists. It has been demonstrated [7] that the eigenvectors calculated by kernel PCA converge, in the large-basis-limit, to eigenfunctions of a linear operator on the underlying kernel. These in a sense reflect a functional basis for the kernel (or similarity measure). However, in general, coordinates in a kernel feature space as calculated by kernel PCA are not required to have preimages in the input space [77]; making matters worse, in the SCISSORS case (similarity kernels operating on molecules), it is not even clear what the input space is! Therefore, we do not have a mathematical derivation for the chemical meaning behind particular coordinates. While it is possible that empirical examination of large molecule sets and their SCISSORS coordinates may uncover such interpretations, interpretability is not crucial to our target application (fast similarity estimation), and we have not carried out such an analysis.

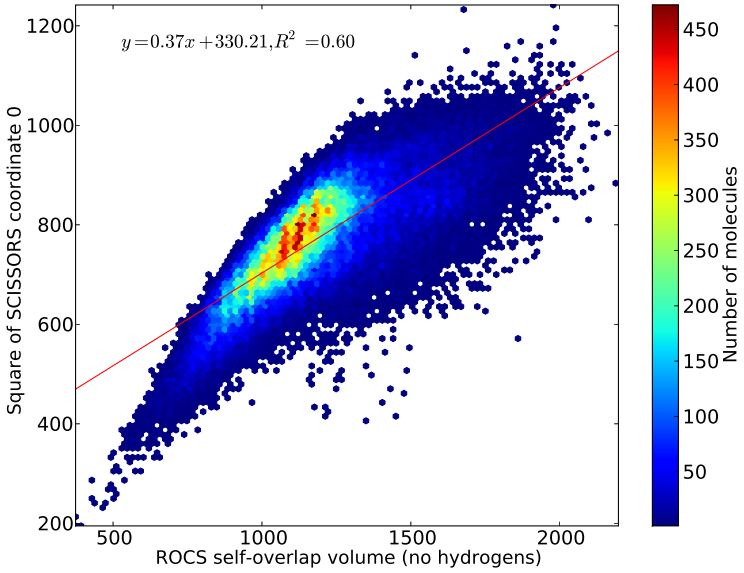


(a) Density plot of square of first coordinate of SCISSORS vectors inferred from ROCS shape overlap values versus ROCS self-overlap volume. Red line indicates optimal linear fit.

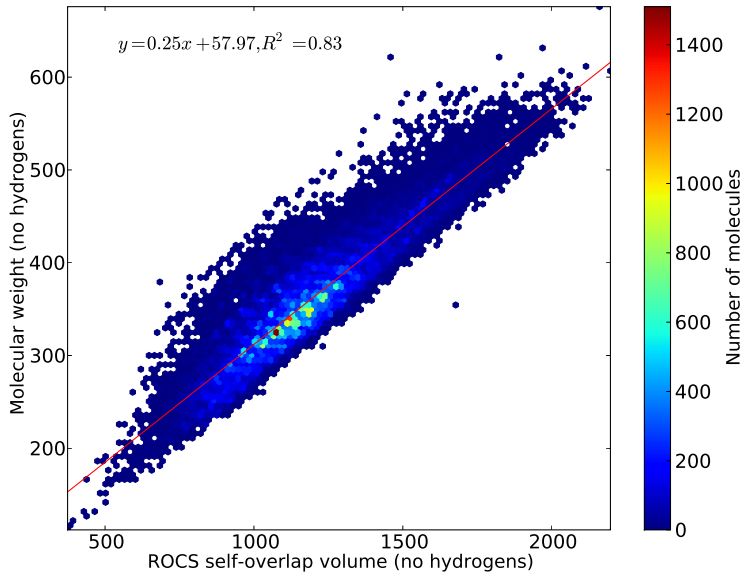


(b) Density plot of molecular self-volume from ROCS against molecular weight. Red line indicates optimal linear fit.

Figure 5.8: Interpretation of SCISSORS coordinates. All data from 128,371 Tanimotos computed on DUD test set; 500 random molecules from Maybridge used as basis.

### 5.4.3 Insights into chemical space

An interesting result of the SCISSORS analysis is that relatively few basis molecules (on the order of 500-1000) were sufficient to achieve accurate estimation of shape Tanimotos for compounds in Maybridge and DUD, and that the source of these molecules (Maybridge, Asinex, or Maybridge Fragment) made little difference for virtual screening. This finding is paralleled by previous results. Haigh et al. demonstrated that a reference shape set of 3,119 molecules was sufficient in their "shape fingerprints" approach to reproduce shape Tanimotos, and that these reference shapes were transferable across databases [38]. Fontaine et al. found that a database of 2,458 reference shapes was sufficient to cover the shape space of a one million compound single conformer data set in their "alignment recycling" approach [27]. Thus, our results corroborate past data showing that although chemical space is very large, the shape space of relevant druglike molecules may be fairly small, with only a few hundred to a few thousand basis shapes providing adequate coverage of the shape space.

### 5.4.4 Applications — Fast library screening and clustering with SCISSORS

The combination of learning vectors on a small basis set with fitting of new vectors in linear time using least-squares makes possible highly accelerated library screening. The target scenario for such an application involves screening based on a similarity measure that is expensive to calculate relative to the calculation of a low (order of $10^1 - 10^2$)-dimensional dot product. The SCISSORS-accelerated screening protocol follows these steps:

1. Select 500-1000 molecules at random to serve as a basis set for the library
2. Use SCISSORS to infer vectors for basis set by eigenvalue decomposition and for library by least squares
3. For each similarity search against the library, run slow similarity method for query molecule versus each basis molecule and learn vector
4. Screen query molecule against full library by SCISSORS vector Tanimoto

The advantage to the SCISSORS protocol is that after vectors have been inferred for a given library of molecules, each new screen only requires that the source similarity measure be run against the basis set, not the whole library. The majority of the comparisons can be done using the SCISSORS Tanimotos, which are thousands of times faster to evaluate.

In particular, clustering and other approaches that require the computation of a full $O(N^2)$ similarity matrix can be dramatically accelerated by SCISSORS. Assuming a library of size $N$ and a basis set of size $k$ ($k \ll N$), using SCISSORS to compute the Tanimoto similarities for the matrix requires only $O(kN)$ evaluations of the slow similarity measure, rather than $O(N^2)$. Since $k$ can be chosen as a fixed constant, SCISSORS is asymptotically faster in slow similarity evaluations than a straightforward similarity construction by a factor of $N/k$ - potentially many thousands of times. This, combined with the asymptotic reduction in storage space required to quickly retrieve a similarity matrix (discussed in the Results), demonstrates that SCISSORS enables huge reductions in computational cost for large-scale chemical matrix problems.

## 5.5 Conclusion

The heavy computational burden imposed by popular chemical similarity measures, combined with the growing size of chemical databases, necessitates faster techniques for similarity comparison to enable large-scale cheminformatics analyses. We have described SCISSORS, a generic method for rapid estimation of chemical similarities that is applicable to several popular similarity measures, including ones based on substructure comparison (LINGO) [85] and three-dimensional shape and chemical complementarity [33, 75]. SCISSORS is able to achieve high accuracy with an efficient precalculation procedure and relatively small molecular basis set. Given precalculated molecular vectors, our method achieves several thousandfold speedup relative to running the source similarity metric for ROCS. We have further described a method that allows construction of a molecular similarity matrix (an important intermediate step in several algorithms) with only a linear number of evaluations of the source similarity measure, rather than the quadratic number normally required.

There are several avenues for further exploration of SCISSORS and related methods.

In particular, it would be interesting to examine the performance of previously-described molecular shape basis sets [27, 38] as basis sets for SCISSORS. There is also scope for exploration of methods that can better capture the curvature of the feature spaces induced by certain similarity measures.

Our algorithm enables cheminformatics calculations to be performed with asymptotically lower costs, both in terms of computation (number of slow similarity evaluations) and storage (keeping molecule vectors on disk rather than full similarity matrices). As a consequence, we anticipate that SCISSORS will allow a new class of extreme-scale cheminformatics applications combining very large datasets with similarity measures formerly considered inaccessible for large compound collections.

## 5.6 Appendix: Detailed Methods

### 5.6.1 Molecular Databases and Preprocessing

The following databases were used

- Maybridge+BBP: 56841 of 56842 molecules from Maybridge Screening Collection (cromoglicic acid caused Omega to crash and was excluded) + 417 molecules from a blood-brain barrier penetration dataset [54]. Molecules from Maybridge were provided as 2-D SDF files; BBP molecules were provided as SMILES.
- Directory of Useful Decoys, release 2: 128,371 molecules provided as 3-D MOL2 files with embedded charges.
- Asinex Gold Collection: 233,795 molecules provided in 2-D SDF format.
- Maybridge Fragment Library: 473 molecules provided in 3-D MOL2 format with embedded charges.
- PubChem Assay #677 (Discovery of novel allosteric modulators of the M1 muscarinic receptor: Antagonist Confirmation Screen): 1,665 molecules provided in 2-D SDF format.

For standardization, all molecules (even if provided with 3-D geometry and charge information) were converted to 2-D uncharged OEBinary format using the OpenEye OEChem toolkit and then processed through the same pipeline. Molecules consisting of multiple disconnected chains (e.g., acids with counterions) were reduced to a single chemical chain using the function "OETheFunctionFormerlyKnownAsStripSalts" to keep only the largest single chain. Molecules containing atoms other H, C, N, O, F, Si, P, S, Cl, Br, and I were excluded, as these are the only atoms allowed in the MMFF94s force field used by OMEGA. Protonation, tautomer, and stereochemical state (other than invertible nitrogens) were maintained as given in the input data.

From the 2-D representation, the OpenEye Omega toolkit was used to build one 3-D conformer, using all default settings except for MaxConfGen=50 and MaxConfs=1. This representative conformer was used to assign charges, using the AM1-BCC charge model in the OpenEye OEProton toolkit. Final 3-D conformers were then built using Omega with the following parameters:

- Bondi van der Waals radii
- fromCT = False
- EnumNitrogen = True
- EnumRing = True
- BuildForceField = SearchForceField = mmff94s_Trunc
- EnergyRange = "5.0, 10.0, 15.0, 20.0, 25.0"
- MaxConfGen = 3000
- MaxConfRange = 50, 100, 200 (multi-conformer molecules only)
- MaxConfs = 1 (single-conformer molecules only)
- RangeIncrement = 3
- RMSRange = "0.5,0.75,1.0,1.5"

For the Maybridge+BBP dataset, both multi-conformer and single-conformer molecules were built; for all others, only single-conformer representations were used. These datasets were already in use for other ongoing drug discovery projects, and thus were not re-built for this study.

All molecule files used as input to ROCS, LINGO, ZAP, and the SCISSORS training routines were stored as 3-D OEBinary files.

### 5.6.2 Software versions

The Maybridge+BBP data set was prepared using OEChem 1.5.1 for file parsing, OEOmega 2.2.1 for conformer generation, and OEProton 1.2.1 for charge assignment. All other data sets were prepared using OEChem 1.6.1, OEOmega 2.3.0, and OEQuacPac (the renamed OEProton) 1.3.1.

ROCS shape and color similarities were calculated by the OpenEye OEShape toolkit, version 1.7.0. LINGO similarities were calculated using OEChem 1.6.1. ZAP ET similarities were calculated using OEZap 2.1.0.

Benchmarking of SCISSORS similarities was done using an implementation written in Python and C, using Python 2.5.2, Numpy 1.1.0, and GotoBLAS2 1.13. Most calculations were performed using an older implementation of SCISSORS written in pure Python and Numpy; performance benchmarking was done using a newer implementation of SCISSORS Tanimotos written in C using GotoBLAS2. C code was compiled using gcc 4.0.1.

### 5.6.3 Software settings for similarity calculations

ROCS shape and color similarities for all accuracy tests except the virtual screening test were calculated using the Analytic overlap method, the Implicit Mills-Dean color forcefield, with color optimization enabled, ignoring hydrogens, and using exact atomic radii (rather than coercing all radii to the carbon radius). For each pair of molecules, the best overlay was chosen from the set of all conformer pairs (for multiconformer matches) and ROCS starting positions by selecting the overlay with the highest Combo score. The shape and color Tanimoto values from this overlay were used as the representative Tanimoto values for that particular pair.

For virtual screening, ROCS was run on the DUD molecules with the Grid overlap method, ignoring hydrogens, and with no color force field (as only the shape Tanimoto was being approximated).

For the performance benchmark (in which we measured the time to construct a SCISSORS representation of a 20,480 molecule library), ROCS/OEShape was run in Analytic overlap mode with no color force field (shape only), and default settings otherwise.

LINGO similarities were calculated using the OELingoSim module in OEChem. Aromaticity (using OpenEye aromaticity model) and chirality were perceived on molecules from their 3-D structures; LINGO similarities were then calculated based on an isomeric canonical SMILES representation.

ZAP electrostatic Tanimotos were calculated using the OEET module in OEZap. First, molecules were overlaid into their optimal overlaid pose using ROCS using the same settings as for shape/color similarity. OEET's default settings for Tanimoto similarity were used to calculate the electrostatic similarity, based on the AM1-BCC charges calculated during molecule setup.

### 5.6.4 Performance benchmarking setup

Performance benchmarking for ROCS and SCISSORS was run on a Mac Pro with 2 x 3GHz Quad-Core Intel Xeon CPUs (Core 2 architecture) and 16GB of DDR2 667MHz fully-buffered memory, running OS X 10.5.8. Both the ROCS and SCISSORS benchmarking scripts were written in Python and executed on a 32-bit build of CPython 2.5.2. All benchmarks were conducted as single-CPU tests.

ROCS was called from within a Python script using the OpenEye OEShape toolkit and greater than 97% of the execution time was spent inside the OEBestOverlay.Overlay function (which calculates the optimal overlap).

SCISSORS operations other than Tanimoto calculations were performed using standard operations in Numpy 1.1.0, as downloaded in binary form from numpy.scipy.org. The C module for SCISSORS Tanimoto calculation was built against GotoBLAS2 1.13, using gcc 4.0.1, with the following performance-relevant compiler options: g++ -arch i386 -fno-strict-aliasing -Wno-long-double -no-cpp-precomp -fno-common -DNDEBUG -msse

-msse2 -msse3 -march=core2 -mfpmath=sse -O3. SCISSORS Tanimoto calculation times were computed over 4,096 x 262,144 Tanimotos, calculated in blocks of 4,096 x 32,768, in 64 dimensions.

# Chapter 6

# Error Bounds on SCISSORS

## Abstract

The SCISSORS method for approximating chemical similarities has shown excellent empirical performance on a number of real-world chemical data sets, but lacks theoretically-proven bounds on its worst-case error performance. The work in this chapter first proves reductions showing SCISSORS to be equivalent to two previous kernel methods: kernel principal components analysis and the rank-$k$ Nyström approximation of a Gram matrix. These reductions allow the use of generalization bounds on these techniques to show that the expected error in SCISSORS approximations of molecular similarity kernels is bounded in expected pairwise inner product error, in matrix 2-norm and Frobenius norm for full kernel matrix approximations, and in RMS deviation for approximated matrices.

## 6.1 Introduction

The SCISSORS method is a technique for accelerating chemical similarity search by transforming Tanimoto similarity scores to inner products, computing a metric embedding for a small "basis set" of molecules that optimally reconstructs the given inner products, and then projecting remaining non-basis "library" molecules into this vector space [40]. SCISSORS similarities are then computed as Tanimotos on these embedded vectors. Significant speedups can be achieved for certain similarity measures (those which are expensive to compute, and have highly concentrated eigenvalue spectra) for repeated queries into a static database: the work done to compute vector projections for each database molecule can be amortized easily across a large number of queries. In the original SCISSORS paper, Haque and Pande report that for a database of approx. 57,000 molecules, a basis set of 1,000 molecules and embedding dimension of 100 was sufficient to accurately reproduce the shape similarity over the whole database.

The embedding used in SCISSORS is computed by first calculating the pairwise inner product matrix $G$ between all pairs of basis molecules. $G$ is then decomposed into eigenvectors $V$ and eigenvalues along the diagonal of a matrix $D$; the vector embedding for the basis molecules lie along the rows of matrix $B$ in the following equation:

$$\begin{aligned} G = BB^T = VDV^T = VD^{1/2}D^{1/2}V^T \\ \therefore B = VD^{1/2} \end{aligned} \tag{6.1}$$

The rank of the approximation can be controlled by ordering the eigenvalues in order of decreasing value, setting all eigenvalues below a certain desired count to zero, and truncating these zero dimensions in the resulting vectors.

While SCISSORS appears to have good empirical performance, it lacks theoretically-rigorous guarantees on its approximation. In this chapter, theoretical bounds on the SCISSORS approximation error will be derived by reducing SCISSORS to previously-described kernel methods from machine learning.

## 6.2 Preliminaries

### 6.2.1 SCISSORS as a kernel method

The key insight of the SCISSORS technique is that molecular similarity measures, after appropriate transformation, can be treated as kernel functions taking pairs of molecules to scalar values that can be interpreted as inner products. The SCISSORS pipeline can be roughly segmented into the following operations:

1. Convert Tanimotos to inner products (basis-vs-basis or library-vs-basis)
2. Compute a vector embedding on the inner products (by eigendecomposition or least-squares)
3. Compute vector-space inner products (standard dot product in $\Re^N$)
4. Convert vector-space inner products to Tanimotos using standard vector Tanimoto equation

Steps 1 and 4 in this pipeline involve ratios of inner products (or kernel values), and as such, introduce nonlinearities into the analysis. However, if one assumes that exact kernel values are given or easily obtained (as demonstrated for the shape overlap volume in [40]), and that the goal is to directly approximate these kernel values rather than the Tanimoto, then SCISSORS directly resembles a typical kernel method. Therefore, in this chapter, we will consider only the error in these inner-product-space stages, rather than error introduced at the Tanimoto stages. Accordingly, we replace the notion of a "molecular similarity function" with that of a "molecular similarity kernel", which can be thought of as the composition of a similarity function with the Tanimoto-to-inner-product operation from SCISSORS.

The following lemma will be useful in demonstrating the equivalence of SCISSORS to various other kernel methods.

**Lemma 6.1** (SCISSORS library vectors are projections onto eigenvectors of the basis inner product matrix)**.** *Given an $N \times N$ SCISSORS basis inner product matrix (that is, a similarity matrix post-Tanimoto-to-inner-product conversion) $K$. Let the eigenvalues (resp. eigenvectors) of $K$ be denoted $\lambda_i$ and $V_i$, with eigenvalues sorted in descending order of*

*value. Let the matrix of all eigenvectors be named* $V = [V_1 V_2 \cdots V_N]$. *The SCISSORS vector* $w$ *for a new molecule with library-vs-basis inner product vector* $L$, *in* $d$ *dimensions, is defined by the expression:*

$$w = \begin{bmatrix} \lambda_1^{-1/2} \langle V_1, L \rangle \\ \lambda_2^{-1/2} \langle V_2, L \rangle \\ \vdots \\ \lambda_d^{-1/2} \langle V_d, L \rangle \end{bmatrix} \tag{6.2}$$

*Proof.* Let the result of equation 6.1 be denoted $B$, the full-dimension basis vector matrix. Let the restriction of $B$ to $d$ dimensions be denoted $B'$; this can be defined by $B' = VD^{1/2}R$ with the restriction matrix $R$ defined by:

$$R = \begin{bmatrix} I_{d \times d} \\ 0_{N-d \times d} \end{bmatrix}$$

Where $I_{d \times d}$ is the $d \times d$ identity matrix, and $0$ is a zero matrix of appropriate dimensions. The desired library vector $w$ is then defined by the least-squares solution to the equation $B'w = L$. This can be solved analytically:

$$\begin{aligned} w &= \left(B'^T B'\right)^{-1} B'^T L \\ &= \left(R^T D^{1/2} V^T V D^{1/2} R\right)^{-1} R^T D^{1/2} V^T L \\ &= \left(R^T D R\right)^{-1} R^T D^{1/2} V^T L \end{aligned}$$

Solve for each part of this separately (with $D_d$ and $D_{N-d}$ denoting corresponding blocks of matrix $D$:

$$\begin{aligned} R^T D R &= \begin{bmatrix} I & 0 \end{bmatrix} \begin{bmatrix} D_d & 0 \\ 0 & D_{N-d} \end{bmatrix} \begin{bmatrix} I \\ 0 \end{bmatrix} \\ &= D_d = \operatorname{diag}\left([\lambda_1, \lambda_2, \cdots, \lambda_d]\right) \\ \therefore \left(R^T D R\right)^{-1} &= D_d^{-1} = \operatorname{diag}\left(\left[\lambda_1^{-1}, \lambda_2^{-1}, \cdots, \lambda_d^{-1}\right]\right) \end{aligned}$$

$$
\begin{aligned}
w &= D_d^{-1} \begin{bmatrix} I_d & 0 \end{bmatrix} \begin{bmatrix} D_d^{1/2} & 0 \\ 0 & D_{N-d}^{1/2} \end{bmatrix} V^T L \\
&= D_d^{-1} \begin{bmatrix} D_d^{1/2} & 0 \end{bmatrix} V^T L \\
&= \begin{bmatrix} D_d^{-1/2} & 0 \end{bmatrix} V^T L \\
w &= \begin{bmatrix} \lambda_1^{-1/2} \langle V_1, L \rangle \\ \lambda_2^{-1/2} \langle V_2, L \rangle \\ \vdots \\ \lambda_d^{-1/2} \langle V_d, L \rangle \end{bmatrix}
\end{aligned}
$$

□

### 6.2.2 Assumptions

The analysis in this chapter will rest on the following assumptions:

- SCISSORS is given molecular similarity kernel values, not Tanimotos, to analyze. While the conversion from Tanimoto to inner product will introduce distortion (particularly if different molecules $x$ and $y$ have very different values of $\kappa(x, x)$ and $\kappa(y, y)$ for similarity kernel $\kappa$, we will not consider this distortion here.

- It is assumed that the similarity kernel $\kappa$ is symmetric positive semidefinite (SPSD). Similarity kernels that are not SPSD are not Mercer kernels and some proofs will fail in the presence of negative kernel eigenvalues. However, given non-SPSD $\kappa$, the results of this chapter can still be applied to a modified kernel $\kappa'$, the nearest SPSD approximation to $\kappa$. If $\kappa$ is symmetric but indefinite, then certain divergence terms can be easily calculated between the kernel matrices $K$ and $K'$ induced by $\kappa$ and $\kappa'$:

  - $||K - K'||_2$ = absolute value of the negative eigenvalue with largest magnitude
  - $||K - K'||_F$ = $\sum \lambda_{<0}^2$, where $\lambda_{<0}$ are the negative eigenvalues

- It is assumed that kernel values are exactly computable. In particular, the case in which kernel values themselves are subject to noise or inexactitude is not considered here. However, the following chapter does treat this case.

Under these assumptions, it is possible to bound the additional error made by SCISSORS in choosing a small random basis rather than using the eigendecomposition of the full kernel matrix over the entire library. Two different types of bounds will be shown in this chapter, arising from reductions to two different kernel methods: kernel principal components analysis, and the rank-$k$ Nyström approximation.

## 6.3 Reduction of SCISSORS to Kernel PCA

### 6.3.1 Overview of Kernel PCA

Kernel principal components analysis [77, 78] is a generalization of traditional principal components analysis from the data space to a feature space defined by a Mercer kernel function $\kappa$. Given a sample of $N$ data points, kernel PCA computes up to $N$ directions of maximum variance of the data, in the kernel's feature space. Points can then be projected into this $N$-dimensional subspace by a projection of their kernel values against the original (training) data points; thus, kernel PCA can be considered to perform a metric embedding of data points into a subspace of the feature space defined by a given kernel.

Similar to traditional (linear) PCA, kernel PCA can be preceded by a centering step, in which the data are centered in feature space; this ensures that the data mean is not reflected in the recovered coordinates. However, the uncentered case has relevance to SCISSORS, so we now proceed to derive the kernel PCA algorithm without data centering (following the approach of Scholköpf [77]).

### 6.3.2 Derivation of kernel PCA

Given a set of data points $x_i$, $i \in [1, \cdots, \ell]$, and a Mercer kernel $\kappa(x, y)$, defined by $\kappa(x, y) = \langle \Phi(x), \Phi(y) \rangle$ for some feature-space projection $\Phi$. Consider the feature covariance matrix $\bar{C}$:

$$\bar{C} = \frac{1}{\ell} \sum_{j=1}^{\ell} \Phi(x_j) \Phi(x_j)^T$$

Let the eigenvalues and eigenvectors of $\bar{C}$ be named $\lambda_k$ and $V_k$ respectively such that $\forall k \ \lambda V = \bar{C} V$. All such $V_i$ must lie in the span of $\Phi(x_1) \cdots \Phi(x_\ell)$. Thus the following system is equivalent:

$$\lambda(\Phi(x_k) \cdot V) = (\Phi(x_k) \cdot \bar{C} V) \ \forall k$$

and there exist $a_1 \cdots a_\ell$ such that

$$V = \sum_{i=1}^{\ell} a_i \Phi(x_i)$$

Defining matrix $K_{ij} = \langle \Phi(x_i), \Phi(x_j) \rangle$ and vector $\alpha = [a_1 \cdots a_n]^T$ we get $\ell \lambda K \alpha = K^2 \alpha$, so we solve the eigenvalue problem $\ell \lambda \alpha = K \alpha$. Solutions $\lambda_k, \alpha^k$ correspond to eigenvalues/vectors of the kernel matrix.

We normalize the resulting solutions by requiring that the feature-space eigenvectors ($V_k$) be unit magnitude. This implies:

$$\sum_{i=1}^{\ell} \sum_{j=1}^{\ell} a_i^k a_j^k \langle \Phi(x_i), \Phi(x_j) \rangle = \left\langle \alpha^k, K \alpha^k \right\rangle = \lambda_k \left\langle \alpha^k, \alpha^k \right\rangle = 1$$

We can compute the projection of a new data point $x$ onto the feature-space correlation matrix eigenvectors $V_k$ by:

$$\langle V_k, \Phi(x) \rangle = \sum_{i=1}^{\ell} a_i^k \langle \Phi(x_i), \Phi(x) \rangle$$

So for $d$ eigenvectors, the projected KPCA coordinate vector $w$ is:

$$w = KPCA\{x\} = \begin{bmatrix} \sum_i a_i^1 \langle \Phi(x_i), \Phi(x) \rangle \\ \sum_i a_i^2 \langle \Phi(x_i), \Phi(x) \rangle \\ \vdots \\ \sum_i a_i^d \langle \Phi(x_i), \Phi(x) \rangle \end{bmatrix}$$

Equivalently:

$$\begin{aligned} L &= [\langle \Phi(x_1), \Phi(x) \rangle, \cdots, \langle \Phi(x_\ell), \Phi(x) \rangle]^T \\ w = KPCA\{x\} &= [\langle \alpha^1, L \rangle, \cdots, \langle \alpha^d, L \rangle]^T \end{aligned}$$

### 6.3.3 Reduction Proof

We now demonstrate that SCISSORS is equivalent to kernel PCA performed without data centering.

As proven in Lemma 6.1, the SCISSORS vector $w$ corresponding to a library molecule is defined by weighted inner products between the eigenvectors of the kernel matrix and the library-versus-basis inner product vector $L$. Define new vectors $V_i' = \lambda_i^{-1/2} V_i$. Recall that the kernel matrix and vector L are already identical between methods, and both $V_i'$ and $\alpha_i$ are defined to be eigenvectors of the kernel matrix. To prove equivalence, all that is left to prove is that the SCISSORS projection vectors $V_i'$ have the same normalization as the KPCA $\alpha^i$; KPCA requires $\lambda_k \langle \alpha^k, \alpha^k \rangle = 1$.

*Proof.* We hypothesize that $V_k' = \alpha^k$. Then:

$$\begin{aligned} \lambda_k \langle V_k', V_k' \rangle &= \lambda_k \left\langle \lambda_k^{-1/2} V_k, \lambda_k^{-1/2} V_k \right\rangle \\ &= \lambda_k \lambda_k^{-1} \langle V_k, V_k \rangle \\ &= 1 \end{aligned}$$

□

## 6.4 Reduction of SCISSORS to the Nyström Rank-$k$ Approximation

### 6.4.1 Overview of the Nyström Method

In many large-scale machine learning methods, the computation and eigendecomposition of very-large scale kernel matrices is a bottleneck, as the time complexity of eigendecomposition scales as O($N^3$). Williams and Seeger introduced a method, based on the Nyström approximation from integral equation theory, to compute a low-rank approximation to a large kernel matrix, based on computing approximate eigenvectors for the entire matrix based on a random sample of a small number of points [87]. Precisely, using notation from Drineas et al. [24], given an $n \times n$ kernel matrix $K$, a desired rank $k$, and a number of basis elements $\ell$, the Nyström approximation computes $\tilde{K}_k$, a rank-$k$ approximation to $K$ by the following procedure:

**Algorithm Sketch 6.1** (Nyström approximation)**.** Given a kernel matrix $K \in \mathbb{R}^{n \times n}$, choose $\ell$ columns (equivalently, $\ell$ basis/landmark input points) $[b_1, b_2, \cdots, b_\ell]$ to obtain matrices $C$ and $W$:

$$C = \begin{bmatrix} K_{1b_1} & K_{1b_2} & \cdots & K_{1b_\ell} \\ K_{2b_1} & K_{2b_2} & \cdots & K_{2b_\ell} \\ \vdots & \vdots & \ddots & \vdots \\ K_{nb_1} & K_{nb_2} & \cdots & K_{nb_\ell} \end{bmatrix}$$

$$W = \begin{bmatrix} K_{b_1b_1} & K_{b_1b_2} & \cdots & K_{b_1b_\ell} \\ K_{b_2b_1} & K_{b_2b_2} & \cdots & K_{b_2b_\ell} \\ \vdots & \vdots & \ddots & \vdots \\ K_{b_\ell b_1} & K_{b_\ell b_2} & \cdots & K_{b_\ell b_\ell} \end{bmatrix}$$

Let $W_k$ be the best rank-k approximation to matrix $W$ and $W_k^+$ be the Moore-Penrose

pseudoinverse of $W_k$. Then the rank-$k$ Nyström approximation to matrix $K$ is defined by:

$$\tilde{K_k} = CW_k^+ C^T$$

### 6.4.2 Preliminaries

Consider a SCISSORS computation of full pairwise similarity over some large set of molecules $\mathcal{M}$. Partition this set, by random selection without replacement, into a basis set $\mathcal{B}$ and a library set $\mathcal{L}$. Then, the matrix $W$ in Algorithm 6.1 corresponds to the SCISSORS basis inner-product matrix on $\mathcal{B}$; similarly, $C$ is an aggregation of transposed library-vs-basis inner-product vectors. To prove the equivalence of SCISSORS and the Nyström method, we will demonstrate that the inner-product matrix computed by the SCISSORS-approximated vectors is identical to that computed by the Nyström method. It is sufficient to show (by Lemma 6.1) that $CW_k^+ C^T$, the Nyström-approximated Gram matrix, factorizes as $S_k S_k^T$ where:

$$S_k^T = D_k^{1/2} \begin{bmatrix} V_1^T \\ V_2^T \\ \vdots \\ V_k^T \end{bmatrix} C^T \tag{6.3}$$

$S_k$ is the matrix with library (and basis) vectors along the rows, so $S_k S_k^T$ is the SCISSORS-approximated Gram matrix. The following lemma is helpful for the proof:

**Lemma 6.2** (The pseudoinverse of $W_k$)**.** *$W_k^+ = \bar{V} D_k^{-1} \bar{V}^T$, where $\bar{V} = [V_1 V_2 \cdots V_k]$, the matrix formed from the first $k$ columns of the basis matrix eigenvectors, and $D_k^{-1} = diag[\lambda_1^{-1}, \lambda_2^{-1}, \cdots, \lambda_k^{-1}]$, the diagonal matrix of the reciprocals of the first $k$ eigenvalues of the basis matrix.*

*Proof.* The Moore-Penrose pseudoinverse of matrix $A$ is defined to be a matrix $X$ of

dimension equal to that of $A^T$ such that the following conditions hold:

$$\begin{aligned} AXA &= A \\ XAX &= X \\ AX &\text{ is Hermitian} \\ XA &\text{ is Hermitian} \end{aligned}$$

Given that the matrix of basis row vectors in $k$ dimensions is defined by:

$$B = \bar{V} D_k^{1/2} = \left[ V_1 \; V_2 \; \cdots \; V_k \right] \text{diag} \left[ \lambda_1^{1/2}, \lambda_2^{1/2}, \cdots, \lambda_k^{1/2} \right]$$

Then $W_k = BB^T = \bar{V} D_k^{1/2} D_k^{1/2} \bar{V}^T = \bar{V} D_k \bar{V}^T$. Define $X = \bar{V} D_k^{-1} \bar{V}^T$. Let $U = \bar{V}$ and $E = D_k$; note that columns of $U$ are orthogonal and that all matrices are real, so that Hermitian can be interpreted as symmetric. Then:

$$\begin{aligned} XW_kX &= UE^{-1}U^TUEU^TUE^{-1}U^T \\ &= UE^{-1}EE^{-1}U^T \\ &= UE^{-1}U^T \\ &= X \\ W_kXW_k &= UEU^TUE^{-1}U^TUEU^T \\ &= UEE^{-1}EU^T \\ &= UEU^T \\ &= W_k \\ XW_k &= UE^{-1}U^TUEU^T \\ &= UU^T = \left(UU^T\right)^T = (XW_k)^T \\ W_kX &= UEU^TUE^{-1}U^T \\ &= UU^T = \left(UU^T\right)^T = (W_kX)^T \end{aligned}$$

Thus, the matrix $X = \bar{V} D_k^{-1} \bar{V}^T$ satisfies all the Moore-Penrose properties and can be used as the value of $W_k^+$. □

### 6.4.3 Final Reduction

We must show that $CW_k^+C^T$ is equal to $S_kS_k^T$ where $S_k^T = D_k^{-1/2}\bar{V}^TC^T$.

*Proof.*

$$\begin{aligned} S_kS_k^T &= C\bar{V}D_k^{-1/2}D_k^{-1/2}\bar{V}^TC^T && \text{by definition of } S_k^T \\ &= C\left(\bar{V}D_k^{-1}\bar{V}^T\right)C^T \\ &= CW_k^+C^T && \text{by lemma 6.2} \end{aligned}$$

□

## 6.5 Expected error in individual inner products is bounded with high probability

### 6.5.1 Statement of the theorem

**Theorem 6.1** (Bounded expected inner product error)
*Given a chemical similarity kernel $\kappa$ defined over pairs of molecules from some distribution $D$, such that $\kappa(x,x) < R^2$ for some positive real constant $R$ for all $x \in D$. Construct a SCISSORS basis set from a random sample $S$ of $\ell$ molecules drawn uniformly at random from $D$. Denote by $\kappa_k^S$ the SCISSORS-approximated kernel of $k$ dimensions from basis set $S$. Then, with probability at least $(1-\delta)^2$, the expected error in SCISSORS approximation, over pairs of independently-chosen molecules $x, y \in D$, is bounded:*

$$\begin{aligned} 0 \leq \mathbb{E}\left[\kappa(x,y) - \kappa_k^S(x,y)\right] \leq \Bigg[ &\min_{1\leq d\leq k}\left(\frac{1}{\ell}\hat{\lambda}^{>d}(S) + \frac{1+\sqrt{d}}{\sqrt{\ell}}\sqrt{\frac{2}{\ell}\sum_{i=1}^{\ell}\kappa\left(s_i,s_i\right)^2}\right) \\ &+R^2\left(\frac{1}{4}+\sqrt{\frac{18}{\ell}\ln\left(\frac{2\ell}{\delta}\right)}\right)\Bigg] \end{aligned} \tag{6.4}$$

*Where $s_i$ are the basis molecules and $\hat{\lambda}^{>d}(S)$ is the sum of the eigenvalues of the basis matrix not used in SCISSORS:*

$$\hat{\lambda}^{>d}(S) = \sum_{i=k+1}^{\ell} \lambda_i$$

### 6.5.2 Proof Overview

The proof of Theorem 6.1 relies on a bound on the generalization error of kernel PCA projections due to Shawe-Taylor [79]. This theorem bounds the expected residual from projecting new data onto a sampled kernel PCA basis; we extend this proof to bound the expected error in inner products from projecting two points onto a kernel PCA basis. Then, the translation to SCISSORS follows trivially from the reduction of SCISSORS to kernel PCA.

The proof relies on the following definitions from the Shawe-Taylor work [79]:

- For a sample of $\ell$ vectors $S = s_1, s_2, \cdots, s_\ell$ and a kernel function $\kappa$, the sample correlation matrix $\mathbf{C(S)}$ is an $\ell \times \ell$ matrix with $C(S)_{ij} = \kappa(s_i, s_j)$.
- $\hat{\mathbf{V}}_\mathbf{k}$ is the space spanned by the first $k$ eigenvectors of $C(S)$.
- $\hat{\mathbf{V}}_\mathbf{k}^\mathbf{T}$ is the orthogonal complement to space $\hat{V}_k$.
- $\lambda_k$ is the $k$th process eigenvalue (true eigenvalue of the kernel operator $\kappa$, computed over the entire distribution generating our data).
- $\hat{\lambda}_\mathbf{k}$ is the $k$th empirical eigenvalue (i.e., the $k$th eigenvalue, in descending order of value, of the kernel matrix on $S$).
- $\lambda^{>\mathbf{k}}$ is the sum $\sum_{i>k} \lambda_k$, and similarly for $\hat{\lambda}^{>\mathbf{k}}$.
- The residual $\mathbf{P}^\mathbf{T}_{\hat{\mathbf{V}}_\mathbf{k}}(\mathbf{x})$ is the projection of $x$ onto the space $\hat{V}_k^T$.

We make use of the following theorem:

**Theorem 6.2** (Theorem 1 from [79])
*If we perform PCA in the feature space defined by kernel $\kappa$, then over random samples of points $S$ s.t. $|S| = \ell$ ($\ell$-samples), for all $1 \leq k \leq \ell$, if we project new data onto the space*

*$\hat{V}_k$, the expected squared residual is bounded by the following, with probability greater than $1-\delta$:*

$$\begin{aligned}\lambda^{>k} &\leq \mathbb{E}\left[\left|\left|P^T_{\hat{V}_k}\left(\Phi(x)\right)\right|\right|^2\right] \\ &\leq \min_{1\leq d\leq k}\left[\frac{1}{\ell}\hat{\lambda}^{>d}(S) + \frac{1+\sqrt{d}}{\sqrt{\ell}}\sqrt{\frac{2}{\ell}\sum_{i=1}^{\ell}\kappa\left(x_i,x_i\right)^2}\right] + R^2\sqrt{\frac{18}{\ell}\ln\left(\frac{2\ell}{\delta}\right)} \qquad (6.5)\end{aligned}$$

*Where the support of the distribution is in a ball of radius R in feature space.*

### 6.5.3 Proof of Theorem 6.1

Given two data vectors $\vec{x}$ and $\vec{y}$ chosen independently from a distribution $D$ and a kernel $\kappa$. By Mercer's theorem, there exists a function $\Phi$, the feature-space projection, such that $\langle\Phi(\vec{x}),\Phi(\vec{y})\rangle = \kappa(\vec{x},\vec{y})$. Let $X = \Phi(\vec{x})$ and $Y = \Phi(\vec{y})$. Assume $||X||^2, ||Y||^2 \leq R^2$ for some positive real constant $R$ (i.e., support of the feature-space distribution is bounded in a ball of radius $R$ around the origin). Given a random $\ell$-sample of vectors from $D$, construct the feature-space eigenvectors/eigenvalues from kernel PCA in $k$ dimensions. Define $X_\parallel$ to be the projection of $X$ onto $\hat{V}_k$, the eigenspace of chosen dimension from KPCA and $X_\perp$ to be the projection of $X$ onto $\hat{V}_k^T$, the orthogonal eigenspace. Likewise define $Y_\parallel$ and $Y_\perp$.

We would like a bound on the error of inner products in the parallel eigenspace (the KPCA space) with respect to the true inner product. We will compute this in the form $L \leq \mathbb{E}\left[X\cdot Y - X_\parallel\cdot Y_\parallel\right] \leq U$.

$$\begin{aligned}\kappa(\vec{x},\vec{y}) = X\cdot Y &= (X_\parallel + X_\perp)\cdot(Y_\parallel + Y_\perp) \\ &= X_\parallel\cdot Y_\parallel + X_\perp\cdot Y_\perp + X_\parallel\cdot Y_\perp + X_\perp\cdot Y_\parallel \\ &= X_\parallel\cdot Y_\parallel + X_\perp\cdot Y_\perp \\ &\therefore \mathbb{E}\left[X\cdot Y - X_\parallel\cdot Y_\parallel\right] = \mathbb{E}\left[X_\perp\cdot Y_\perp\right]\end{aligned}$$

With step 3 following because dot products between orthogonal eigenspaces are zero by definition. From this, we know that $L \geq 0$, since inner products are positive. It is possible to prove a tighter lower bound, but we are here interested in the upper bound of the error

only: $\mathbb{E}[X_\perp \cdot Y_\perp] \leq U$. This expression can further be bounded above:

$$\begin{aligned}\mathbb{E}\left[X_\perp \cdot X_\perp\right] &\leq \mathbb{E}\left[||X_\perp||||Y_\perp||\right] && \text{Cauchy-Schwarz inequality} \\ &= \mathbb{E}\left[||X_\perp||\right]\mathbb{E}\left[||Y_\perp||\right] + \text{Cov}\left(||X_\perp||, ||Y_\perp||\right) && (6.6)\end{aligned}$$

From Theorem 6.2, we know that for every $\delta \in [0, 1]$, sample size $\ell$, and feature-space radius bound $R$, there exists some constant $\alpha$ such that $E\left[X_\perp \cdot X_\perp\right] \leq \alpha$ and $E\left[Y_\perp \cdot Y_\perp\right] \leq \alpha$ with probability greater than $(1-\delta)^2$ (since we have two independent events each of probability $\geq (1-\delta)$). Using this fact we will now bound each term in equation 6.6.

**Bound on** $E\left[||X_\perp||\right]$

From Theorem 6.2, we know that $E\left[||X_\perp||^2\right] \leq \alpha$. By Jensen's inequality ($f(\mathbb{E}[x]) \leq \mathbb{E}[f(x)]$ for convex $f$):

$$\begin{aligned}\mathbb{E}^2\left[||X_\perp||\right] &\leq \mathbb{E}\left[||X_\perp||^2\right] \leq \alpha \\ \therefore \mathbb{E}\left[||X_\perp||\right] &\leq \sqrt{\alpha} && (6.7)\end{aligned}$$

**Bound on** $\text{Cov}\left(||X_\perp||, ||Y_\perp||\right)$

By the Cauchy-Schwarz inequality,

$$\text{Cov}\left(||X_\perp||, ||Y_\perp||\right) \leq \sqrt{\mathbb{V}\left[||X_\perp||\right]\mathbb{V}\left[||Y_\perp||\right]}$$

By symmetry, $\mathbb{V}\left[||X_\perp||\right] = \mathbb{V}\left[||Y_\perp||\right]$, so:

$$\text{Cov}\left(||X_\perp||, ||Y_\perp||\right) \leq \mathbb{V}\left[||X_\perp||\right] \tag{6.8}$$

Since $||X_\perp|| \in [0, R]$ by the assumption on support of feature distribution, $\mathbb{E}\left[||X_\perp||\right]$ must exist; let $E\left[||X_\perp||\right] = \gamma$ for some $\gamma$. Under this constraint, the variance of the distribution of $||X_\perp||$ is maximized by a scaled Bernoulli random variable $\nu$ with probability

density $f$:

$$\begin{aligned} f(x) &= \delta(x)\left(1-\frac{\gamma}{R}\right)+\delta(x-R)\frac{\gamma}{R} \\ \mathbb{E}[\nu] &= 0\times\left(1-\frac{\gamma}{R}\right)+R\times\frac{\gamma}{R}=\gamma \\ \mathbb{V}[\nu] &= \mathbb{E}\left[\nu^2\right]-\mathbb{E}^2[\nu] \\ &= \left(0+R^2\frac{\gamma}{R}\right)-\gamma^2 \\ &= \gamma\left(R-\gamma\right) \end{aligned}$$

This quadratic expression is maximized by $\gamma=\frac{R}{2}$, so:

$$\mathbb{V}\left[||X_\perp||\right] \leq \frac{R^2}{4} \tag{6.9}$$

**Final steps**

From Theorem 6.2: for every $\delta \in [0,1]$, sample size $\ell$, and feature-space radius bound $R$, there exists some constant $\alpha$ such that $E\left[X_\perp \cdot X_\perp\right] \leq \alpha$ and $E\left[Y_\perp \cdot Y_\perp\right] \leq \alpha$ with probability greater than $(1-\delta)^2$ for all $x$ and $y$ sampled independently from the distribution.

$$\begin{aligned} \mathbb{E}\left[X_\perp \cdot X_\perp\right] &\leq \mathbb{E}\left[||X_\perp||\right]\mathbb{E}\left[||Y_\perp||\right]+\text{Cov}\left(||X_\perp||,||Y_\perp||\right) && \text{Equation 6.6} \\ &\leq \alpha+\text{Cov}\left(||X_\perp||,||Y_\perp||\right) && \text{Equation 6.7} \\ &\leq \alpha+\mathbb{V}\left[||X_\perp||\right] && \text{Equation 6.8} \\ &\leq \alpha+\frac{R^2}{4} && \text{Equation 6.9} \end{aligned}$$

Therefore, by substitution from Theorem 6.2, with probability greater than $(1-\delta)^2$ on $\ell$-samples $S$, for any vectors $X$ and $Y$ independently sampled from D, the expected kernel

approximation error $\mathbb{E}\left[X \cdot Y - X_{\|} \cdot Y_{\|}\right]$ is bounded above by:

$$\begin{aligned}
&\alpha + \frac{R^2}{4} \\
&= \min_{1 \le d \le k} \left[ \frac{1}{\ell} \hat{\lambda}^{>d}(S) + \frac{1+\sqrt{d}}{\sqrt{\ell}} \sqrt{\frac{2}{\ell} \sum_{i=1}^{\ell} \kappa\left(x_i, x_i\right)^2} \right] + R^2 \sqrt{\frac{18}{\ell} \ln\left(\frac{2\ell}{\delta}\right)} + \frac{R^2}{4} \\
&= \min_{1 \le d \le k} \left[ \frac{1}{\ell} \hat{\lambda}^{>d}(S) + \frac{1+\sqrt{d}}{\sqrt{\ell}} \sqrt{\frac{2}{\ell} \sum_{i=1}^{\ell} \kappa\left(x_i, x_i\right)^2} \right] + R^2 \left( \frac{1}{4} + \sqrt{\frac{18}{\ell} \ln\left(\frac{2\ell}{\delta}\right)} \right)
\end{aligned}$$

Since computing approximate inner products using SCISSORS is equivalent to computing inner products using kernel PCA (section 6.3.3), this bound also holds for SCISSORS.

## 6.6 The error in SCISSORS-approximated Gram matrices is bounded in 2-norm, Frobenius norm, and RMS deviation

### 6.6.1 Statement of Theorems

Given a chemical similarity kernel $\kappa$ and a set of $n$ input molecules drawn from some probability distribution such that the $\kappa(x, x) < R^2$ for all molecules $x$. Let the true kernel matrix be denoted $K$ and the best possible rank-$k$ approximation to $K$ be denoted $K_k$. Compute a SCISSORS-approximated kernel matrix $\tilde{K}$ based on a size-$\ell$ uniform random sample of these vectors and a $k$-dimensional vector expansion. Then the following three theorems hold:

**Theorem 6.3** (Bounded error 2-norm)
*With probability at least $1 - \delta$, the error in the SCISSORS kernel matrix is worse than the lowest possible error from a rank $k$-approximated kernel matrix by at most a bounded amount in 2-norm:*

$$||K - \tilde{K}||_2 \leq ||K - K_k||_2 + \frac{2n}{\sqrt{\ell}} R^2 \left[ 1 + 2\sqrt{\frac{(n-\ell)^2}{(n-1/2)(n-\ell-1/2)} \log \frac{1}{\delta}} \right]$$

**Theorem 6.4** (Bounded error Frobenius norm)
*With probability at least $1 - \delta$, the error in the SCISSORS kernel matrix is worse than the lowest possible error from a rank $k$-approximated kernel matrix by at most a bounded amount in Frobenius norm:*

$$||K - \tilde{K}||_F \leq ||K - K_k||_F + \left[ \frac{64k}{\ell} \right]^{1/4} nR^2 \left[ 1 + 2\sqrt{\frac{(n-\ell)^2}{(n-1/2)(n-\ell-1/2)} \log \frac{1}{\delta}} \right]^{1/2}$$

**Theorem 6.5** (Bounded RMS error)
*With probability at least $1 - \delta$, the elementwise root-mean-square (RMS) error in the SCISSORS kernel matrix is worse than the lowest possible RMS error from a rank $k$-approximated kernel matrix by at most a bounded amount:*

$$\begin{aligned} \text{RMS}\{K - \tilde{K}\} \leq \text{RMS}\{K - K_k\} \\ + \left[ \frac{64k}{\ell} \right]^{1/4} R^2 \left[ 1 + 2\sqrt{\frac{(n-\ell)^2}{(n-1/2)(n-\ell-1/2)} \log \frac{1}{\delta}} \right]^{1/2} \end{aligned}$$

### 6.6.2 Proof Overview

The proofs of Theorems 6.3, 6.4, and 6.5 rely on the following theorem, due to Talwalkar [83] bounding the error of the rank-$k$ Nyström approximation of a Gram matrix:

**Theorem 6.6** (Theorem 5.2 from [83])
*Let $\tilde{K}$ denote the rank-k Nyström approximation of an $n \times n$ Gram matrix $K$ based on $\ell$ columns sampled uniformly at random without replacement from $K$, and $K_k$ the best rank-k approximation of $K$. Then, with probability at least 1 - $\delta$, the following inequalities hold for*

*any sample of size $\ell$:*

$$||K - \tilde{K}||_2 \leq ||K - K_k||_2 + \frac{2n}{\sqrt{\ell}} K_{max} \left[ 1 + \sqrt{\frac{n-\ell}{n-1/2} \frac{1}{\beta(\ell,n)} \log \frac{1}{\delta}} \frac{d^K_{max}}{K^{1/2}_{max}} \right]$$

$$||K - \tilde{K}||_F \leq ||K - K_k||_F + \left[ \frac{64k}{\ell} \right]^{1/4} nK_{max} \left[ 1 + \sqrt{\frac{n-\ell}{n-1/2} \frac{1}{\beta(\ell,n)} \log \frac{1}{\delta}} \frac{d^K_{max}}{K^{1/2}_{max}} \right]^{1/2}$$

*Where:*

- $K_{max} = \max_i K_{ii}$
- $d^K_{max}$ *is the maximum distance implied in* $K = \max_{i,j} \sqrt{K_{ii} + K_{jj} - K_{ij}}$
- $\beta(\ell, n) = 1 - (2 \max\{\ell, n - \ell\})^{-1}$.

For SCISSORS, we are particularly interested in the case in which $\ell \ll n$, so $\beta(\ell, n) = 1 - \frac{1}{2n-2\ell}$ and $1/\beta(\ell, n) = \frac{n-\ell}{n-\ell-1/2}$.

### 6.6.3 Proof of Theorems 6.3, 6.4, and 6.5

Given a kernel $\kappa$ and a distribution of input vectors such that their distribution in the feature space implied by $\kappa$ is $D$, and that the support of $D$ is contained within a ball of radius $R$ in feature space. Then, $K_{max}$ in the above equations is bounded above by $R^2$ and $d^K_{max} \leq 2R$. Note that this boundedness assumption holds for any finite sample of vectors from $D$, as we can construct an empirical distribution of vectors from the sample, which will be guaranteed to be of bounded radius.

Theorems 6.3 and 6.4 immediately follow from theorem 6.6 by applying the reduction of SCISSORS to the Nyström method, the definitions of $K_{max}$ and $d^K_{max}$, and the assumption above that $\ell \ll n$. Theorem 6.5 requires one additional step:

**Lemma 6.3.** *Given an $n \times n$ matrix $M$, the root-mean-square value of each element of M, RMS$\{M\}$ is related to the Frobenius norm of $M$, $||M||_F$ by the relationship:*

$$\text{RMS}\{M\} = \frac{1}{n} ||M||_F$$

*Proof.*

$$||M||_F = \sqrt{\sum_{i,j} M_{ij}}$$

$$\text{RMS}\{M\} = \sqrt{\frac{1}{n^2}\sum_{i,j} M_{ij}} = \frac{1}{n}\sqrt{\sum_{i,j} M_{ij}} = \frac{1}{n}||M||_F$$

□

Then Theorem 6.5 follows by multiplying each term of Theorem 6.4 by $1/n$.

## 6.7 Conclusions

Reduction to existing kernel methods makes it possible to prove rigorous probabilistic bounds on the approximation error made by SCISSORS under fairly mild restrictions on the input molecule distribution. However, because very few assumptions are made about the input distribution, the resulting bounds end up being very loose. For example, consider the added RMS error from basis-sampling (Theorem 6.5) under conditions resembling those in [40]: $n = 50,000$, $k = 100$, $l = 1,000$, with a desired confidence of $1 - e^{-3} \approx 95\%$:

$$\left[\frac{64 \cdot 100}{1000}\right]^{1/4} K_{max} \left[1 + 2\sqrt{\frac{(50000 - 1000)^2}{(50000 - 1/2)(50000 - 1000 - 1/2)} \log e^{-3}}\right]^{1/2} \approx 3K_{max}$$

So with 95% confidence, the RMS kernel error will be less than 3 times the maximum value of the kernel. This is clearly a very loose result; however, it is notable that this holds with no assumptions about the distribution of input molecules, except boundedness in the kernel values. The performance of SCISSORS on real-world data sets is significantly better than this worst-case estimate, indicating that the distribution of molecules in the similarity space considered is somehow friendly to sampling-based algorithms.

# Chapter 7

# The Impact of Noisy Kernel Computation on Low-Rank Kernel Approximation Methods


## Abstract

We use a perturbation approach to explore the impact of noisy or approximate computation of kernel functions on the spectral decomposition of the resulting kernel matrix. We apply these perturbation results to compute the elementwise error in low-rank noisy kernel approximation by the Nyström rank-$k$ method, and use these results to explain its experimental performance on noisy kernels.

## 7.1 Introduction

A broad range of methods in machine learning, including both supervised (e.g., support vector machines [13]) and unsupervised (e.g., kernel PCA [78]) learning algorithms, have been formulated to take advantage of the "kernel trick" to do learning in non-linear spaces. These kernel methods are constructed such that, in a linear formulation, they depend only on the inner products between pairs of input points, not on the points themselves. To kernelize them, the Euclidean inner product is replaced by a Mercer kernel function $K(\cdot, \cdot)$: a positive semidefinite function mapping pairs of input points to the non-negative reals. By Mercer's theorem, such a kernel function is equivalent to an inner product in some (possibly high- or infinite-dimensional) space. Thus, kernel methods can implicitly compute high-dimensional inner products from low-dimensional data. More interestingly, kernels can also be used to apply linear learning methods to non-vectorial data, such as text [56] or chemical structures [40]. While no natural inner product is defined on such data, kernels defined with domain-specific knowledge can substitute for an inner product to allow machine learning on such domains.

Much work has been done to examine the abilities of kernel methods to denoise corrupted input data [14], but less work [1] has focused on the issue of the kernel function itself being corrupted. Specifically, most denoising work to date has focused on the case of equation 7.1, in which input vectors $X$ and $Y$ are mixed with random noise sampled from some distribution. In this work we will consider the model of equation 7.2, in which the input data are intact, but the resulting value of the kernel is corrupt. This change has several interesting implications; in particular, the resultant function is no longer guaranteed to be positive semidefinite (and in general, will not be), thus making it an improper kernel.

$$K(X, Y) \to K(X + N_1, Y + N_2) \tag{7.1}$$

$$K(X, Y) \to K(X, Y) + N \tag{7.2}$$

We will first briefly review the sources of noise in computed kernels and then, using a perturbative approach, derive to first order the effect of kernel noise on the eigenvalues

and eigenvectors of the kernel matrix. The kernel method we consider in this paper is the Nyström rank-$k$ approximation of a full kernel matrix [24, 87]; we thus extend the derivation to a first-order expression for the error in a Nyström-approximated element. Finally, we show experimental results using kernels from chemical informatics.

## 7.2 Past work and the origins of noise

Most work to date has focused on kernels whose exact values are efficiently computable. In particular, Shawe-Taylor [79] and Talwalkar [83] have proven approximation bounds on the error incurred by low-rank approximations in kernel PCA and the Nyström rank-$k$ method; however, these bounds focus on the sampling error incurred by choosing a limited number of data elements from some distribution. A distinct question is the error incurred by the use of kernels whose exact evaluation is intractable, such that only approximate evaluations are available. These kernels are particularly of interest when modeling physical systems, where the relevant inner product in function space may be evaluated by numerical integration or require global non-convex optimization. Formally exact kernel evaluations also may become inexact when performed on a computer, due to limited precision introducing quantization noise and numerical error. Thus, examining of the impact of error and noise in kernel evaluations is of interest for practitioners of kernel-based learning methods.

An example of a noisy kernel is the molecular shape similarity function of Grant and Pickup [35], widely used in computational chemistry and drug design. This function computes an inner product between pair of chemical molecules represented by their excluded volume in three-dimensional space. Each molecule is represented as the union of a number of spherical isotropic Gaussians, each one centered on an atom. The two molecules are rotated and translated in space to maximize their volume overlap; the kernel value is then the overlap volume between the two. This overlap volume can formally be computed by numerical integration of equation 7.3, where each $\rho_{Ai}$ is the Gaussian on one atom. To ease computation, equation 7.3 is transformed to equation 7.4 by the principle of inclusion-exclusion; this summation is then truncated at second-order overlaps and used as the objective function for numerical local optimization [33, 39].

$$\rho_A(\mathbf{r}) = 1 - \prod_{i=1}^{N} (1 - \rho_{Ai}(\mathbf{r})) \tag{7.3}$$

$$\rho_A(\mathbf{r}) = \sum_i \rho_{Ai} - \sum_{i<j} \rho_{Ai}\rho_{Aj} + \sum_{i<j<k} \rho_{Ai}\rho_{Aj}\rho_{Ak} - \sum_{i<j<k<l} \rho_{Ai}\rho_{Aj}\rho_{Ak}\rho_{Al} + \cdots \tag{7.4}$$

The combination of a truncated objective function (an overestimator for the true objective) and local rather than global optimization contributes to error in the final output. As an example, we computed the overlay for 10,000 pairs of drug-like compounds using PAPER [39], an implementation of the Grant and Pickup method, with 4 and 12 starting points for the local optimizer (12 including the 4). We then scored each of these overlays with the true objective function (Equation 7.3); Figure 7.1 shows the distribution of improvement in scores from 4 to 12 starting points. Without noise, one would expect 12 starting points to dominate (improving the ability of the local optimizer to find the best overlay); however, the truncated objective function imposes inaccuracy with respect to the true objective, resembling Laplacian noise with standard deviation = 7.4. Despite this noise, shape similarity is widely used in the chemical informatics community and has been successfully used with spectral methods related to kernel PCA [40].

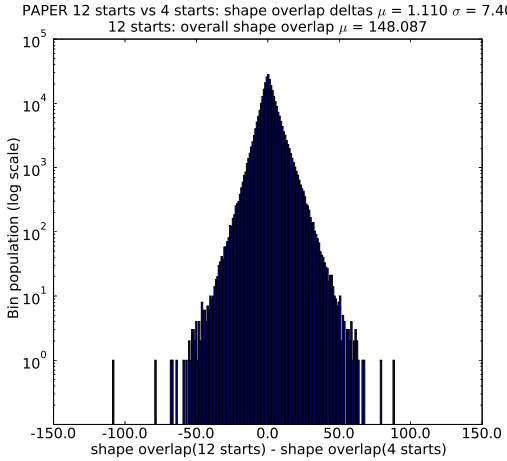


Figure 7.1: Histogram of the difference in kernel value for shape overlay computed using 12 vs. 4 starting positions. An exact kernel would show no spread away from zero difference. The computed standard deviation of 7.4 $\approx$ 5% of the mean kernel value.

Past methods have deliberately introduced structured noise into a kernel matrix to ease computation (e.g., by sparsification) [2]. Achlioptas [1] showed that low-rank kernel approximations are relatively resilient to Gaussian perturbations, and suggested that for kernel PCA [78] in particular, replacing complicated kernels with simpler unbiased estimators can work well. Achlioptas further suggests a rule, derived from random matrix theory, for deciding the optimal rank of a low-rank approximation in the presence of noise. We here present an alternative analysis, motivated by perturbative methods, that grants deeper insight into the mechanism by which noise affects kernel methods.

## 7.3 Perturbing the spectral decomposition

To analyze kernel PCA and Nyström approximation under noise, we must consider the spectral decomposition of the kernel matrix. Our main spectral perturbation results are summarized as Theorems 7.1 and 7.2.

**Theorem 7.1**

*If each element of an $D \times D$ kernel matrix $K_0$ is perturbed with iid Gaussian noise distributed as $N(0, \sigma^2)$, to first order, the perturbed eigenvalues $\lambda_i$, $i \in 1..D$, are related to the unperturbed eigenvalues $\lambda_{0i}$ by the relationship:*

$$\lambda_i = \lambda_{0i} + N\left(0, \sigma^2\right)$$

Note that, for sufficiently large kernel matrices, as a consequence of the Central Limit Theorem, the result of Theorem 7.1 will hold for any iid error terms of zero mean and bounded variance.

**Theorem 7.2**

*If each element of an $D \times D$ kernel matrix $K_0$ is perturbed with iid Gaussian noise distributed as $N(0, \sigma^2)$, to first order, the perturbed eigenvectors $\mathbf{x}_i$, $i \in 1..D$, are a random blend of*

*the unperturbed eigenvectors $\mathbf{x}_{0i}$ and are defined by the relationship:*

$$\mathbf{x}_i = \mathbf{x}_{0i} + \sum_{j \neq i}^{N} N\left(0, \frac{\sigma^2}{(\lambda_{0i} - \lambda_{0j})^2}\right) \mathbf{x}_j$$

*Where the $\lambda_{0i}$ are the unperturbed eigenvalues of $K_0$, sorted in descending order.*

Our perturbation analysis relies on the following fact of linear algebra [30]:

**Fact 1.** *Given solutions $\mathbf{x}_i$ and $\lambda_{0i}$ to the generalized eigenvalue problem $K_0\mathbf{x}_i = \lambda_{0i}M_0\mathbf{x}_i$, if we perturb matrices $K_0$ and $M_0$ to form new matrices $K$ and $M$:*

$$K = K_0 + [\delta K]$$
$$M = M_0 + [\delta M]$$

*For small perturbations $[\delta K]$ and $[\delta M]$, the solutions $\tilde{\mathbf{x}}_i$ and $\lambda_i$ to the perturbed eigenvalue problem $K\tilde{\mathbf{x}}_i = \lambda_i M\tilde{\mathbf{x}}_i$ are given, to first order, by the following expressions:*

$$\begin{aligned}
\lambda_i &= \lambda_{0i} + \mathbf{x}_i^T \left([\delta K] - \lambda_{0i}[\delta M]\right)\mathbf{x}_i \\
\tilde{\mathbf{x}_i} &= \mathbf{x}_i\left(1 - \frac{1}{2}\mathbf{x}_i^T[\delta M]\mathbf{x}_i\right) + \sum_{j \neq i}^{N} \frac{\mathbf{x}_j^T\left([\delta K] - \lambda_{0i}[\delta M]\right)\mathbf{x}_i}{\lambda_{0i} - \lambda_{0j}}\mathbf{x}_j
\end{aligned} \tag{7.5}$$

We are interested in the problem in which $M = I$, the identity matrix, and $K_0$ is the kernel matrix which we perturb with some random noise. Thus,

$$\begin{aligned}
M &= I \\
[\delta M] &= 0 \\
K_0\mathbf{x}_i &= \lambda_{0i}\mathbf{x}_i
\end{aligned} \tag{7.6}$$

*Proof of theorem 7.1.* We begin with the perturbation equation from Fact 1. Define for indexing convenience $\mathbf{x} = \mathbf{x}_i$ (this proof does not require the perturbed eigenvectors) and

$\delta_{ij} = [\delta K]_{ij}$, and consider a system of D eigenvectors:

$$\begin{aligned}
\lambda_i &= \lambda_{0i} + \mathbf{x}^T \left( [\delta K] - \lambda_{0i} [\delta M] \right) \mathbf{x} \\
&= \lambda_{0i} + \mathbf{x}^T \left( [\delta K] \right) \mathbf{x} \\
&= \lambda 0 i + \mathbf{x}^T \begin{bmatrix} \sum \delta_{0j} x_j \\ \sum \delta_{1j} x_j \\ \vdots \\ \sum \delta_{Dj} x_j \end{bmatrix} \\
\lambda_i &= \lambda_{0i} + \sum_{k=1}^{D} x_k \sum_{j=1}^{D} \delta_{kj} x_j
\end{aligned}$$

Assume that the elements of $[\delta K]$ are iid normal: $\delta_{ij} \sim N(\mu, \sigma^2)$ iid. Then, from linearity of independent normal random variables:

$$\begin{aligned}
\lambda_i &= \lambda_{0i} + \sum_{k=1}^{D} x_k \sum_{j=1}^{D} \delta_{kj} x_j \\
&= \lambda_{0i} + \sum_{k=1}^{D} x_k \sum_{j=1}^{D} N\left(\mu, \sigma^2\right) x_j \\
&= \lambda_{0i} + \sum_{k=1}^{D} x_k N\left( \mu \sum_{j=1}^{D} x_j, \sigma^2 \sum_{j=1}^{D} x_j^2 \right) \\
&= \lambda_{0i} + N\left( \mu \sum_{k} \sum_{j} x_k x_j, \sigma^2 \sum_{k} \sum_{j} x_k^2 x_j^2 \right) \\
&= \lambda_{0i} + N\left( \mu \sum_{k=j} x_k x_j \sum_{k \neq j} x_k x_j, \sigma^2 \sum_{k} x_k^2 \sum_{j} x_j^2 \right)
\end{aligned}$$

Further assume that our basis eigenvector $x$ has unit magnitude (orthonormal basis). Then:

$$\begin{aligned}\lambda_i &= \lambda_{0i} + N\left(\mu \sum_{k=j} x_k x_j \sum_{k\neq j} x_k x_j, \sigma^2 \sum_k x_k^2 \sum_j x_j^2\right) \\ &= \lambda_{0i} + N\left(\mu \sum_{k=j} x_k^2 \sum_{k\neq j} x_k x_j, \sigma^2 \sum_k x_k^2 \sum_k x_k^2\right) \\ &= \lambda_{0i} + N\left(\mu \sum_{k\neq j} x_k x_j, \sigma^2\right)\end{aligned}$$

If the kernel noise is assumed to be zero-mean normal ($\mu = 0$), then to first order we have that the perturbation from the true eigenvalue is also Gaussian:

$$\lambda_i = \lambda_{0i} + N\left(0, \sigma^2\right)$$

□

*Proof of theorem 7.2.* We want to compute the perturbed eigenvector $\tilde{\mathbf{x}}_i$ of matrix $K$ arising from eigenvector $\mathbf{x}_i$ of matrix $K_0$. Let $\lambda_{0i}$ be the (unperturbed) eigenvalue of $K_0$ corresponding to eigenvector $\mathbf{x}_i$. Define $\delta_{ij} \equiv [\delta K]_{ij}$. From Fact 1, the assumption that $[M] = I$, and $[\delta M] = 0$,

$$\begin{aligned}\tilde{\mathbf{x}}_i &= \mathbf{x}_i\left(1 - \frac{1}{2}\mathbf{x}_i^T\left[\delta M\right]\mathbf{x}_i\right) + \sum_{j\neq i} \frac{\mathbf{x}_j^T\left(\left[\delta K\right] - \lambda_{0i}\left[\delta M\right]\right)\mathbf{x}_i}{\lambda_{0i} - \lambda_{0j}}\mathbf{x}_j \\ &= \mathbf{x}_i + \sum_{j\neq i} \frac{\mathbf{x}_j^T\left[\delta K\right]\mathbf{x}_i}{\lambda_{0i} - \lambda_{0j}}\mathbf{x}_j \\ &= \mathbf{x}_i + \sum_{j\neq i} \frac{1}{\lambda_{0i} - \lambda_{0j}}\left(\mathbf{x}_j^T\left[\delta K\right]\mathbf{x}_i\right)\mathbf{x}_j \\ &= \mathbf{x}_i + \sum_{j\neq i} \frac{1}{\lambda_{0i} - \lambda_{0j}}\left(\mathbf{x}_j^T\begin{bmatrix}\sum_{p=1}^d \delta_{1p}x_{ip} \\ \sum_{p=1}^d \delta_{2p}x_{ip} \\ \vdots \\ \sum_{p=1}^d \delta_{Np}x_{ip}\end{bmatrix}\right)\mathbf{x}_j\end{aligned}$$

Assume $\delta_{ij} \equiv [\delta K]_{ij} \sim N(\mu, \sigma^2)$ iid. Then:

$$\begin{aligned}
\tilde{\mathbf{x}_i} &= \mathbf{x}_i + \sum_{j \neq i} \frac{1}{\lambda_{0i} - \lambda_{0j}} \left( \mathbf{x}_j^T \begin{bmatrix} N\left(\mu \sum_p x_{ip}, \sigma^2 \sum_p x_{ip}^2\right) \\ N\left(\mu \sum_p x_{ip}, \sigma^2 \sum_p x_{ip}^2\right) \\ \vdots \\ N\left(\mu \sum_p x_{ip}, \sigma^2 \sum_p x_{ip}^2\right) \end{bmatrix} \right) \mathbf{x}_j \\
&= \mathbf{x}_i + \sum_{j \neq i} \frac{1}{\lambda_{0i} - \lambda_{0j}} \left( \sum_{q=1}^{d} x_{jq} N\left(\mu \sum_p x_{ip}, \sigma^2 \sum_p x_{ip}^2\right) \right) \mathbf{x}_j \\
&= \mathbf{x}_i + \sum_{j \neq i} \frac{1}{\lambda_{0i} - \lambda_{0j}} N\left(\mu \sum_p x_{ip} \sum_q x_{jq}, \sigma^2 \sum_p x_{ip}^2 \sum_q x_{jq}^2\right) \mathbf{x}_j
\end{aligned}$$

Assume $\mu = 0$ and all unperturbed eigenvectors are unit magnitude.

$$\begin{aligned}
\tilde{\mathbf{x}_i} &= \mathbf{x}_i + \sum_{j \neq i} \frac{1}{\lambda_{0i} - \lambda_{0j}} N\left(0, \sigma^2\right) \mathbf{x}_j \\
&= \mathbf{x}_i + \sum_{j \neq i} N\left(0, \frac{\sigma^2}{\left(\lambda_{0i} - \lambda_{0j}\right)^2}\right) \mathbf{x}_j
\end{aligned}$$

□

## 7.4 First-order approximation to the kernel error

The results of Theorems 7.1 and 7.2 are sufficient to explain the noisy-kernel performance of kernel PCA, which is typically used to find principal directions of variation in feature space (the kernel matrix eigenvectors). Analyzing the Nyström approximation, however, requires one more step. Computing a rank-$d$ approximation $K_d$ of an $N \times N$ kernel matrix $K$ using the Nyström method is equivalent to the following procedure:

**Algorithm Sketch 7.1.** Computing a Nyström approximation via kernel PCA.

1. Select $B$ row/column indices $b_1, \cdots, b_B$ from $K_0$, and select the induced $B \times B$ submatrix $\beta$. These will be called "basis" rows, as the other elements will be projected onto linear combinations of these landmark points.

2. Compute the spectral decomposition of $\beta$, retaining the eigenvectors $V_i$ corresponding to the top $d$ eigenvalues $\lambda_i$

3. For every index $\ell_i$, define the vector $L_i = [K(b_1, \ell_i), \cdots, K(b_B, \ell_i)]^T$.

4. For each $L_i$, the projection of the data item corresponding to $L_i$ onto the Nyström subspace is $P_i = \begin{bmatrix} \lambda_1^{-1/2} \langle V_1, L_i \rangle \\ \lambda_2^{-1/2} \langle V_2, L_i \rangle \\ \vdots \\ \lambda_d^{-1/2} \langle V_1, L_i \rangle \end{bmatrix}$

5. Define matrix $P = [P_1 P_2 \cdots P_N]$. Then $K_d = P^T P$.

The above procedure is equivalent to carrying out kernel PCA without centering on a subset of the data in the kernel matrix, projecting the remainder of the data into a $d$-dimensional kernel PCA subspace, and re-computing the kernel matrix using the coordinates from kernel PCA. As a consequence, the relevant elementwise error quantity for the Nyström method is the error in inner products between the kernel PCA-projected vectors. Theorem 7.3 provides a first-order approximation of the elementwise error in low-rank-approximated inner products caused by a noisy kernel.

**Theorem 7.3**

*Given an $N \times N$ kernel matrix $K$ and a perturbed kernel matrix $\tilde{K}$ such that each element of $\tilde{K} - K$ is distributed as $N(0, \sigma^2)$ iid. Denote the rank-$d$ Nyström approximations of $K$ and $\tilde{K}$ as $K_d$ and $\tilde{K}_d$, respectively. Let $\ell_1$ and $\ell_2$ be two arbitrary data elements (row or column indices) on which $K$ was computed. Let $P_1$ and $P_2$ be the corresponding projections onto the Nyström subspace of $K$, and $\tilde{P}_1$ and $\tilde{P}_2$ the projections onto the Nyström subspace of $\tilde{K}$. Then, to first order, the error induced in the Nyström approximation by kernel noise is*

*equal to*

$$\left\langle \tilde{P}_1, \tilde{P}_2 \right\rangle - \langle P_1, P_2 \rangle = \sum_{i=1}^{d} \left[ \lambda_i^{-1} \left( \langle V_i, L_1 \rangle \left( N\left(0, \sigma^2\right) + N\left(0, \sigma^2 \sum_{i \neq j} \frac{\langle V_j, L_2 \rangle^2}{(\lambda_i - \lambda_j)^2} \right) \right) \right) \right.$$
$$+ \lambda_i^{-1} \left( \langle V_i, L_2 \rangle \left( N\left(0, \sigma^2\right) + N\left(0, \sigma^2 \sum_{i \neq j} \frac{\langle V_j, L_1 \rangle^2}{(\lambda_i - \lambda_j)^2} \right) \right) \right)$$
$$\left. + \frac{\xi}{\lambda_i(\lambda_i - \xi)} \langle V_i, L_1 \rangle \langle V_i, L_2 \rangle \right] \tag{7.7}$$

*With $\xi$ is distributed as $N(0, \sigma^2)$. $V_i$, $\lambda_i$, and $L_i$ are defined as in the Nyström procedure in Algorithm 7.1, computed on the noise-free kernel matrix $K$.*

*Proof.* We will call all data elements NOT chosen in step 1 of Algorithm 7.1 "library" elements, as opposed to the "basis" elements that were selected. From step 4 in Algorithm 7.1:

$$P_1 = \begin{bmatrix} \lambda_1^{-1/2} \langle V_1, L_1 \rangle \\ \lambda_2^{-1/2} \langle V_2, L_1 \rangle \\ \vdots \\ \lambda_d^{-1/2} \langle V_1, L_1 \rangle \end{bmatrix} \qquad P_2 = \begin{bmatrix} \lambda_1^{-1/2} \langle V_1, L_2 \rangle \\ \lambda_2^{-1/2} \langle V_2, L_2 \rangle \\ \vdots \\ \lambda_d^{-1/2} \langle V_1, L_2 \rangle \end{bmatrix} \tag{7.8}$$

Using Theorems 7.1 and 7.2, we can expand the definitions of $\tilde{P}_1$ and $\tilde{P}_2$ to reach the following formulas for the inner products:

$$
\begin{aligned}
\langle P_1, P_2 \rangle &= \sum_{i=1}^{d} \lambda_i^{-1/2} \lambda_i^{-1/2} \langle V_i, L_1 \rangle \langle V_i, L_2 \rangle \\
\left\langle \tilde{P}_1, \tilde{P}_2 \right\rangle &= \sum_{i=1}^{d} \tilde{\lambda}_i^{-1/2} \tilde{\lambda}_i^{-1/2} < \tilde{V}_i, \tilde{L}_1 >< \tilde{V}_i, \tilde{L}_2 > \\
&= \sum_{i=1}^{d} \Bigg[ \left(\lambda_i + N(0, \sigma^2)\right)^{-1} \times \\
&\quad \left\langle V_i + \sum_{j \neq i} N\left(0, \frac{\sigma^2}{(\lambda_i - \lambda_j)^2}\right) V_j, L_1 + N_{b\times 1}(0, \sigma^2) \right\rangle \times \\
&\quad \left\langle V_i + \sum_{j \neq i} N\left(0, \frac{\sigma^2}{(\lambda_i - \lambda_j)^2}\right) V_j, L_2 + N_{b\times 1}(0, \sigma^2) \right\rangle \Bigg]
\end{aligned}
$$

Where $N_{b\times 1}(\mu, \sigma^2)$ is a $b \times 1$-dimensional vector of iid normal random variables with mean $\mu$ and variance $\sigma^2$.

We will first consider each $< \tilde{V}_i, \tilde{L}_j >$ term in isolation; to be concrete, we will look at $< \tilde{V}_i, \tilde{L}_1 >$. This inner product can be broken into four terms:

1. $\langle V_i, L_1 \rangle$: this is the desired "clean" kernel term.

2. $< V_i, N_{b\times 1}(0, \sigma^2) >$. Arises from the noise in the library-vs-basis comparison.

$$
\begin{aligned}
< V_i, N_{b\times 1}(0, \sigma^2) > &= \sum_k V_{ik} N(0, \sigma^2) = N\left(0, \sum_k V_{ik}^2 \sigma^2\right) \\
&= N\left(0, \sigma^2\right) \text{ since } ||V_i|| = 1
\end{aligned} \tag{7.9}
$$

3. $\left\langle \sum_{i\neq j} N\left(0, \frac{\sigma^2}{(\lambda_i-\lambda_j)^2}\right) V_j, L_1 \right\rangle$. Arises from the noise in the basis projection eigenvectors.

$$\begin{aligned}\left\langle \sum_{i\neq j} N\left(0, \frac{\sigma^2}{(\lambda_i-\lambda_j)^2}\right) V_j, L_1 \right\rangle &= \sum_{i\neq j}\sum_k N\left(0, \frac{\sigma^2}{(\lambda_i-\lambda_j)^2}\right) V_{jk}L_{1k} \\ &= \sum_{i\neq j} N\left(0, \frac{\sigma^2}{(\lambda_i-\lambda_j)^2}\right) \sum_k V_{jk}L_{1k} \\ &= \sum_{i\neq j} N\left(0, \frac{\sigma^2}{(\lambda_i-\lambda_j)^2}\right) \langle V_j, L_1\rangle \\ &= N\left(0, \sigma^2 \sum_{i\neq j} \frac{\langle V_j, L_1\rangle^2}{(\lambda_i-\lambda_j)^2}\right) \end{aligned} \tag{7.10}$$

4. $\left\langle \sum_{j\neq i} N\left(0, \frac{\sigma^2}{(\lambda_i-\lambda_j)^2}\right) V_j, N_{b\times 1}(0,\sigma^2) \right\rangle$. Cross term from noise vs noise.

$$\begin{aligned}&\left\langle \sum_{j\neq i} N\left(0, \frac{\sigma^2}{(\lambda_i-\lambda_j)^2}\right) V_j, N_{b\times 1}(0,\sigma^2) \right\rangle \\ &= \sum_{j\neq i} N\left(0, \frac{\sigma^2}{(\lambda_i-\lambda_j)^2}\right) \sum_k V_{jk} N\left(0,\sigma^2\right) \\ &= \sum_{j\neq i} N\left(0, \frac{\sigma^2}{(\lambda_i-\lambda_j)^2}\right) N\left(0,\sigma^2\right) \text{ as in term \#2} \\ &= N\left(0,\sigma^2\right) N\left(0, \sigma^2 \sum_{j\neq i} \frac{1}{(\lambda_i-\lambda_j)^2}\right) \end{aligned} \tag{7.11}$$

Furthermore, we can factorize $\left(\lambda_i + N\left(0,\sigma^2\right)\right)^{-1}$ to separate out the noise:

$$\begin{aligned}\left(\lambda_i + N\left(0,\sigma^2\right)\right)^{-1} &= \lambda_i^{-1} + \Delta \\ \Delta &= \left(\lambda_i + N\left(0,\sigma^2\right)\right)^{-1} - \lambda_i^{-1} \\ &= \frac{\xi}{\lambda_i(\lambda_i - \xi)} \qquad\qquad \xi \sim N\left(0,\sigma^2\right) \end{aligned} \tag{7.12}$$

We are now in a position to compute, to first order, the deviation in library-vs-library

inner products that is due to noise. In this context, "to first order" means that we will ignore any terms that contain the product of two or more noise terms. This is motivated by the assumption that the noise is small, so the product of two noise terms is smaller; furthermore, the model from Theorems 7.1 and 7.2 is only accurate to first order. We want the following:

$$\text{Error} = \sum_{i=1}^{d} \lambda_i^{-1} \langle V_i, L_1 \rangle \langle V_i, L_2 \rangle - \sum_{i=1}^{d} \tilde{\lambda}_i^{-1} < \tilde{V}_i, \tilde{L}_1 >< \tilde{V}_i, \tilde{L}_2 > \tag{7.13}$$

Note that term 4 in the inner-product expansion detailed above can be dropped since it is second-order. After algebraic reduction to eliminate second- and higher-order terms, the above can be reduced to the following expression for the inner product error due to noise:

$$\begin{aligned}\left\langle \tilde{P}_1, \tilde{P}_2 \right\rangle - \langle P_1, P_2 \rangle = \sum_{i=1}^{d} \Bigg[ & \lambda_i^{-1} \left( \langle V_i, L_1 \rangle \left( N\left(0, \sigma^2\right) + N\left(0, \sigma^2 \sum_{i \neq j} \frac{\langle V_j, L_2 \rangle^2}{(\lambda_i - \lambda_j)^2} \right) \right) \right) \\ & + \lambda_i^{-1} \left( \langle V_i, L_2 \rangle \left( N\left(0, \sigma^2\right) + N\left(0, \sigma^2 \sum_{i \neq j} \frac{\langle V_j, L_1 \rangle^2}{(\lambda_i - \lambda_j)^2} \right) \right) \right) \\ & + \frac{\xi}{\lambda_i(\lambda_i - \xi)} \langle V_i, L_1 \rangle \langle V_i, L_2 \rangle \Bigg]\end{aligned} \tag{7.14}$$

With $\xi$ distributed as $N\left(0, \sigma^2\right)$. □

## 7.5 Experiments

Figure 7.2 shows the root-mean-square (RMS) error in using the Nyström method to approximate three different kernels: LINGO, a noisy version of LINGO in which iid $N(0, 1)$ noise has been added to each element, and the molecular shape overlap kernel. Each bar shows the RMS error as the two parameters of the Nyström method (size of "basis" set and dimensionality of expansion) are varied. Note that the RMS error is proportional to the Frobenius norm of the error matrix, by equation 7.15:

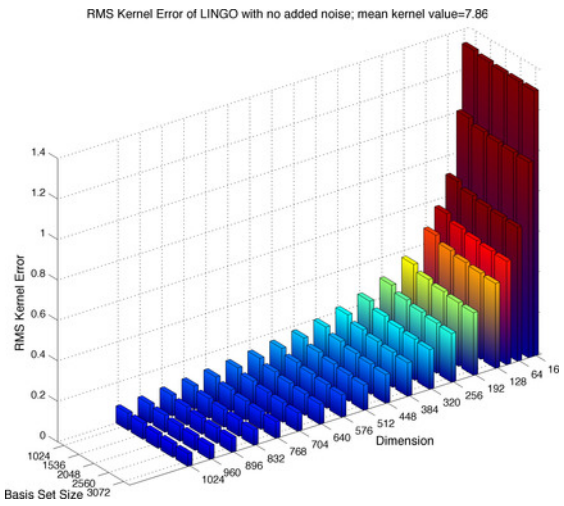


(a) Exact LINGO

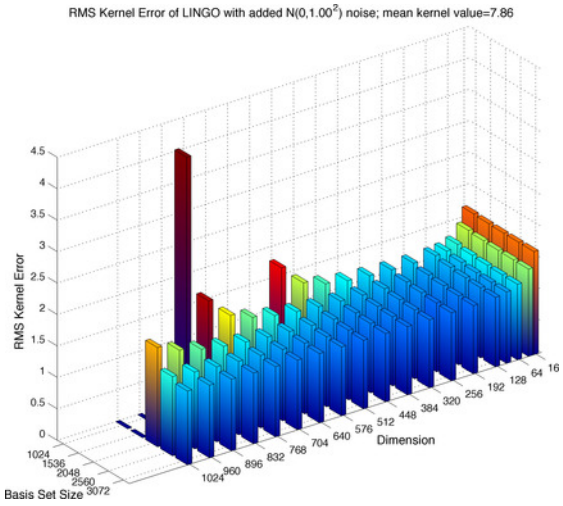


(b) LINGO with added N(0,1) noise

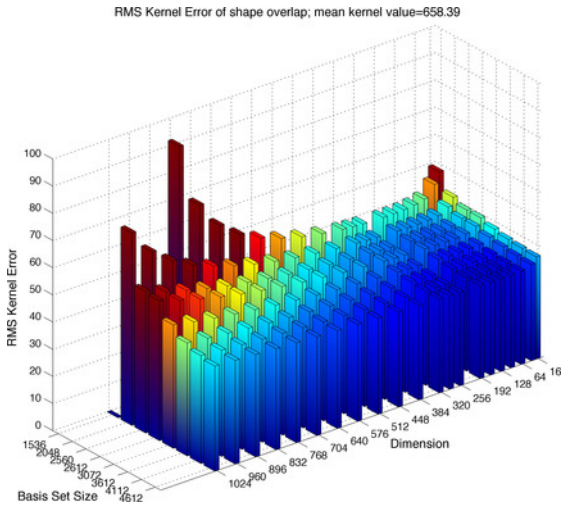


(c) Shape overlap

Figure 7.2: Effects of kernel noise on Nyström approximation

$$
\begin{aligned}
M &\in \Re^{m \times n} \\
||M||_F &= \sqrt{\sum_i \sum_j M_{ij}^2} \\
RMS(M) &= \sqrt{\frac{1}{mn} \sum_i \sum_j M_{ij}^2} \\
\therefore RMS(M) &= \frac{1}{\sqrt{mn}} ||M||_F
\end{aligned} \tag{7.15}
$$

The features of these plots can be explained by combining our results with the following bound on the error of the Nyström approximation, due to Talwalkar [83]:

**Theorem 7.4** (Theorem 5.2 of [83])
*Let $\tilde{K}$ denote the rank-k Nyström approximation of an $n \times n$ kernel matrix $K$ based on $\ell$ columns sampled uniformly at random without replacement from $K$, and $K_k$ the best rank-k approximation of $K$. Define $\beta(\ell, n) = 1 - (2\max\{\ell, n-\ell\})^{-1}$. If $\ell < n$, with probability at least 1 - $\delta$, the following inequality holds for any sample of size $\ell$:*

$$
||K - \tilde{K}||_F \leq ||K - K_k||_F + \left[\frac{64k}{\ell}\right]^{1/4} nK_{max} \left[1 + \sqrt{\frac{n-\ell}{n-1/2} \frac{1}{\beta(\ell,n)} \log\frac{1}{\delta}} \frac{d_{max}^K}{K_{max}^{1/2}}\right]^{1/2}
$$

*Where $K_{max}$ = $\max_i K_{ii}$ and $d_{max}^K$ is the maximum distance implied by the values of K, $d_{max}^K = \max_{ij} \sqrt{K_{ii} + K_{jj} - K_{ij}}$.*

The following fact about the Frobenius norm is also useful:

**Fact 2.** *Given a real symmetric matrix $M$ with singular values $\sigma_i$ (equivalently, eigenvalues $\lambda_i$:*

$$
||M||_F = \sqrt{\sum_{i,j} M_{ij}^2} = \sqrt{tr\,(M^T M)} = \sqrt{\sum_i \sigma_i^2} = \sqrt{\sum_i \lambda_i^2} \tag{7.16}
$$

The features of figure 7.2(a) are well-explained by Theorem 7.4. As we increase the rank of the approximation, we account for a larger fraction of the eigenspectrum of the

basis matrix, reducing the magnitude of the first term in theorem 7.4 by fact 2. Error also decreases (though to a smaller extent), as we increase the size of the basis set — this effect can be explained by a reduction in the magnitude of the second term in the theorem.

Once noise is added to the kernel functions, theorem 7.4 is no longer sufficient to explain the results. In particular, in both figures 7.2(b) and 7.2(c), adding dimensions only improves the quality of the approximation to a point, after which error rises dramatically (much faster than the fourth root of $k$, the rate suggested by the theorem). Furthermore, the minimum error hits a "noise floor", even after adding a large number of basis points. These features are well-explained by our perturbation results.

### 7.5.1 Noise floors

Figure 7.2(b), shows a noise floor around an RMS error of 1 for a kernel to which we have added $N(0, 1)$ noise to every evaluation. An intuitive explanation is that since the kernel evaluations are corrupted by zero-mean noise that is uncorrelated to the kernel value, the learning algorithm will be unable to predict this noise; we would thus expect an RMS error equal to the RMS value of the noise, which is $\sigma$.

For shape (figure 7.2(c)), the estimated noise ($\sigma \approx 7.4$, figure 7.1) is insufficient to explain the error floor of around 35. However, shape is not a true Mercer kernel: it has significant negative eigenvalues [53]. Using fact 2, it is possible to compute the RMS error due to ignoring these negative eigenvalues: approximately 27 in the large basis limit (at which eigenvalues should be best approximated [79]). Thus, the combination of the noise model and the negative eigenvalues is able to explain the Nyström error floor for shape.

### 7.5.2 Increasing error

The second unique feature of figures 7.2(b) and 7.2(c), versus figure 7.2(a), is that for both noisy kernels, the error eventually increases as more dimensions are used, and that this transition can be delayed by using more basis data. Our perturbation results help to explain this behavior.

Theorem 7.1 shows that the eigenvalues learned on a noisy kernel matrix will be equal to the true eigenvalues, plus the added noise. This implies that as the magnitude of an

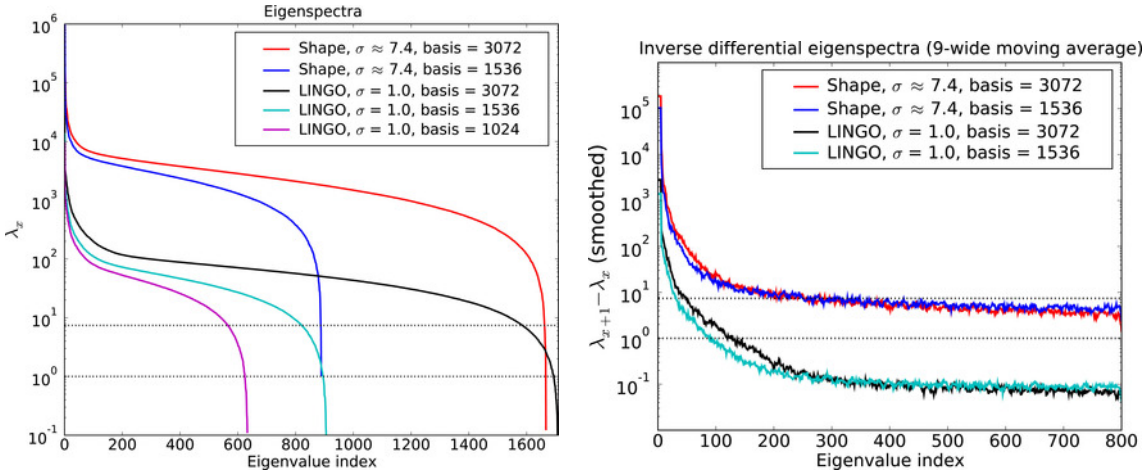


(a) Eigenspectra (b) Differential eigenspectra

Figure 7.3: Eigenspectra and spectral gaps for noisy LINGO and shape

eigenvalue approaches the standard deviation of the noise, the value of that eigenvalue will become unreliable. Figure 7.3(a) plots the eigenvalue spectra for the noisy LINGO and shape kernels for several basis set sizes, as well as the $\sigma$ values for each kernel. In all cases, a dramatic rise in error in figure 7.2 is seen when the approximation grows in dimension to use eigenvalues whose values are around the same value as $\sigma$.

Noise in the eigenvalues of the kernel matrix determines the point where error rises dramatically, but does not appear to correlate well with the exact location of the error minimum. However, errors in the learned eigenvectors do have a useful effect. According to theorem 7.2, the reliability of a learned eigenvector is determined by the separation between its eigenvalue and the other eigenvalues of the kernel matrix: in the presence of noise, learned eigenvectors are blends of the true eigenvector and surrounding eigenvectors, with variance in the blending factor inversely proportional to the square of the gap between the corresponding eigenvalues. Figure 7.3(b) plots a smoothed view of the first difference function of the eigenvalue spectra (that is, the gap between adjacent eigenvalues) for noisy LINGO and for shape, along with the respective noise $\sigma$ values.

For shape, the differential eigenspectrum is quantitatively predictive of the error minimum: the spectral gap intersects with $\sigma = 7.4$ between 200 and 300 dimensions, precisely where the error minimum is seen in figure 7.2(c). This holds true for both 1536 and 3072

basis molecules, consistent with the fact that the error minimum is at approximately the same dimensionality for both basis sets. For LINGO, the agreement is not quantitative, but is still explanatory. Figure 7.3(b) shows the spectral gap intersecting $\sigma = 1$ around 100 dimensions for a 1536-basis and 150 dimensions for a 3072-basis; in contrast, the minimum error is found at 192 and 256 dimensions, respectively. While the exact count of best dimensionality is not correct, the relative margin between the two is approximately correct. The spectral gap criterion predicts that the 3072-basis should be able to reliably estimate an extra 50 eigenvectors, which we confirm to within the resolution of our sampling (64 dimensions). We speculate that the reason extra vectors do not hurt for LINGO is that there are still useful directions to be learned in this regime. In figure 7.2(a), going beyond 256 dimensions still significantly reduces the RMS kernel error, so the true kernel has relevant information in these dimensions. It is possible that in the noisy case, there is a tradeoff being made between learning relevant directions in feature space, and noise in this learning, such that the net effect is almost zero until the eigenvalue noise threshold is passed. It is also possible that the true reason is not well explained by the first-order analysis, and requires higher-order analysis.

## 7.6 Practical Recommendations

In earlier work, Achlioptas [1] suggested, when approximating an $n \times d$ matrix $A$, to choose a rank $k$ such that:

$$||A - A_k||_2 \sim \sigma\sqrt{n} \tag{7.17}$$

Where $\sigma^2$ is the mean squared entry of the error matrix $A - A_k$. By using fact 2, this criterion can be converted into a form more relevant to the current work:

**Criterion 7.1** (Achlioptas criterion)**.** *When computing a low-rank approximation (equivalently, performing kernel PCA) on an $n \times n$ positive semidefinite kernel matrix $A$, let the eigenvalues of $A$ be named $\lambda_i$, $i = 1 \cdots n$, in descending order of value. A good choice of*

*approximation will retain the $k$ eigenvalues $\lambda_1$ through $\lambda_k$ such that:*

$$\lambda_{k+1} \approx \frac{1}{\sqrt{n}} \sqrt{\sum_{i=k+1}^{n} \lambda_i^2} \tag{7.18}$$

*Proof.* $\sigma$ from the original Achlioptas criterion is equal to the RMS value of matrix $(A - A_k)$ by definition. Let $B = A - A_k$. Then, by equation 7.15 and fact 2:

$$\sigma = \frac{1}{\sqrt{n \cdot n}} ||B||_F = \frac{1}{n} \sqrt{\sum_{i=k+1}^{n} \lambda_i^2}$$

$$\therefore \sigma\sqrt{n} = \frac{1}{\sqrt{n}} \sqrt{\sum_{i=k+1}^{n} \lambda_i^2} \tag{7.19}$$

The 2-norm of $A - A_k$ is just equal to the largest singular value (equivalently, here, the largest eigenvalue) of $A - A_k$, which is the first eigenvalue not kept in A. Note that the condition that A is PSD is not critical; as long as all negative eigenvalues are smaller in magnitude than $\lambda_{k+1}$, the equivalence between $\lambda_{k+1}$ and $||A - A_k||_2$ will hold. □

Theorems 7.1 and 7.2 and the experimental data in figure 7.2 suggest further criteria which suggest the appropriate dimension to use for low-rank kernel approximation or the number of relevant dimensions that can be reliably extracted using kernel PCA in the presence of kernel noise:

**Criterion 7.2** (Eigenvalue criterion)**.** *Given a kernel function $K$ perturbed by zero-mean noise of standard deviation $\sigma$, low-rank approximation should use only eigenvectors corresponding to eigenvalues $\lambda_i$ such that $\lambda_i \gg \sigma$.*

**Criterion 7.3** (Spectral gap criterion)**.** *Given a kernel function $K$ perturbed by zero-mean noise of standard deviation $\sigma$, let the eigenvalues of the kernel matrix be named $\lambda_i$, sorted in descending order. Low-rank approximation should use at most $k - 1$ dimensions, with $k$ such that*

$$\lambda_k - \lambda_{k-1} > \sigma \text{ and } \lambda_{k+1} - \lambda_k \leq \sigma \tag{7.20}$$

*That is, use only eigenvectors corresponding to eigenvalues which are separated from their neighbors by at least $\sigma$.*

**Acknowledgments**

The authors would like to thank John Chodera for clever statistical insight. ISH acknowledges support from an NSF graduate fellowship. The authors acknowledge award NSF MRI-R2 for computing resources, funded under the American Recovery and Reinvestment Act of 2009 (Public Law 111-5).

## 7.7 Appendix 1: Detailed experimental methods

### 7.7.1 Figure 7.1

The molecules used for this plot were the 57,248 molecule "Maybridge+BBP" dataset from Haque [40]. 293 molecules were chosen at random as reference molecules; for each of these, a further 1000 molecules were chosen at random and overlaid onto their references using PAPER [39], using initialization modes 1 (4 starting points) and 2 (12 starting points, including all 4 from mode 1). The total number of overlay volumes histogrammed in the figure is 293,000.

Overlap volume was computed by numerical integration of equation 7.3, over all atoms (including hydrogens) and Batsanov van der Waals radii [6]. The integration code computed a bounding box for each molecule in an overlay, grew the box by 1 Åin each direction (+x, -x, +y, etc.), and converted this to a cubic grid with resolution 0.3 Å. Integration was performed in single precision over the grid with more points.

### 7.7.2 LINGO calculations in Figures 7.2, 7.3

The molecules used for this plot were taken from the Maybridge Screening Collection (N=56842), represented as canonical isomeric SMILES. The order of SMILES strings was shuffled to remove local correlations between molecules adjacent in the file. Basis sets were drawn as the first X strings in the shuffled file, for each of the basis sizes. The final

32,768 strings in the shuffled file were separated into 8 test sets of size 4,096. For each basis size, dimensionality, and noise $\sigma$, all-pairs approximate kernel values were computed on each test set and subtracted from the true kernel (or true kernel plus noise, in the case of $\sigma \neq 0$). The square errors were then accumulated over test sets; each bar thus represents $8 \times 4096 \times 4096 \times \frac{1}{2} \approx 67 \times 10^6$ kernel evaluations.

Kernel evaluations were performed using a version of SIML modified to compute only the LINGO intersection, and not the full Tanimoto [42].

### 7.7.3 Shape calculations in Figures 7.2, 7.3

The first 2612 basis molecules were taken from the PubChem3D shape fingerprint basis set [27]. All remaining basis molecules were taken from a k-centers+k-medoids clustering of PubChem3D based on ROCS Color Tanimoto, with clustering performed independently on subsets defined by molecular volume cutoffs in the shape fingerprint basis.

The test set was constructed as 159 sets of 4000 single-conformer molecules randomly chosen from PubChem3D. Molecules were chosen without replacement within each set, but with replacement between sets. On average, each pair of sets shared one molecule in common. Overlays were computed using PLASTIC, a version of PAPER [39] modified to include support for "color" similarity analysis, and the ImplicitMillsDean color forcefield from OpenEye ROCS. Overlays were computed optimizing for summed shape and color similarity, but only the shape overlay scores were used to generate plots in this paper. RMS errors were computed as for LINGO analyses, but over 159 test sets rather than 8; each bar thus represents $159 \times 4000 \times 4000 \times \frac{1}{2} \approx 1.3 \times 10^9$ kernel evaluations.

### 7.7.4 Differential eigenspectrum plot

Computed first forward difference function of each kernel matrix's eigenspectrum by applying numpy diff operator to each eigenspectrum. Smoothed each trace for visualization using a 9-wide moving average filter (4 previous samples, current sample, and 4 forward samples, each with weight 1/9).

## 7.8 Appendix 2: Proof that LINGO is a proper kernel

The LINGO intersection between two strings $x$ and $y$ relies on first transforming each string to a multiset [42, 85]. For the $q$-LINGO algorithm, each contiguous 4-character substring in $x$ is mapped to a multiset element; the multiplicity counts the number of times that substring appears in $x$. The LINGO similarities in this work use $q = 4$. After transforming $x$ and $Y$ to multisets $X$ and $Y$, the LINGO intersection is computed as $|X \cap Y|$: sum, for each element present in $X$ or $Y$, the minimum of the multiplicity of that element in X and that in Y.

For strings from an alphabet with $k$ characters, the multiset constructed for $q$-LINGO is equivalent to a histogram over $k^q$ elements: all possible $q$-character substrings in the alphabet. Then, the LINGO intersection is equivalent to the histogram intersection function, proven to be a kernel by Odone [66].

# Chapter 8

# Real-Time 3D Chemical Similarity Search over PubChem


## Abstract

Similarity search over million-molecule-scale chemical databases is a bottleneck for emerging analyses in computational biochemistry. In this chapter, I show that combining specialized hardware and approximation algorithms overcomes this bottleneck, allowing real-time search performance with excellent accuracy. The performance of the method is demonstrated for 3D shape and chemical functionality ("color") similarity on the 17 million-molecule NCBI PubChem3D database.

## 8.1 Introduction

Continuing improvements in both computer power as well as chemical high-throughput screening have dramatically expanded the size of biochemical databases. Simultaneously, virtual screening has become a commonly-used tool in medicinal chemistry, such that medicinal chemists may routinely screen chemical ideas or known active hits against large databases of existing, purchasable, or synthesizable chemical matter. As the sizes of these databases are often beyond one million compounds, high speed is necessary to support interactive usage of chemical similarity search, and is of critical importance to drug discovery.

However, many useful chemical similarity measures are too slow to be used in an interactive manner over large databases. In particular, "3D" similarity measures, which consider the three-dimensional arrangement of atoms in a molecule rather than just atom types and bond connectivity, are often very slow, taking on the order of 10 ms to 10 sec per comparison. Without massive dedicated computational resources, it is impossible to support interactive use of these tools over large-scale databases.

In this chapter, we describe how, for a particular pair of 3D similarity measures, combining special-purpose hardware (graphics processing units) and an approximation algorithm enable interactive 3D chemical search over the 17 million-molecule PubChem3D database. We demonstrate very high accuracy over the diverse PubChem3D library, and show that we are able to achieve throughput of tens of millions of similarity calculations per second on a single server, thousands of times faster than the unaccelerated calculation.

## 8.2 3D Similarity Measures

This section reviews shape and color similarities, two related types of chemical similarity measures that take into account the three-dimensional nature of molecules. The versions of shape and color we consider are based on the Gaussian model of molecular shape [35]. While other methods for three-dimensional similarity have been considered [5, 18, 46, 48, 76], the model based on Gaussian shape is both efficient to compute [33, 39] and has shown good performance in drug discovery applications [75].

### 8.2.1 Shape

Shape similarities, as used here, model the volumetric similarities between molecules. To do this, the density function of a molecule is represented as the union of atom-centered spherical Gaussian functions $\rho_i$ [35]. While less intuitive than a "hard-sphere" model, in which the molecule is represented as the union of finite-radius spheres centered at each atom, the Gaussian model has the advantage of being a smooth function in space, which enables gradient calculation and efficient evaluation.

Given two molecules A and B, the shape overlap is defined in terms of the total volume shared by the two molecules ($|A \cap B|$). Since each molecule is defined in terms of its component atoms, the principle of inclusion-exclusion implies that this volume can be defined in terms of second- and higher-order intersections between the atoms: $|A_i \cap B_j| - |A_i \cap A_j \cap B_k| - |A_i \cap B_j \cap B_k| + |A_i \cap A_j \cap B_k \cap B_l| + \cdots$. However, to reduce the complexity of evaluating this objective function, implementations typically truncate this calculation to just the second-order (pairwise overlap) term: $|A_i \cap B_j| \ \forall i, j$ [33, 39]. In principle, the shape overlap between two molecules is defined as the global maximum of this volume overlap objective, optimized over all rigid-body transformations of either molecule. This optimization is usually performed by local optimizations starting from many starting points; while not guaranteed to be globally convergent, this local optimization procedure appears to perform well in practice.

Because the shape overlap is not a normalized measure (larger molecules will naturally have larger overlap volumes), Gaussian shape similarity scores are usually reported in terms of a Tanimoto coefficient:

$$T_{AB} = \frac{O_{AB}}{O_{AA} + O_{BB} - O_{AB}}$$

Where $O_{xy}$ is the overlap volume between molecules $x$ and $y$. Since overlap volumes are always positive, this Tanimoto is a normalized similarity between 0 and 1.

### 8.2.2 Color

Computing chemical similarity by excluded volume, as done in shape similarity, makes the modeling assumption that sterics are the dominant factor distinguishing molecules; if two molecules have similar steric excluded volume, then they will be shape-similar. However, this assumption is clearly not always true. Figure 8.1 depicts the molecular structures as well as excluded volume for benzene and pyridine. While these two molecules have almost identical sterics (pyridine is missing one hydrogen, and has a nitrogen whose radius is slightly smaller than that of carbon), they have very different physical properties. In particular, the nitrogen in pyridine confers water-solubility and a hydrogen-bond acceptor site. For this reason, it is of interest to consider the sites of particular chemical functionalities in space in addition to the simple steric exclusion.

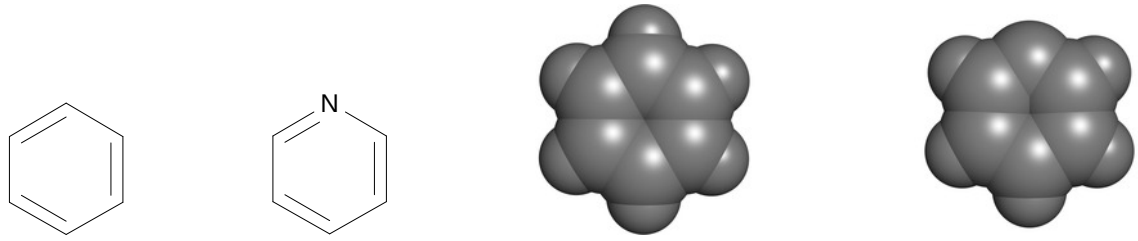


(a) Benzene (b) Pyridine (c) Benzene shape (d) Pyridine shape

Figure 8.1: Comparison of molecular structure and volume for benzene and pyridine

One method, known as color similarity, incorporates this chemotype matching into the Gaussian shape framework by adding virtual atoms to represent particular chemical functionalities. Functionalities of interest (e.g, hydrogen bonding sites and charged sites) are defined by SMARTS (cite) strings, which identify molecular subgraphs corresponding to the desired function. A virtual "color" atom is then added to the molecule at a site associated with the functionality (e.g., at the centroid of the set of atoms that match the given SMARTS pattern). A "color force field" defines the interactions of these color atoms; for example, in the OpenEye Implicit Mills-Dean color force field, color atoms do not interact with "real" (shape) atoms, but do have a positive interaction with atoms of their same color type (e.g., anion-anion). The color overlap can then be computed using the same Gaussian overlap model as in shape. The similarity between color atoms alone can be separated from

that defined by the shape atoms; this leads to two different similarity measures between molecules, the shape and color Tanimotos. It is common to consider the so-called "combo" Tanimoto, which is the sum of shape and color Tanimotos, divided by 2 to keep it in the [0,1] interval.

## 8.3 GPU Implementation of 3D Color Similarity

GPU acceleration plays a key role in our ability to deliver real-time search performance over very large chemical databases. In previous publications [39, 41], we described the design and implementation of PAPER (PAPER Accelerates Parallel Evaluations of ROCS), a GPU-accelerated implementation of shape-only molecular similarity using the Gaussian model of shape. Here, we describe the implementation of PLASTIC (PLASTIC aLigns Atoms with Shape Theory Incorporating Color), an extension to PAPER that adds support for color similarity calculations.

As described in section 8.2.2, color overlap interactions are computed in the same manner as shape interactions, but on different sets of atoms, with interactions defined by a color force field (CFF). In PLASTIC, shape and color are unified, with shape defined by an implicit CFF rule adding a positive interaction between "shape" type atoms; the only difference between shape atoms and color atoms of other types is that shape atoms can have distinct radii (e.g., hydrogen and carbon will typically not be modeled with the same radius), whereas other color types are usually defined with identical radii (e.g., all anion virtual atoms have the same radius). However, this distinction is an implementation detail and not critical to the method.

Three principal changes are required to implement color on the GPU: two involving data structures and one in the core algorithm. In PAPER, each molecule uploaded to the GPU is represented by a scalar count of atoms, 3 arrays containing coordinates of each atom in the x, y, and z axes, and a final array containing a precomputed function of each atom's radius. In PLASTIC, the atom count scalar is extended to a vector. The first element of the vector contains the total number of atoms in the molecule (shape and all virtual types); each subsequent element contains the number of atoms of a particular type. An additional CFF data structure is also uploaded to the GPU, defining the interactions in the

CFF (e.g., anion-anion) and their weights. The weights are scalar multipliers controlling the contribution of each interaction to the final objective score: $O(a,b) = \sum w_i O_i(a,b)$, where $O(a,b)$ is the objective between molecules $a$ and $b$, $w_i$ is the weight of interaction $i$, and $O_i(a,b)$ is the overlap between $a$ and $b$ considering only interaction type $i$.

The final GPU-side change from PAPER to PLASTIC is to the objective/gradient evaluation loop. In PAPER, all pairs of atoms from the reference and fit molecules contribute interactions to the final overlap value. However, with the addition of a color force field, this is no longer true: typically, for example, shape and color atoms would not interact with each other. Thus, in PLASTIC with a typical CFF, the interaction matrix is block-diagonal, rather than full. Using the PAPER interaction loop (in which every term of the interaction matrix is evaluated) would be highly wasteful of computation. Instead, in PLASTIC a PAPER-style interaction loop is embedded in an outer loop over the interaction terms in the CFF; iterations of the outer loop are separated by a thread barrier (CUDA `__syncthreads`). This strategy means that only valid atom pairs are evaluated. However, because there are typically very few color atoms of any given type in a molecule, the evaluation of color terms is inefficient on the GPU, as there are usually more available scalar processing units (CUDA threads) than there are atom-pair interactions for color interactions. In principle, it would be possible to run multiple interactions simultaneously, without the barrier, but this has not been implemented. Even with this inefficiency, we achieve typical performance of 15,000 shape+color overlay optimizations/sec for PLASTIC on the PubChem3D database, on an NVIDIA GeForce GTX 480.

## 8.4 Fast Similarity Approximation by Metric Embedding

The SCISSORS technique is an approximation technique to rapidly approximate chemical similarities by precomputing vector embeddings for molecules in a static database, and is generalizable to many similarity measures, given technical conditions on their eigenvalue spectra [40]. We apply the SCISSORS method to enable rapid shape and color searches on PubChem3D; in this section we briefly review the relevant details behind SCISSORS.

The first step in computing SCISSORS-approximated Tanimotos on a large chemical database of size $N$ is to select a "basis set" of molecules from the database, of size $k$,

where $k$ is typically much less than $N$; the original SCISSORS paper suggests that random sampling of the database is a good way to pick a basis. Similarities are then computed among all pairs of molecules in the basis set, stored in a matrix $G$, and converted to inner products using the relation:

$$\langle A, B \rangle = \frac{2T_{AB}}{1 + T_{AB}}$$

A spectral decomposition of $G$, $G = VDV^T$ is then computed, and a desired dimension $d$ for the vector space is chosen. The eigenvalues in $D$ are sorted in descending order (and corresponding eigenvectors are sorted), and all eigenvalues other than the top $d$ are set to zero. The vector space representation for the basis molecules is then equal to the first $d$ columns of the matrix $VD^{1/2}$, where the vector for the $i$th basis molecule is the $i$th row of the matrix. This spectral decomposition was proven to be the least-squares optimal choice to represent the molecules' computed inner products, under the $d$-dimensional constraint.

To compute the vectors for a "library", or non-basis molecule, that molecule is compared against each basis molecule, the similarities are converted to inner products using the above relation, and the inner products are stored in a vector $L$. The vector $x$ representing that library molecule is computed by solving the linear least-squares equation $VD^{1/2}x = L$. Finally, the SCISSORS-approximated Tanimoto for a given pair of molecules $a$ and $b$ is computed using the vector Tanimoto relation on their vectorial representations $A$ and $B$:

$$T_{ab} = \frac{\langle A, B \rangle}{\langle A, A \rangle + \langle B, B \rangle - \langle A, B \rangle}$$

On any given dataset and similarity measure, SCISSORS has three tunable parameters: the size of the basis set used, the choice of basis molecules given a fixed basis size, and the desired dimensionality of approximation. In the remainder of this chapter, we sample this parameter space and show that we are able to find SCISSORS parameters that allow accurate approximation of shape and color Tanimotos on a large (>17M molecule), diverse chemical dataset.

## 8.5 Materials and Methods

### 8.5.1 Databases

To demonstrate the performance and accuracy of our techniques on a large, diverse chemical library, we will use the PubChem3D database [10], which contains single-conformer 3D models of (at the time of the work) 17,093,120 small molecules, approximately 90% of the molecules in the entire NCBI PubChem Compound collection. PubChem3D represents a broad swath of both druglike and non-druglike organic chemistry space, and therefore demonstrates the generalization performance of our techniques onto diverse libraries.

### 8.5.2 Software

We present results of SCISSORS approximations for shape and color Tanimotos computed using two different GPU packages for Gaussian shape overlay. Our PLASTIC code is an extension of the open-source PAPER package for molecular overlay [39] that adds color chemotype matching capability. We also tested using a prerelease version (version prerelease-1.0.6) of the commercial FastROCS package, from OpenEye Scientific Software. Atomic radii for PLASTIC were assigned using Batsanov van der Waals radii [6]; FastROCS uses an approximate technique to evaluate the overlap objective which requires it to assume that all atoms have the same radius as carbon. Finally, PLASTIC considers color during the course of overlay optimization, considering color during both pose estimation as well as final scoring of starting points and molecules. FastROCS performs local optimization purely based on shape and rescores final poses including shape and color; these joint scores are then used to select among initial starting points and molecules.

Both programs used the OpenEye Implicit Mills-Dean "color force field", or set of SMARTS queries defining the placement, weight, and radius of virtual color atoms; PLASTIC used the SMARTS matcher from OpenBabel whereas FastROCS used an OpenEye-developed SMARTS matcher. Implicit Mills-Dean defines six color types: anion and cation, hydrogen bond donors and acceptors, hydrophobic groups, and rings; interactions have positive weight for self-interactions (e.g., anion in query vs anion in fit); and all color atoms are Gaussians with radius 1 Å.

### 8.5.3 SCISSORS Basis Sets

The primary SCISSORS basis set we used in this work was the PubChem Shape Fingerprint set [11], a set of 2,612 molecules chosen by clustering to cover the shape diversity of a multi-conformer representation of the molecules in PubChem3D. For experiments using FastROCS, we used a 2,611-molecule subset excluding hydrobromic acid (HBr), because FastROCS will not accept molecules with only one non-hydrogen atom. This basis set will be called the PC3DFP basis.

We also performed a clustering of PubChem3D based on color Tanimoto values computed using the CPU implementation of ROCS (release 1.7.2, version 20091103), also from OpenEye, using the "Analytic2" mode. For this clustering, PubChem3D was broken into seven sets by molecular volume, according to the same divisions used to compute the Shape Fingerprint set; these sets were then clustered using the k-centers clustering algorithm, followed by two update rounds of k-medoids. The 2,500 cluster centers (molecules) with the highest number of other molecules associated to them by color Tanimoto distance were kept as additional basis molecules.

In basis-vs-dimension plots presented here, bases of 2,612 or fewer molecules are comprised entirely of sequential subsets of the Shape Fingerprint basis set. Because of the way the PC3DFP basis was assembled from its subsets (concatenation of SDF files), subsets of fewer than 2,612 (or 2,611 for FastROCS) molecules are biased in that they exclude more molecules with few heavy atoms than ones with many heavy atoms. Bases of more than 2,612/2,611 molecules were constructed by augmenting the entire PC3DFP basis with an appropriate number of the highest-population cluster centers from our color clustering of PubChem3D, in descending order of cluster population.

### 8.5.4 Evaluation Methodology

To evaluate the performance of SCISSORS with different parameter settings (basis size and dimensionality), we assembled a number of evaluation sets by random sampling from PubChem3D. Each set consists of 4,000 molecules chosen uniformly at random from PubChem3D. Molecules were chosen without replacement within each set, but with replacement between sets; on average, each pair of sets shares one molecule in common. 159 such

sets were used for evaluating SCISSORS with PLASTIC and a subset of 140 were used to evaluate SCISSORS with FastROCS.

On each set, we computed all pairwise Tanimotos among members of the set, as well as the Tanimotos between each molecule in the set and each basis molecule, using both PLASTIC and FastROCS. SCISSORS shape and color vectors were computed using these library-vs-basis Tanimotos and SCISSORS Tanimotos computed on those vectors. The SCISSORS Combo Tanimoto was computed as the average of SCISSORS shape and color Tanimotos. We then evaluated error at each parameter choice by pooling all 159 (resp., 140) sets and comparing SCISSORS Tanimotos to PLASTIC or FastROCS Tanimotos. All data for PLASTIC in figures 8.2, 8.3, 8.5, 8.6, and 8.7 corresponds to $159 \times 4000 \times 4000 \times 0.5$ unique Tanimotos. FastROCS data in the same figures was accumulated over $140 \times 4000 \times 4000 \times 0.5$ unique Tanimotos. Note that fewer molecule pairs contributed to figure 8.4, because only pairs with true color Tanimoto $> 0.5$ were considered in that plot.

## 8.6 Results: Parameter Selection

Figures 8.2, 8.3, and 8.4 show the results of our tests of SCISSORS as a function of basis set size and dimension for PLASTIC and FastROCS. For shape and color Tanimotos, we illustrate both the root-mean-square error between the SCISSORS and true Tanimotos as well as the mean error of (SCISSORS - true).

The features of the plots are broadly similar for PLASTIC and FastROCS, with only small differences in magnitude between the two. For both methods, an error minimum on shape is achieved around 256 dimensions; interestingly, adding additional basis molecules beyond the 2,612 in the PC3DFP basis did not significantly help. Beyond 256 dimensions, the RMS error in both methods starts to rise. This effect can be explained by looking at the mean error plot: SCISSORS Tanimotos systematically underpredict the true shape Tanimoto at high dimensions. This happens because additional dimensions learned are essentially random, so the SCISSORS Tanimoto converges to around 0.2-0.3, the Tanimoto between a pair of random vectors. For both methods, both the mean and RMS errors for shape converge to a minimum in absolute value at 256 dimensions and 2,612 (2,611 for FastROCS) basis molecules, so we used this for the vector expansion of PubChem3D.

The similarity in plot features between PLASTIC and FastROCS carries over to color Tanimotos. However, the distribution of color Tanimotos in the dataset makes the interpretation of the RMS error plots (figure 8.3) dangerous. Both the RMS error and the mean error in Tanimotos appear to converge to zero as more dimensions are added, in contrast to the case for shape. However, this is because the most common value for the color Tanimoto is quite low - around the 0.2-0.3 value found for a pair of random vectors. Thus, adding additional dimensions reduces the RMS error purely by coincidence. A useful way to measure error in this case is to only consider molecule pairs with a true color Tanimoto greater than 0.5 (figure 8.4). For these molecules, adding dimensions clearly increases the mean error past 128 dimensions. Ultimately, the best dimensionality was chosen to balance two factors: underestimation of high Tanimotos and overestimation of low Tanimotos. Color appears to be a very noisy measure (unsurprising, since there are very few color atoms per molecule, which subsequently contribute little to overlay optimization), making clean estimation difficult. To balance the error in low and high Tanimotos, we decided to expand color in 192 dimensions for PLASTIC and 256 dimensions for FastROCS, by examination of plots similar to those in the next section.

## 8.7 Results: Accuracy

Figures 8.5, 8.6, and 8.6 show scatter-density plots of SCISSORS shape, color, and combo Tanimotos versus true Tanimotos computed by PLASTIC and FastROCS, using the PC3DFP basis and dimensionality chosen in the last section. It is immediately apparent from the shape approximation plot (figure 8.5) that SCISSORS is able to approximate shape Tanimotos very accurately: within approximately 0.05 RMS Tanimoto error for PLASTIC and 0.03 RMS error for FastROCS. Interestingly, this is very close to the optimal approximation that should be possible even in theory. Because of the truncated objective functional and use of a local optimizer, shape Tanimotos computed using the presented Gaussian shape overlay algorithm are actually somewhat noisy with respect to the true shape Tanimoto. Figure 8.8 shows a histogram of true shape Tanimotos (computed on a subset of the Maybridge Screening Calculation) based on the "optimal" poses found by PAPER with 12 starting points rather than 4. The true overlap volume was computed by numerical integration of the full objective,

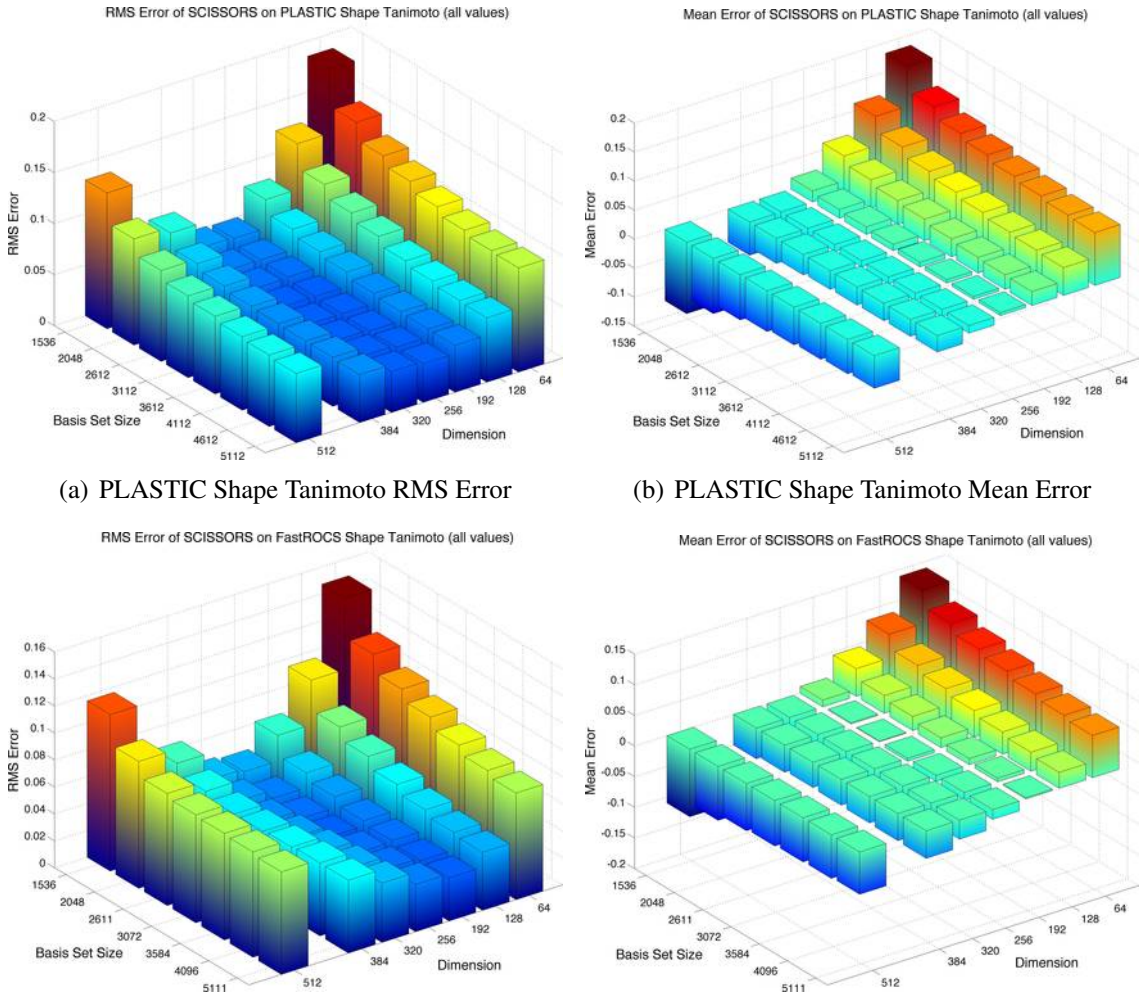


(a) PLASTIC Shape Tanimoto RMS Error

(b) PLASTIC Shape Tanimoto Mean Error

(c) FastROCS Shape Tanimoto RMS Error

(d) FastROCS Shape Tanimoto Mean Error

Figure 8.2: Basis vs Dimension RMS and mean error plots for SCISSORS on PLASTIC and FastROCS Shape Tanimotos for PubChem3D

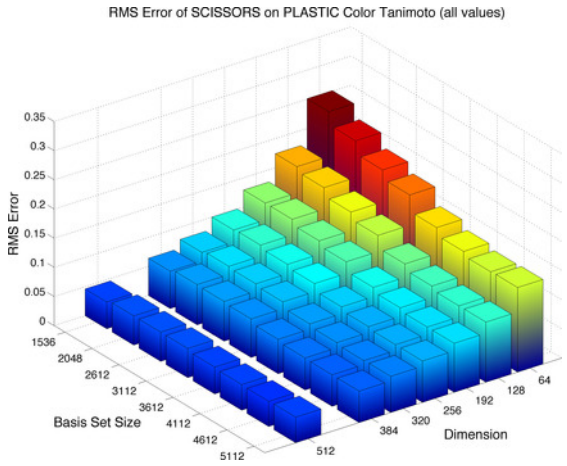


(a) PLASTIC Color Tanimoto RMS Error (all values)

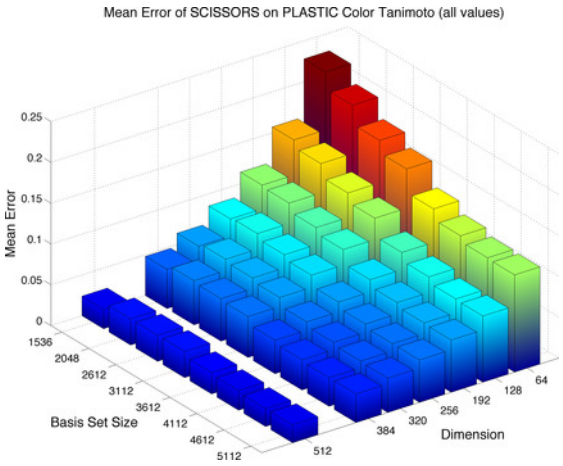


(b) PLASTIC Color Tanimoto Mean Error (all values)

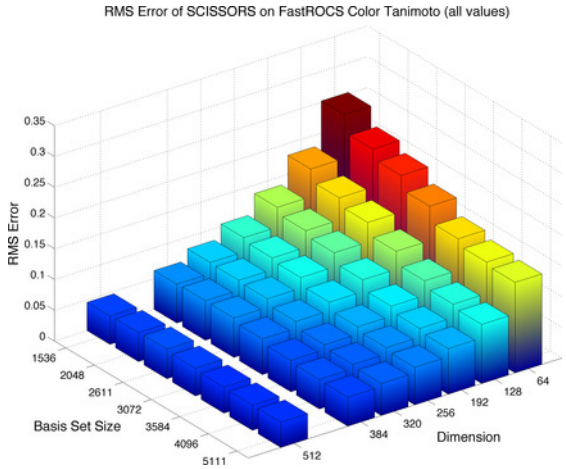


(c) FastROCS Color Tanimoto RMS Error (all values)

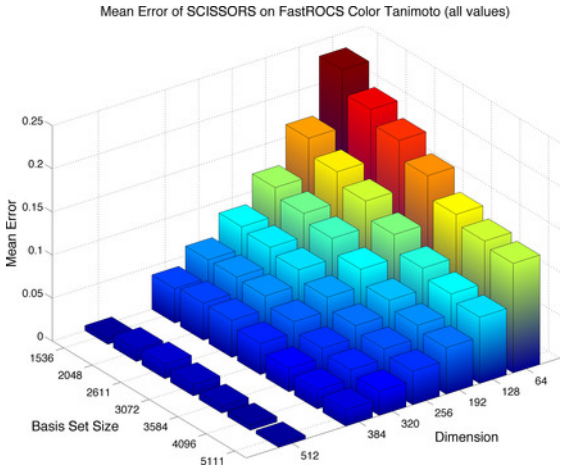


(d) FastROCS Color Tanimoto Mean Error (all values)

Figure 8.3: Basis vs Dimension RMS and mean error plots for SCISSORS on PLASTIC and FastROCS Color Tanimotos for PubChem3D (all values)

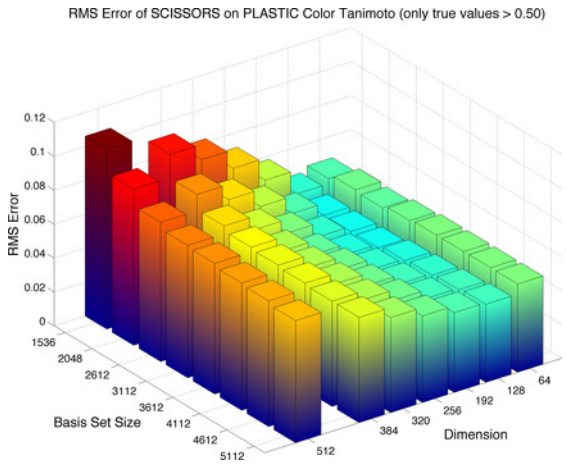


(a) PLASTIC Color Tanimoto RMS Error (true color Tanimoto $> 0.5$)

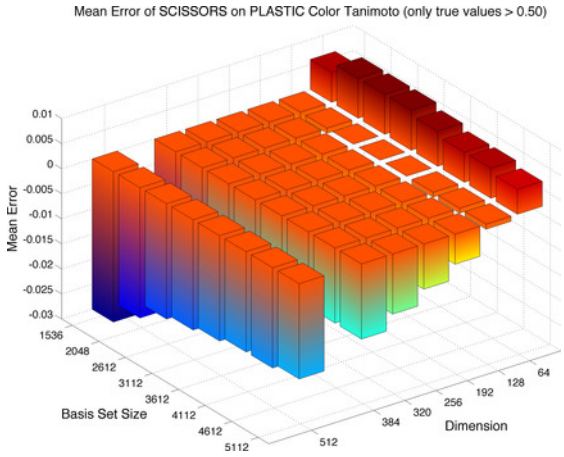


(b) PLASTIC Color Tanimoto Mean Error (true color Tanimoto $> 0.5$)

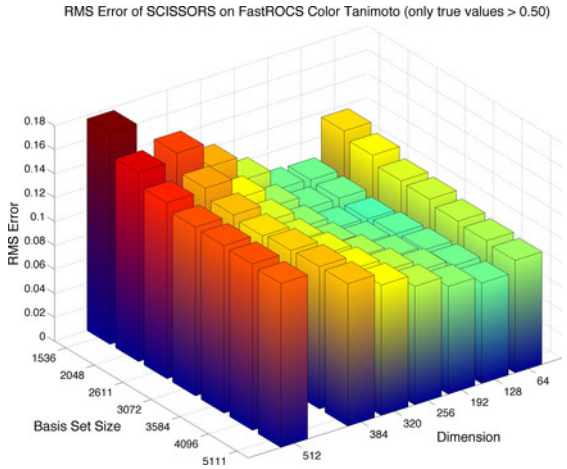


(c) FastROCS Color Tanimoto RMS Error (true color Tanimoto $> 0.5$)

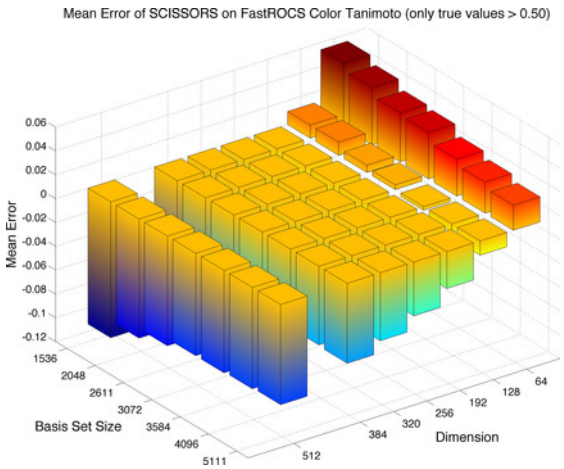


(d) FastROCS Color Tanimoto Mean Error (true color Tanimoto $> 0.5$)

Figure 8.4: Basis vs Dimension RMS and mean error plots for SCISSORS on PLASTIC and FastROCS Color Tanimotos for PubChem3D (true Tanimoto $> 0.5$)

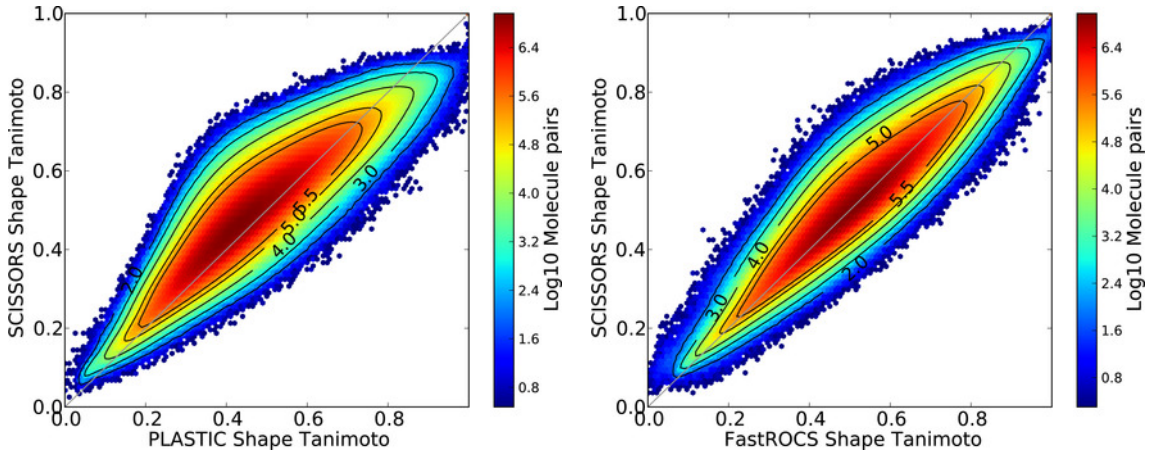


(a) PLASTIC Shape (b) FastROCS Shape

Figure 8.5: SCISSORS approximation based on PLASTIC and FastROCS Shape Tanimotos: 256D, PC3DFP basis set

rather than the truncated version. Because the 12 starting points are a superset of the 4, one would expect that using more starting points would strictly dominate. However, what is actually seen is almost zero mean shift, with a standard deviation ($\sigma = 0.03$) almost an order of magnitude larger than the mean shift ($\mu = 0.005$). The RMS error of SCISSORS approximations on both PLASTIC and FastROCS is of similar magnitude to this inherent noise in our "ground truth" calculation, suggesting that it is unreasonable to expect to do better.

Figure 8.6 illustrates the performance of SCISSORS on color Tanimotos. SCISSORS is able to approximate the color Tanimoto, but with a much broader range in performance than on shape; this is likely due to two factors. First, the mean color Tanimoto (approx 0.1-0.2) is much lower than the mean shape Tanimoto (approx 0.5). In vector-space, this implies that most molecules are nearly orthogonal to one another; a situation that is inherently difficult to approximate well in low rank. This is compounded with higher apparent noise in the color calculation. While we have not investigated the cause of this noise in great depth, we speculate that there may be two causes. Firstly, there are many fewer color atoms per molecule than there are shape atoms; thus, there may be a small-sample-statistics effect at work. More fundamentally, color overlap is a very small (for PLASTIC) or nonexistent (for FastROCS) component of the optimization objective when

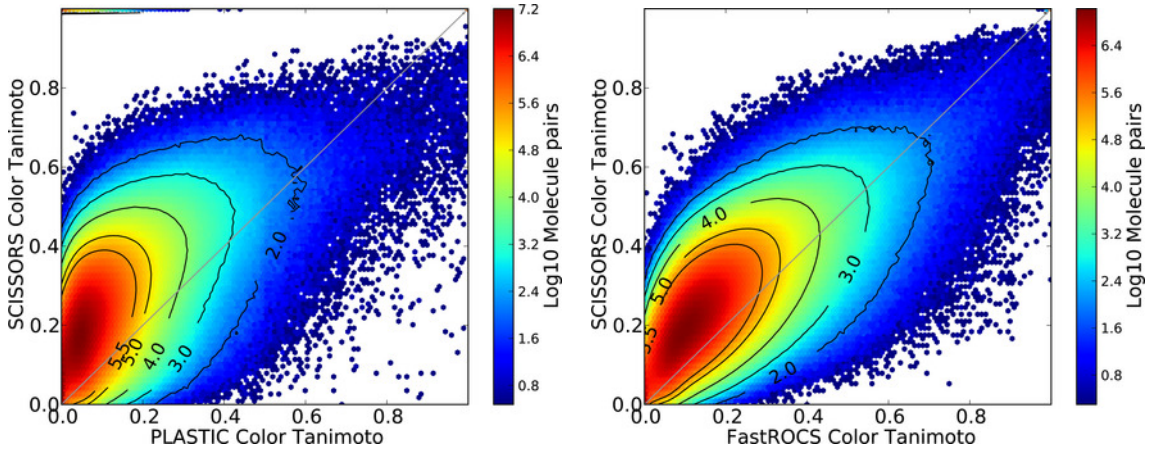


(a) PLASTIC Color (b) FastROCS Color

Figure 8.6: SCISSORS approximation based on PLASTIC and FastROCS Color Tanimotos: 192D PLASTIC, 256D FastROCS, PC3DFP basis set

molecular overlay estimates the correct overlay pose. Thus, only very limited optimization is done of the color Tanimoto, which broadens the estimation of color Tanimoto over the true value. Nevertheless, estimation of the color Tanimoto alone is of little practical interest: typically, color (chemotype) similarity is used jointly with shape similarity, not on its own.

Figure 8.7 shows a more realistic case, in which SCISSORS is used to approximate the combo Tanimoto: the scaled sum of shape and color similarity. This combination is frequently used in virtual screening applications to find relevant ligands based on an active query [75]. SCISSORS is able to compute excellent approximations to the shape and color combination, because adding shape information reduces the noise in the color approximation. Figure 8.9 shows the joint distribution of PLASTIC shape and color Tanimotos over our PubChem3D evaluation set. Of particular note is that high color similarity depends on high shape similarity (the upper-left quadrant is nearly empty). This correlation helps reduce the noise in the combo Tanimoto distribution, particularly at large combo Tanimoto values.

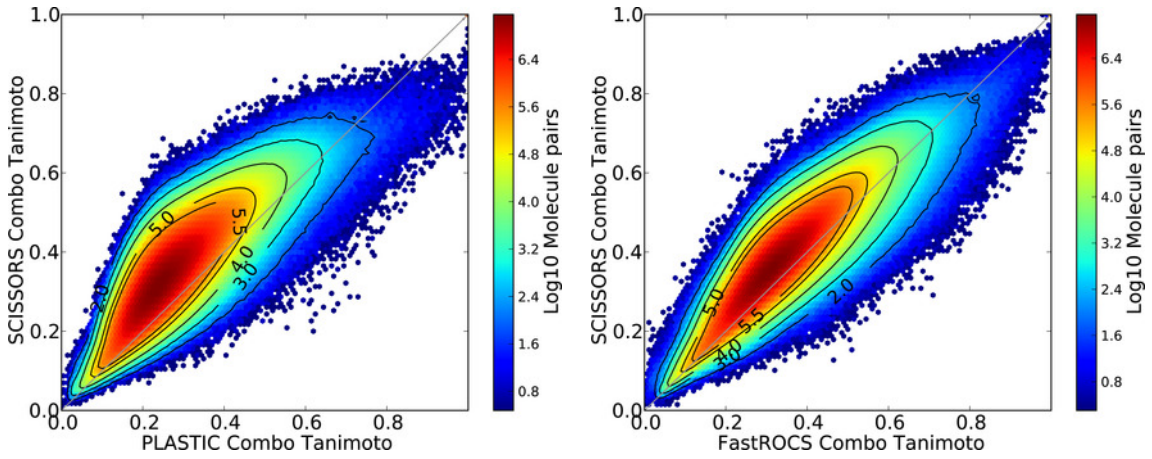


(a) PLASTIC Combo (b) FastROCS Combo

Figure 8.7: SCISSORS combo Tanimoto approximation based on PLASTIC and FastROCS: Shape in 256D for both; color in 192D for PLASTIC and 256D for FastROCS; PC3DFP basis set

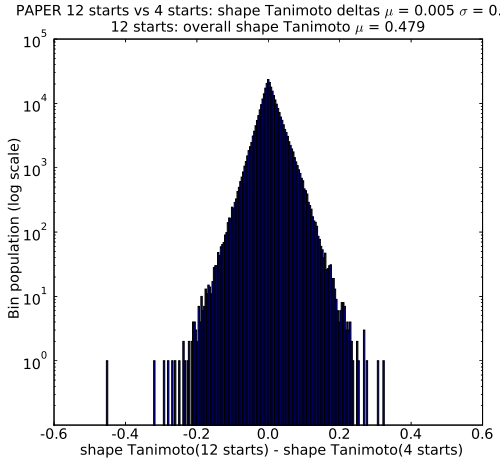


Figure 8.8: Histogram of change in true shape Tanimoto from using 12 starting points rather than 4 with PAPER

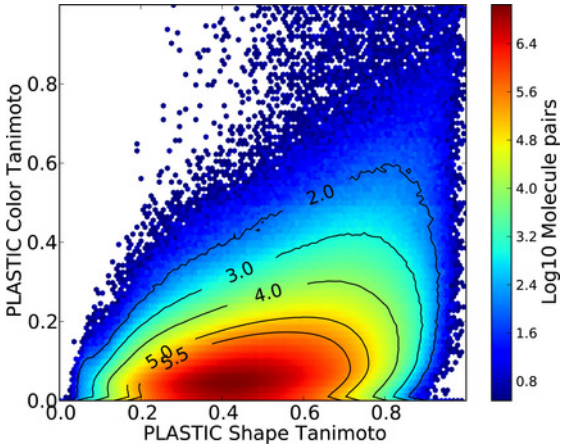


Figure 8.9: Density plot of PLASTIC color vs shape Tanimotos on PubChem3D evaluation set

## 8.8 Results: Throughput

Combining GPU acceleration for direct shape and color Tanimoto calculation with the SCISSORS approximation algorithm enables real-time search throughput on PubChem-scale databases. Given precomputed vector representations for the database molecules (which we have computed for all of PubChem3D), the PLASTIC+SCISSORS combination can do a full shape and color search for a new query compound (not present in the database) against the entire database in approximately one second on one server. Performing multiple queries simultaneously against the same database can further amortize this cost; in the $N^2$ limit of computing all pairwise similarities, we are able to achieve approximately 274,000x speedup relative to using ROCS to compute all similarities.

Precomputation of the database vectors is a significant, though not prohibitive, expense. This is dominated by the cost of performing the direct shape and color Tanimoto calculations, both pairwise between basis molecules, and between library and basis molecules; the number of Tanimoto calculations required for $B$ basis and $L$ library molecules is described by the equation:

$$NumTan = \frac{(B)(B-1)}{2} + LB$$

For even modest library sizes, this is rapidly dominated by the latter term (since the basis is typically much smaller than the library). For PubChem3D, we must evaluate approximately $2600^2/2 + 2600 * 17 \times 10^6 \approx 44.2 \times 10^9$ Tanimotos: approximately one month of computation on a single NVIDIA GeForce GTX 480 GPU using PLASTIC. The subsequent linear algebra steps (eigendecomposition of the basis matrix and least-squares projection of library vectors) are negligible in cost, taking hours on a few CPU cores. At the chosen dimensionalities, the vector representations fit in under 35GB of storage.

Once the database vectors have been computed, searching based on a new non-database query proceeds in two steps. First, PLASTIC is used to compute Tanimotos from the query against the database basis set; at 2,612 basis molecules, this takes under 200ms on a single GPU. These Tanimotos are then projected into the SCISSORS vector space (milliseconds or less), and finally vector Tanimotos are computed against the database vectors. For a single query, the dominant cost in computing these vector Tanimotos is the time of streaming vectors in from main memory to the CPU. A typical 2010-era server

able to keep the SCISSORS database in memory will feature approximately 40GB/s of main memory bandwidth (20GB/s per socket, over two CPU sockets); thus, this phase can complete in under a second. Indeed, because this $\sim$ 1-second cost is constant, several query molecules (or conformers) represented by distinct vectors can be compared at the same time with essentially no additional slowdown until an arithmetic performance limit is reached. The particular limit depends on CPU architecture and number of cores, but typical current servers should be able to handle ten simultaneous queries with no slowdown relative to one.

GPUs can also be used profitably to accelerate the vector-comparison portion of the SCISSORS search scheme. The most expensive part of the Tanimoto calculation is the dot product between the two vectors; GPUs are highly efficient at performing this type of dense linear algebra. However, GPUs typically have much smaller amounts of onboard memory than would be available to a CPU on a server. Thus, they are not well-suited (in the absence of multi-GPU parallelism) to performing single-query-vs-database searches. Only small database pieces could be stored on-GPU at a time, which would constrain the search to the rate at which database pieces could be moved from main memory across the peripheral bus to the GPU ($\sim 4$ GB/s).

GPUs are an excellent choice for larger comparisons, such as $N^2$ pairwise similarity problems. These applications are able to reuse database vectors more effectively, and are therefore bound by arithmetic throughput rather than memory bandwidth. The dominant costs in computing a SCISSORS combo Tanimoto based on the PLASTIC vectors described here are a 256D and a 192D dot product, which combined require approximately 450 multiply-adds. The NVIDIA GeForce GTX 580, a current high-end GPU, has 512 scalar processors clocked at 1.544GHz, with each scalar unit able to perform one fused multiply-add (FMA) per cycle; these specifications imply an upper bound of $\sim 1.8 \times 10^9$ SCISSORS dot products per second. Allowing for additional overhead in the computation (memory loads to cache, division, etc.), even a conservative estimate of 33% efficiency shows that bulk throughput of 600 million shape+color Tanimotos/second is achievable per-GPU: 4 million times faster than the equivalent computation using ROCS on the CPU. In the case of full pairwise similarity comparison of PubChem3D, the pairwise vector Tanimotos would take around 5 days on a single GTX 580. Thus, combining PLASTIC (for library-vs-basis computations) with SCISSORS on the GPU (to accelerate bulk Tanimoto computations)

yields a runtime of around 40 GPU-days to compute $(17 \times 10^6)^2$ shape and color Tanimotos: almost 275,000 times speedup relative to the same calculation on a single CPU using OpenEye ROCS.

## 8.9 Conclusions

The high-speed chemical search capabilities described in this chapter enable a wide range of practical applications for 3-D search methods in drug discovery and computational biochemistry. An interesting direction for drug discovery is the creation of interactive compound design interfaces, in which chemists can design compounds at a computer and receive feedback about the presence of similar compounds in a database in real time. In this application, the reduction in search latency from hours to seconds (or less) enables a level of interactivity simply impossible with prior methods. Clustering methods are also important in drug discovery and industrial project management; they are often used, for example, in managing corporate compound collections and purchases. Compound clustering by hierarchical agglomerative clustering or Jarvis-Patrick [47] requires the computation of O($N^2$) similarities, which is infeasible on million-molecule scale datasets without the acceleration techniques described here. Additionally, because SCISSORS computes a vector embedding for each molecule, it enables the use of more-efficient vector clustering techniques, such as k-means, potentially reducing the computational cost of clustering from quadratic to linear.

Biochemical machine learning also stands to benefit from such techniques. In particular, the use of SCISSORS-approximated similarities for large pairwise comparisons allows rapid assessment of the distribution of similarities in a dataset, and thereby allows accurate assignment of significance scores (e.g., Z-values) to particular Tanimoto values. These significance scores (and, indeed, the approximate similarities themselves) can then be used to induce probabilistic graphical models on chemical data sets. A very simple form of such a learning method would be a k-nearest-neighbors classifier defined on a large data set, using the principle of similarity to predict new function. Such methods can be generalized to more complicated models. For example, thresholding similarities above a certain score (e.g., by statistical significance) could be used to create a graph with molecules at vertices and edges

between "significantly similar" molecules. Given an activity label on a training subset of vertices, this graph could be used to train a Markov random field model of activity. Crucially, O($N^2$) similarity calculations are needed to set up the graph structure of such a model, even if the resultant graph is relatively sparse; the high-speed techniques here described are very well-suited to such O($N^2$) problems.

## 8.10 Acknowledgments

The author thanks Del Lucent (Stanford/CSIRO Molecular and Health Technologies, Melbourne) for contributions to the development of PLASTIC (CPU-side code for parsing color force fields).

# Chapter 9

# Conclusion and Future Directions

In the introduction to this dissertation, I argued that the performance of chemical similarity comparison is a key factor limiting the ability of biochemical machine learning (BML) to scale to next-generation data sets, and that analysis of these data sets will be critical to the continued development of computational biochemistry. These computational limitations occur in both space and time: both our storage capacity and our processing performance are inadequate to handle the largest current data sets.

Through the course of this dissertation, I have demonstrated that a two-pronged approach combining hardware acceleration with approximation algorithms is able to solve both the storage and processing scaling problems for an interesting and industrially-useful class of chemical similarity measures. Specifically, I have used graphics processing units (GPUs) to accelerate the evaluation of both two-dimensional (chemical graph-based) and three-dimensional (shape- and chemotype-based) similarity comparisons by a factor of 30 to 100. I then presented the SCISSORS algorithm, a metric embedding technique that allows high-quality approximate evaluations of the considered 2D and 3D similarities at effective rates thousands to millions of times higher than evaluation of the exact similarity function. This combination can compute similarities faster than precomputed similarities could be read back from disk, effectively solving the storage problem for large-scale similarity problems. Analysis of the SCISSORS algorithm leads to bounds on its approximation performance, based on connections to kernel principal components analysis and the Nyström approximation, as well as an analysis of the behavior of kernel approximation in the presence

of inexact kernel evaluation.

The advances presented in this dissertation suggest a number of directions for future investigation, which I will categorize by subject area: work on new similarity calculation techniques, research into kernel methods, and applications of this dissertation's methods in biochemical machine learning.

## 9.1 Directions in Chemical Similarity Search

### 9.1.1 Reducing Noise in Shape Similarity

In Chapter 2 of this work, I applied the increased arithmetic throughput from GPUs to accelerate the performance (in evaluations/sec) of 3D shape comparison. However, the results of Chapter 7 suggest an interesting alternative application of these additional FLOP/s. PAPER follows the original Grant et al. [33] prescription for three-dimensional shape comparison; in particular, it uses a second-order truncation of the overlap objective function (considering only pairwise atomic overlaps) and a local optimization scheme to find the best overlay. However, Chapter 7 demonstrates that these approximations add sufficient error to the shape-overlap kernel function to impede low-rank approximation efforts. Since the SCISSORS low-rank approximation is critical to achieving maximum performance on large-scale similarity comparison it makes sense to tailor the source similarity calculation for best performance in the approximation by reducing kernel noise.

The extension of shape overlay comparison to higher-order overlaps is a particularly simple (and thus, appealing) future option. Because the second-order truncation does not remove doubly-counted regions of space from the overlap volume, it is an overestimator for the true overlap. Adding higher-order overlap terms would be easily handled with the color force field interaction matrix used to implement chemotype comparison in PLASTIC, described in Chapter 8. All order-three overlap functions, in the Gaussian formalism, can be described as the product of three atom-centered Gaussians. In the Grant and Pickup 2nd-order method, the product of two Gaussians is reduced to a single Gaussian, which has an analytic integral. Similarly, it should be possible to reduce a 3rd-order interaction to the product of an atom-centered Gaussian and a "virtual" Gaussian constructed from the

product of the remaining two atoms' densities. These virtual Gaussians are thus equivalent to color/chemotype virtual atoms of a new type: this "shape-pair" type has a negative interaction with standard shape atoms, and no interaction with other atoms. This general approach, in which high-order overlaps are reduced to pairwise overlaps between shape atoms and virtual atoms, with varying weight depending on the sign of the term, can be generalized to arbitrarily high order (though the number of virtual atoms in a structure will grow combinatorially quickly).

An alternative way to reduce the noise in shape comparison would be to modify the final step in the algorithm. As currently described, PAPER/PLASTIC choose the final "winning" pose from the optimized pool of starting poses by evaluating the (truncated second-order) objective. This leads to the very small shift in performance seen in Figure 7.1: adding starting points is almost as likely to hurt the true objective as help it, since the minima of the true and truncated objectives do not align. Adding a rescoring step, in which each optimized pose is rescored using the exact scoring function (e.g., by high-resolution quadrature on the GPU), would restore the desired optimization property that adding starting positions cannot hurt the final answer. While quadrature may be too expensive for every objective evaluation during pose optimization, a single rescoring evaluation at the end, particularly when GPU-accelerated, may still maintain high overall throughput while reducing noise.

### 9.1.2 Accelerating SCISSORS-based searches

The high dimensionality of SCISSORS vectors is a limiting factor in their search performance. In particular, it would be desirable to reduce the memory bandwidth requirements for SCISSORS-based one-vs-many searches, in which streaming the database vectors from main memory is the bottleneck. Here, the optimality properties of the kernel PCA projection underlying SCISSORS may allow significant speedups in the (common) case where only a few high-scoring hits are desired from a database, rather than a full rank-ordering. Because dimensions in the SCISSORS projection are sorted in descending order of importance to the overall similarity, it should be possible to incrementally search a SCISSORS database by considering low-dimensional subspaces in the SCISSORS space at a time. For example, given 256-D SCISSORS vectors, it may be possible to do a search on the first 16 dimensions

alone for the whole database and filter out compounds which are unlikely to appear in the final result list. Such a hierarchical strategy has the hope of significantly reducing bandwidth costs at the expense of increased complexity and increased false-positive/negative rate.

## 9.2 Topics in Kernel Methods

The analysis of low-rank approximation in the presence of noise presented in Chapter 7, while experimentally relevant to the analysis of SCISSORS for shape approximation, has several limitations. In particular, our perturbation analysis in its current form only considers zero-mean iid Gaussian noise. The extension of this analysis to other forms of kernel inexactitude may be of significant interest. In particular, errors in kernel functions will typically be neither independent nor identically distributed among kernel elements: one may imagine a dependence on each data point, such that noise terms within a row or column might be significantly correlated, with distinct distributions per-row or -column. Additionally, the assumption of normality of the noise, while analytically tractable, is strong. Using the Central Limit Theorem, it should be possible to demonstrate that our results hold for a larger class of error distributions. Work examining other distributions without invoking the CLT may also be useful: in particular, distributions arising from quantization error, numerical roundoff, and approximate function evaluation (e.g., transcendental functions) may be of interest in a number of numerical applications.

## 9.3 Applications in Biochemical Machine Learning

The high-speed similarity techniques described in this dissertation enable a wide range of potential applications in biochemical machine learning. These applications benefit from three attributes of the described methods: fast one-vs-many search using GPUs or precalculated SCISSORS databases, accelerated many-vs-many search using SCISSORS, and the translation of non-vectorial molecular data into a vector space.

### 9.3.1 Fast One-vs-Many Search

As I argued in Chapter 8, the ability to perform similarity queries on million-molecule scale databases with turnaround time in seconds enables new workflows in medicinal chemistry. Computer-aided design tools in medicinal chemistry are often used as "idea generation" techniques, in which new chemical proposals are shown to bench chemists in response to structural information or previous compounds in a series. However, the slow speed of prior search methods restricted the application of 3D-similarity-based proposals to batch mode processing. The ability to return results in seconds makes possible an interactive workflow, in which chemists could sketch out a desired compound and in real time see compounds of similar shape and functionality from a database, without waiting for a slow batch query.

### 9.3.2 Fast Many-vs-Many Search

The conclusion to Chapter 8 describes an application of GPU+SCISSORS accelerated similarity search to build a probabilistic graphical model on chemical space by connecting highly-related compounds in a Markov graphical model. Another interesting application of many-vs-many search is to directly predict protein binding partners of given molecules by shape comparison.

It would be possible to construct a space-filling model of a protein binding pocket (possibly with virtual color atoms representing desirable chemotypes at particular sites in the binding cavity), and then compare these "negative images" directly with compounds. Such a problem, given the thousands of available protein structures and millions of compounds currently known, requires fast pairwise comparison in order to be tractable. The scale of the problem is dramatically expanded by considering protein flexibility. In principle, molecular dynamics or Monte Carlo simulations could be used to sample the accessible conformational space of a protein binding pocket; each accessible conformational state would then be modeled by a different space-filling model, perhaps growing the problem by a factor of 10 to 100.

### 9.3.3 Projecting Molecules into Vector Spaces

Because molecules are not naturally interpreted as elements of a vector space, many techniques from machine learning (usually defined on vectorial data) are not easily applied to biochemistry. The use of an appropriate set of features to represent molecules as vectors is thus critical for machine learning. However, in some cases, it is simpler to define a similarity or distance function between molecules than it is to define a set of features to reproduce that similarity. For example, minimum-distance field similarities such as electrostatic and shape similarity are easily defined algorithmically, but defy a simple feature-space definition because of their invariance to rotation and translation of the molecules in question. SCISSORS provides a method to compute an optimal feature-space projection for molecules based on a similarity score, under the assumptions that the feature space is adequately sampled by a small set of landmark molecules and the eigenspectrum of the similarity function falls off rapidly. Thus, SCISSORS enables the application of vector-based machine learning methods to chemical data by computing vector features of molecules based on particular chemical similarities. An especially interesting application of this vector-space projection would be to learn SCISSORS features for a variety of similarity functions based on different chemical data (e.g., shape, chemotype, electrostatics, chemical graph, etc.) and then use feature selection or metric learning to train a new similarity measure fusing the relevant features of each component similarity method.

# Bibliography


[1] ACHLIOPTAS, D. Random matrices in data analysis. In *Proc. 15th European Conf. on Machine Learning* (2004), pp. 1–8.

[2] ACHLIOPTAS, D., MCSHERRY, F., AND SCHÖLKOPF, B. Sampling techniques for kernel methods. In *Annual Advances in Neural Information Processing Systems 14: Proceedings of the 2001 Conference* (2001), vol. 14, pp. 335–342.

[3] AHO, A. V., AND CORASICK, M. J. Efficient string matching: an aid to bibliographic search. *Commun. ACM 18*, 6 (June 1975), 333–340.

[4] ALBISTON, A. L., MORTON, C. J., NG, H. L., PHAM, V., YEATMAN, H. R., YE, S., FERNANDO, R. N., DE BUNDEL, D., ASCHER, D. B., MENDELSOHN, F. A. O., PARKER, M. W., AND CHAI, S. Y. Identification and characterization of a new cognitive enhancer based on inhibition of insulin-regulated aminopeptidase. *The FASEB Journal 22*, 12 (Dec. 2008), 4209–4217.

[5] BALLESTER, P. J., AND RICHARDS, W. G. Ultrafast shape recognition to search compound databases for similar molecular shapes. *J. Comput. Chem. 28*, 10 (July 2007), 1711–1723.

[6] BATSANOV, S. S. Van der Waals radii of elements. *Inorg Mat 37*, 9 (2001), 871–885.

[7] BENGIO, Y., DELALLEAU, O., ROUX, N. L., PAIEMENT, J.-F., VINCENT, P., AND OUIMET, M. Learning eigenfunctions links spectral embedding and kernel PCA. *Neural Comput. 16*, 10 (October 2004), 2197–2219.

[8] BLUM, L. C., AND REYMOND, J.-L. 970 million druglike small molecules for virtual screening in the chemical universe database GDB-13. *J. Am. Chem. Soc. 131*, 25 (July 2009), 8732–8733.

[9] BOHACEK, R. S., MCMARTIN, C., AND GUIDA, W. C. The art and practice of structure-based drug design: A molecular modeling perspective. *Med. Res. Rev. 16*, 1 (1996), 3–50.

[10] BOLTON, E. E., KIM, S., AND BRYANT, S. H. PubChem3D: Conformer generation. *J. Cheminformatics 3*, 1 (Mar. 2011).

[11] BOLTON, E. E., KIM, S., AND BRYANT, S. H. PubChem3D: Diversity of shape. *J. Cheminformatics 3*, 1 (Mar. 2011).

[12] BONDI, A. van der Waals volumes and radii. *J. Phys. Chem. 68*, 3 (March 1964), 441–451.

[13] BOSER, B. E., GUYON, I. M., AND VAPNIK, V. N. A training algorithm for optimal margin classifiers. In *Proceedings of the 5th Annual Workshop on Computational Learning Theory* (New York, NY, USA, 1992), COLT '92, ACM, pp. 144–152.

[14] BRAUN, M. L., BUHMANN, J., AND MUELLER, K.-R. Denoising and dimension reduction in feature space. In *Annual Advances in Neural Information Processing Systems 19: Proceedings of the 2006 Conference* (2007), vol. 19.

[15] BUTINA, D. Unsupervised data base clustering based on Daylight's fingerprint and Tanimoto similarity: A fast and automated way to cluster small and large data sets. *J. Chem. Inf. Comput. Sci. 39*, 4 (July 1999), 747–750.

[16] CARHART, R. E., SMITH, D. H., AND VENKATARAGHAVAN, R. Atom pairs as molecular features in structure-activity studies: definition and applications. *J. Chem. Inf. Comput. Sci. 25*, 2 (May 1985), 64–73.

[17] CHARIFSON, P. S., Ed. *Practical Application of Computer-Aided Drug Design*, 1 ed. Marcel Dekker, New York, July 1997.

[18] CHEESERIGHT, T., MACKEY, M., ROSE, S., AND VINTER, A. Molecular field extrema as descriptors of biological activity: Definition and validation. *J. Chem. Inf. Model. 46*, 2 (Mar. 2006), 665–676.

[19] CHODERA, J. D., MOBLEY, D. L., SHIRTS, M. R., DIXON, R. W., BRANSON, K., AND PANDE, V. S. Alchemical free energy methods for drug discovery: progress and challenges. *Curr. Opin. Struct. Biol. 21*, 2 (Apr. 2011), 150–160.

[20] CLARK, R. D., AND WEBSTER-CLARK, D. J. Managing bias in ROC curves. *J. Comput. Aided Mol. Des.* (February 2008).

[21] CONNOLLY, M. L. Computation of molecular volume. *J. Am. Chem. Soc. 107*, 5 (1985), 1118–1124.

[22] COX, T. F., AND COX, M. A. A. *Multidimensional Scaling*. Chapman & Hall, London, January 1994.

[23] DENG, Y., AND ROUX, B. Computation of binding free energy with molecular dynamics and grand canonical Monte Carlo simulations. *The Journal of Chemical Physics 128*, 11 (2008), 115103+.

[24] DRINEAS, P., AND MAHONEY, M. W. On the Nyström method for approximating a Gram matrix for improved kernel-based learning. *J. Mach. Learn. Res. 6* (2005).

[25] DURANT, J. L., LELAND, B. A., HENRY, D. R., AND NOURSE, J. G. Reoptimization of MDL keys for use in drug discovery. *J. Chem. Inf. Comput. Sci. 42*, 6 (November 2002), 1273–1280.

[26] FERRARA, P., GOHLKE, H., PRICE, D. J., KLEBE, G., AND BROOKS, C. L. Assessing Scoring Functions for Protein-Ligand Interactions. *Journal of Medicinal Chemistry 47*, 12 (June 2004), 3032–3047.

[27] FONTAINE, F., BOLTON, E., BORODINA, Y., AND BRYANT, S. H. Fast 3D shape screening of large chemical databases through alignment-recycling. *Chem. Cent. J. 1* (2007), 12.

[28] FRIEDRICHS, M. S., EASTMAN, P., VAIDYANATHAN, V., HOUSTON, M., LEGRAND, S., BEBERG, A. L., ENSIGN, D. L., BRUNS, C. M., AND PANDE, V. S. Accelerating molecular dynamic simulation on graphics processing units. *J. Comput. Chem. 30*, 6 (2009), 864–872.

[29] GAMO, F.-J., SANZ, L. M., VIDAL, J., DE COZAR, C., ALVAREZ, E., LAVANDERA, J.-L., VANDERWALL, D. E., GREEN, D. V. S., KUMAR, V., HASAN, S., BROWN, J. R., PEISHOFF, C. E., CARDON, L. R., AND GARCIA-BUSTOS, J. F. Thousands of chemical starting points for antimalarial lead identification. *Nature 465*, 7296 (May 2010), 305–310.

[30] GASIOROWICZ, S. *Quantum Physics*. John Wiley and Sons, New York, 1974.

[31] GOLUB, G. H., AND VAN LOAN, C. F. *Matrix Computations*, 3rd ed. The Johns Hopkins University Press, Baltimore, October 1996.

[32] GOTO, K., AND VAN DE GEIJN, R. High-performance implementation of the level-3 BLAS. *ACM Trans. Math. Softw. 35*, 1 (2008), 1–14.

[33] GRANT, J. A., GALLARDO, M. A., AND PICKUP, B. T. A fast method of molecular shape comparison: A simple application of a Gaussian description of molecular shape. *J. Comp. Chem. 17*, 14 (1996), 1653–1666.

[34] GRANT, J. A., HAIGH, J. A., PICKUP, B. T., NICHOLLS, A., AND SAYLE, R. A. Lingos, finite state machines, and fast similarity searching. *J. Chem. Inf. Model. 46*, 5 (September 2006), 1912–1918.

[35] GRANT, J. A., AND PICKUP, B. T. A Gaussian description of molecular shape. *J. Phys. Chem. 99*, 11 (1995).

[36] GRIEWANK, A. O., MARKEY, B. R., AND EVANS, D. J. Singularity-free static lattice energy minimization. *J. Chem. Phys. 71*, 8 (1979), 3449–3454.

[37] GUNDERSEN, E., FAN, K., HAAS, K., HURYN, D., JACOBSEN, J. S., KREFT, A., MARTONE, R., MAYER, S., SONNENBERG-REINES, J., AND SUN, S. Molecular-modeling based design, synthesis, and activity of substituted piperidines as gamma-secretase inhibitors. *Bioorg & Med Chem Lett 15*, 7 (April 2005), 1891–1894.

[38] HAIGH, J. A., PICKUP, B. T., GRANT, J. A., AND NICHOLLS, A. Small molecule shape-fingerprints. *J. Chem. Inf. Model 45*, 3 (May 2005), 673–684.

[39] HAQUE, I. S., AND PANDE, V. S. PAPER — accelerating parallel evaluations of ROCS. *J. Comput. Chem. 31*, 1 (2009), 117–132.

[40] HAQUE, I. S., AND PANDE, V. S. SCISSORS: A linear-algebraical technique to rapidly approximate chemical similarities. *J. Chem. Inf. Model. 50*, 6 (June 2010), 1075–1088.

[41] HAQUE, I. S., AND PANDE, V. S. Large-Scale chemical informatics on GPUs. In *GPU Computing Gems: Emerald Edition* (Feb. 2011), W.-m. W. Hwu, Ed., Morgan Kaufmann.

[42] HAQUE, I. S., PANDE, V. S., AND WALTERS, W. P. SIML: A fast SIMD algorithm for calculating LINGO chemical similarities on GPUs and CPUs. *J. Chem. Inf. Model. 50*, 4 (Apr. 2010), 560–564.

[43] HUANG, N., KALYANARAMAN, C., IRWIN, J. J., AND JACOBSON, M. P. Physics-Based Scoring of Protein-Ligand Complexes: Enrichment of Known Inhibitors in Large-Scale Virtual Screening. *J. Chem. Inf. Model. 46*, 1 (Jan. 2006), 243–253.

[44] HUANG, N., SHOICHET, B. K., AND IRWIN, J. J. Benchmarking sets for molecular docking. *J. Med. Chem. 49*, 23 (October 2006), 6789–6801.

[45] IRWIN, J. J., AND SHOICHET, B. K. ZINC — a free database of commercially available compounds for virtual screening. *J. Chem. Inf. Model. 45*, 1 (2005), 177–182.

[46] JAIN, A. N. Ligand-based structural hypotheses for virtual screening. *J. Med. Chem. 47*, 4 (February 2004), 947–961.

[47] JARVIS, R. A., AND PATRICK, E. A. Clustering using a similarity measure based on shared near neighbors. *IEEE Transactions on Computers C-22*, 11 (Nov. 1973), 1025–1034.

[48] JENKINS, J. L., GLICK, M., AND DAVIES, J. W. A 3D similarity method for scaffold hopping from known drugs or natural ligands to new chemotypes. *J. Med. Chem. 47*, 25 (Dec. 2004), 6144–6159.

[49] JENKINS, O. C. Localization from pairwise distance relationships using kernel PCA. Tech. Rep. CRES-03-010, Los Angeles, USA, 2003.

[50] JORGENSEN, W. L. Efficient Drug Lead Discovery and Optimization. *Accounts Chem. Res. 42*, 6 (June 2009), 724–733.

[51] KEARSLEY, S. K. An algorithm for the simultaneous superposition of a structural series. *J. Comp. Chem. 11*, 10 (1990), 1187–1192.

[52] KLEPEIS, J. L., LINDORFF-LARSEN, K., DROR, R. O., AND SHAW, D. E. Long-timescale molecular dynamics simulations of protein structure and function. *Curr. Opin. Struct. Biol. 19*, 2 (Apr. 2009), 120–127.

[53] LAUB, J., ROTH, V., BUHMANN, J. M., AND MÜLLER, K. R. On the information and representation of non-Euclidean pairwise data. *Pattern Recogn. 39* (Oct. 2006), 1815–1826.

[54] LI, H., YAP, C. W., UNG, C. Y., XUE, Y., CAO, Z. W., AND CHEN, Y. Z. Effect of selection of molecular descriptors on the prediction of blood-brain barrier penetrating and nonpenetrating agents by statistical learning methods. *J. Chem. Inf. Model. 45*, 5 (September 2005), 1376–1384.

[55] LINDHOLM, E., NICKOLLS, J., OBERMAN, S., AND MONTRYM, J. NVIDIA Tesla: A unified graphics and computing architecture. *IEEE Micro 28*, 2 (2008), 39–55.

[56] LODHI, H., SAUNDERS, C., SHAWE-TAYLOR, J., CRISTIANINI, N., AND WATKINS, C. Text classification using string kernels. *J. Mach. Learn. Res. 2* (Feb. 2002), 419–444.

[57] MARTIN, E. J., BLANEY, J. M., SIANI, M. A., SPELLMEYER, D. C., WONG, A. K., AND MOOS, W. H. Measuring diversity: Experimental design of combinatorial libraries for drug discovery. *J. Med. Chem. 38*, 9 (April 1995), 1431–1436.

[58] MILLER, M. D., SHERIDAN, R. P., AND KEARSLEY, S. K. SQ: A program for rapidly producing pharmacophorically relevent molecular superpositions. *J. Med. Chem. 42*, 9 (May 1999), 1505–1514.

[59] MUCHMORE, S. W., SOUERS, A. J., AND AKRITOPOULOU-ZANZE, I. The use of three-dimensional shape and electrostatic similarity searching in the identification of a melanin-concentrating hormone receptor 1 antagonist. *Chem. Biol. Drug Des. 67*, 2 (February 2006), 174–176.

[60] NICHOLLS, A. Method for determining a shape space for a set of molecules using minimal metric distances. *U.S. Patent 7,110,888* (September 2006).

[61] NICHOLLS, A., AND GRANT, J. A. Molecular shape and electrostatics in the encoding of relevant chemical information. *J. Comput.-Aided Mol. Des. 19*, 9 (September 2005), 661–686.

[62] NICHOLLS, A., MACCUISH, N., AND MACCUISH, J. Variable selection and model validation of 2D and 3D molecular descriptors. *J. Comput.-Aided Mol. Des. 18*, 7 (July 2004), 451.

[63] NICKOLLS, J., BUCK, I., GARLAND, M., AND SKADRON, K. Scalable parallel programming with CUDA. *ACM Queue 6*, 2 (2008), 40–53.

[64] NIKOLOVA, N., AND JAWORSKA, J. Approaches to measure chemical similarity - a review. *QSAR & Combin. Sci. 22*, 9-10 (January 2003), 1006–1026.

[65] NVIDIA. *NVIDIA CUDA Programming Guide 2.0*. NVIDIA, 2008.

[66] ODONE, F., BARLA, A., AND VERRI, A. Building kernels from binary strings for image matching. *IEEE Trans. Image Proc. 14*, 2 (Feb. 2005), 169–180.

[67] OMEGA IN OPENEYE PYTHON TOOLKITS, VERSION 1.5.1-1. *OpenEye Scientific Software, Inc., Santa Fe, NM, USA, www.eyesopen.com.* (2007).

[68] PEKALSKA, E. M. *Dissimilarity representations in pattern recognition. Concepts, theory and applications.* PhD thesis, Wroclaw University, Wroclaw, Poland, January 2005.

[69] PONDER, J. W., WU, C., REN, P., PANDE, V. S., CHODERA, J. D., SCHNIEDERS, M. J., HAQUE, I., MOBLEY, D. L., LAMBRECHT, D. S., DISTASIO, R. A., HEAD-GORDON, M., CLARK, G. N. I., JOHNSON, M. E., AND HEAD-GORDON, T. Current Status of the AMOEBA Polarizable Force Field. *J. Phys. Chem. B 114*, 8 (Mar. 2010), 2549–2564.

[70] PRESS, W. H., FLANNERY, B. P., TEUKOLSKY, S. A., AND VETTERLING, W. T. *Numerical Recipes in C : The Art of Scientific Computing*. Cambridge University Press, October 1992.

[71] RAGHAVENDRA, A. S., AND MAGGIORA, G. M. Molecular basis sets — a general similarity-based approach for representing chemical spaces. *J. Chem. Inf. Model. 47*, 4 (July 2007), 1328–1340.

[72] REFSGAARD, H. H., JENSEN, B. F., BROCKHOFF, P. B., PADKJAER, S. B., GULDBRANDT, M., AND CHRISTENSEN, M. S. In silico prediction of membrane permeability from calculated molecular parameters. *J. Med. Chem. 48* (Feb 2005), 805–811.

[73] ROCS. *OpenEye Scientific Software, Inc., Santa Fe, NM, USA, www.eyesopen.com* (2008).

[74] ROGERS, D., AND HAHN, M. Extended-connectivity fingerprints. *J. Chem. Inf. Model. 50* (May 2010), 742–754.

[75] RUSH, T. S., GRANT, J. A., MOSYAK, L., AND NICHOLLS, A. A shape-based 3-d scaffold hopping method and its application to a bacterial protein-protein interaction. *J. Med. Chem. 48*, 5 (March 2005), 1489–1495.

[76] SCHNEIDER, G., NEIDHART, W., GILLER, T., AND SCHMID, G. "Scaffold-Hopping" by topological pharmacophore search: a contribution to virtual screening. *Angewandte Chemie (Intl. ed. in English) 38*, 19 (Oct. 1999), 2894–2896.

[77] SCHÖLKOPF, B., SMOLA, A., AND MÜLLER, K.-R. Nonlinear component analysis as a kernel eigenvalue problem. Tech. Rep. 44, Tuebingen, Germany, December 1996.

[78] SCHÖLKOPF, B., SMOLA, A., AND MÜLLER, K.-R. Nonlinear component analysis as a kernel eigenvalue problem. *Neural Comput. 10*, 5 (July 1998), 1299–1319.

[79] SHAWE-TAYLOR, J., WILLIAMS, C. K. I., CRISTIANINI, N., AND KANDOLA, J. On the eigenspectrum of the Gram matrix and the generalization error of kernel-PCA. *IEEE Trans. Info. Theory 51*, 7 (July 2005), 2510–2522.

[80] SHIRTS, M., MOBLEY, D., AND CHODERA, J. Alchemical Free Energy Calculations: Ready for Prime Time? *Annual Reports Comput. Chem. 3* (2007), 41–59.

[81] STONE, J. E., PHILLIPS, J. C., FREDDOLINO, P. L., HARDY, D. J., TRABUCO, L. G., AND SCHULTEN, K. Accelerating molecular modeling applications with graphics processors. *J. Comput. Chem. 28*, 16 (September 2007), 2618–2640.

[82] SUN, D., CHUAQUI, C., DENG, Z., BOWES, S., CHIN, D., SINGH, J., CULLEN, P., HANKINS, G., LEE, W.-C., DONNELLY, J., FRIEDMAN, J., AND JOSIAH, S. A kinase-focused compound collection: Compilation and screening strategy. *Chem Biol & Drug Des 67*, 6 (June 2006), 385–394.

[83] TALWALKAR, A. *Matrix Approximation for Large-scale Learning*. PhD thesis, Courant Institute of Mathematical Sciences, New York University, New York, NY, May 2010.

[84] TANAKA, N., OHNO, K., NIIMI, T., MORITOMO, A., MORI, K., AND ORITA, M. Small-world phenomena in chemical library networks: Application to fragment-based drug discovery. *J. Chem. Inf. Model. 12*, 49 (2009), 2677–2686.

[85] VIDAL, D., THORMANN, M., AND PONS, M. LINGO, an efficient holographic text based method to calculate biophysical properties and intermolecular similarities. *J. Chem. Inf. Model. 45*, 2 (March 2005), 386–393.

[86] WASSON, S. Nvidia's GeForce GTX 280 graphics processor. *The Tech Report.* (Accessed 1 Jul 2008).

[87] WILLIAMS, C., AND SEEGER, M. Using the Nyström method to speed up kernel machines. In *Advances in Neural Information Processing Systems 13* (2001), vol. 13, pp. 682–688.

[88] WILLIAMS, C. K. I. On a connection between kernel pca and metric multidimensional scaling. *Mach. Learn. 46*, 1-3 (January 2002), 11–19.

[89] ZAUHAR, R. J., MOYNA, G., TIAN, L., LI, Z., AND WELSH, W. J. Shape signatures: a new approach to computer-aided ligand- and receptor-based drug design. *J. Med. Chem. 46*, 26 (December 2003), 5674–5690.